UNIVERSIDAD DE CANTABRIA
Departamento de Física Moderna

y

CSIC – UC
Instituto de Física de Cantabria

Estudio Mesoscópico de la Plasticidad y Fractura en Materiales Desordenados

Memoria presentada por la Licenciada
Clara Beatriz Picallo González
para optar al título de
Doctora por la Universidad de Cantabria

Realizada bajo la supervisión del
Dr. **Juan Manuel López Martín**

2010

Dr. Juan Manuel López Martín, Investigador Científico del Consejo Superior de Investigaciones Científicas, certifica:

> Que la presente Memoria, titulada **"Estudio Mesoscópico de la Plasticidad y Fractura en Materiales Desordenados"**, ha sido realizada, bajo mi dirección, por Clara Beatriz Picallo González, y constituye su Tesis para optar al grado de Doctora por la Universidad de Cantabria. Asimismo emito mi conformidad para que dicha memoria sea presentada y tenga lugar, posteriormente, la correspondiente lectura.

Santander, a 13 de Octubre de 2010

Fdo.: Dr. Juan Manuel López Martín

A mis padres.

Agradecimientos

En primer lugar quiero expresar mi profunda gratitud a Juanma por haberme dado la oportunidad de realizar este trabajo. Además de su valiosa dirección científica, siempre me ha brindado su ayuda y constantes ánimos.

I would like to acknowledge Mikko Alava and Stefano Zapperi for giving me the privilege to work with and learn from them. I am truly in debt to all the people at the ISI Foundation for their help and hospitality. I also thank Hermann Riecke for introducing me to a very different field of research and the support received at the Northwestern University.

Al grupo de Física Estadística y No Lineal del Instituto de Física de Cantabria, especialmente a Ana, Diego, Iván, Jorge, Marta y Silvia, compañeros y amigos del despacho S114, por todos los buenos momentos disfrutados en su compañía.

A mis padres, por su cariño e interés infinitos. A mi hermana María, víctima habitual de mis altibajos, por su paciencia y apoyo fundamentales durante este tiempo. Al resto de mi familia por estar siempre pendientes, animándome con entusiasmo en todos mis proyectos. A los amigos que, desde aquí o en la distancia, han seguido y alentado el desarrollo de esta tesis, consiguiendo que me olvidase de ella siempre que era necesario.

Agradezco también la financiación recibida a través de la beca AP2005-0944 del Programa de Formación de Profesorado Universitario (FPU) del Ministerio de Educación.

Santander, a 13 de Octubre de 2010

A Mesoscopic Study of Plasticity and Fracture in Disordered Materials

A dissertation submitted in partial fulfillment of the
requirements for the degree of
Doctor of Philosophy in Physics

by

Clara Beatriz Picallo González

UNIVERSIDAD DE CANTABRIA
Departamento de Física Moderna

&

CSIC – UC
Instituto de Física de Cantabria

2010

Contents

Chapter 1

Motivations and Outline

Understanding how materials deform and break is a subject of critical importance in industry. At the same time, it requires from the knowledge of the basic processes governing the phenomenon and hence, fundamental physics research is a must. From the very beginning, there was the need of having quantitative rules for the resistance of materials. The first attempts to quantify these phenomena date back to the early experimental works of Leonardo Da Vinci in the fifteenth century with wires of different lengths (collected in [da Vinci 1940]) and the subsequent works of Galileo Galilei who summarized the *new science of mechanics* in his work [Galilei 1638], along with the studies of elastic bodies by Robert Hooke [Hooke 1678]. Modern fracture mechanics is considered to begin with the efforts of Griffith to establish an energetic criterion for the propagation of brittle failure [Griffith 1921] and the extension of Irwin for ductile materials [Irwin 1948]. Nowadays, in spite of the technological development of the field, many questions remain open after years of intensive research. Moreover, several experiments in the last decades have revealed features that cannot be accounted for within the framework of continuum mechanics [Alava et al. 2006, Zaiser 2006].

Many subjects get straightforward benefits from the advances in fracture and deformation mechanics. For instance, nanomaterials are of crucial importance for new developing technologies and hence the knowledge of how size affects their behavior is essential for the good performance at those scales. It has been observed in many materials and experimental setups that small size samples exhibit surprisingly higher strengths than macroscopic samples of the same material.

The design of new materials *à la carte* relies on the knowledge of how temperature, chemical composition, microstructure, etc., affect the mechanical response of the material. A trendy example is the production of metallic glasses. These alloys usually display high yield stress and macroscopic brittleness at room temperature. However, with the adequate composition, production technique and treatments, ductile metallic glasses that exhibit perfect plasticity or strain hardening over a wide range of strain can be obtained and are employed in many interesting applications like micro-electro-mechanical systems [Greer 2009, Schuh et al. 2007].

Also interestingly, the mechanical properties of biological materials are now starting to be investigated and the understanding of their complex hierarchical nature is still a challenge. It seems that this hierarchical structure plays a decisive role in the tolerance of these kind of materials to microcracks and a good knowledge of the mechanisms that rule them may open the door to the construction of biomaterials and bio-inspired materials [Buehler and Keten 2010]. Many applications can be envisaged as the detection of diseases by changes in the material properties, prediction of the fracture of bones, or tissue regeneration, just to name a few.

The presence of power law distributions in both temporal and spatial properties and the universality of the behavior seem to suggest that fracture and plasticity could be explained as some type of critical phenomena [Alava et al. 2006, Zaiser 2006]. This means that there should be some general principles that rule the process and that are more important than a detailed description of the interactions and atomic structure of the media. Hence, simplified theoretical approaches based on fundamental concepts can help to capture the essential ingredients in the system. In this sense, tools coming from statistical mechanics can help to deal with disorder, long range interactions and scaling laws. In the last decade several steps have been given in this direction and, to this aim, some simplified models have been developed and studied. This Thesis is devoted to the study of the deformation and failure of materials in the presence of disorder with the help of statistical mechanics tools and models. The outline of this Thesis is as follows:

Chapter 2 (page 5) serves as a brief review of solid mechanics and the different approaches to modeling the response of materials. We focus on the statistical physics approach to the problem, describing the models and the insight gained from this perspective. We give special attention to the Random Fuse Model (RFM) [de Arcangelis et al. 1985], a simple scalar model based on the formal analogy of electrical and mechanical equations that has become

the cornerstone of lattice models for fracture and will be used throughout this Thesis.

In Chapter 3 (page 23) we numerically study the brittle fracture of materials by means of the acoustic emission produced during the load of an amorphous medium simulated with the RFM. Acoustic emission is a typical experimental tool for monitoring damage in materials. After introducing the subject of *crackling noise* in section 3.1, in section 3.2 we study the differences between several energy estimators and derive scaling relations that account for their statistical behavior. We also study the temporal evolution of the energy dissipation in the search for traces of the proximity of final failure. Finally, the consequences of relaxing the quasistatic loading condition to mimic dynamic fracture are also studied. These results were published in [Picallo and López 2008].

Chapter 4 (page 45) deals with elastic-perfectly plastic behavior. A brief introduction to the basic concepts is found in 4.1 where the elastic-perfectly plastic version of the RFM is presented as well as the conjectured equivalence of this problem to the classic topic of directed polymers and minimum energy surfaces. In section 4.2 we numerically and theoretically revise the relation between minimum energy surfaces and the yield surfaces produced with an elastic perfectly plastic RFM. These results were published in [Picallo et al. 2009].

Chapter 5 (page 65) begins with a description of the experimental findings and existing numerical models of plasticity in section 5.1. In section 5.2 we introduce a lattice model for ductile fracture based on the RFM but able to account for both brittle and ductile behavior. In section 5.3 we study the transition from brittleness to ductility as plastic deformation is accumulated prior to fracture. Ductile fracture surfaces are compared to minimum energy surfaces and crack surfaces resulting from brittle fracture. The burst avalanches are also studied and compared with the current theoretical and experimental understanding. These results correspond to [Picallo et al. 2010a;b].

Chapter 2

Introduction

Deformation and fracture events are commonly observed around us and our experience has taught us how differently materials like crystal and plasticine behave. Everyone has an intuitive notion of the *strength* of some materials and how *deformable* or on the contrary *fragile* materials are and how different are the fracture patterns that arise when breaking one or the other.

The present chapter will formalize these intuitive concepts and establish the basic working framework in solid mechanics (see, for instance [Lai et al. 1999, Lubliner 2008, Rice 1999]). We will also discuss the key ingredients that one must take into account to build a fracture model and some of the possible approaches to the problem. We will focus on the statistical physics point of view giving a brief description of the kind of models proposed by this community and some of the insights gained during the past few years. We will finish describing the model that will be used throughout this Thesis.

2.1 Solid mechanics in brief

If we follow what happens to one of the material points of a continuous body subject to deformation, it will move from its reference configuration $\mathbf{r_0}$ to a different spatial position $\mathbf{r}(\mathbf{r_0}, t)$. The difference between these two positions defines the *displacement vector* $\mathbf{u} = \mathbf{r}(\mathbf{r_0}, t) - \mathbf{r_0}$.

When deformations are small ($\mathbf{u} \to 0, \nabla\mathbf{u} \to 0$), it is enough to characterize the changes in shape with the so called *infinitesimal strain tensor* $\boldsymbol{\epsilon}$, a second-

order tensor corresponding to the symmetric part of $\nabla \mathbf{u}$:

$$\epsilon_{ij} = \frac{1}{2}\left(\frac{\partial u_i}{\partial x_j} + \frac{\partial u_j}{\partial x_i}\right), \tag{2.1}$$

where $i, j = 1, 2, 3$ are the 3D spatial components [Lai et al. 1999]. Note that the strain $\boldsymbol{\epsilon}$ is a dimensionless variable while the displacement $\mathbf{u}$ has units of [Length].

The range of deformations in which this approximation is valid can be studied within the *infinitesimal strain theory*, in contrast with the *finite strain theory* that will not be addressed here.

To obtain the equations of motion of a continuum we must apply Newton's Second Law $\sum \mathbf{F} = m\mathbf{a}$ to the solid. To this aim, we need to take into account all the forces that play a role in the material. We can distinguish between short-range and long-range forces. Long ranged forces are considered to be *body forces* that act throughout the volume of a body (e.g. gravity or magnetism) whereas short-range forces are *surface forces* that act only on a real or imaginary surface in the material and are due to the internal forces among its particles. Therefore, Newton's Second Law in the continuum can be written as:

$$\int_V \mathbf{b} dV + \int_S \mathbf{t}(\mathbf{n}) dS = \int_V \rho \mathbf{a} dV, \tag{2.2}$$

where $\mathbf{b}$ represents the body forces and $\mathbf{t}(\mathbf{n})$ the surface forces that depend not only on the position but also on the local orientation of the surface element on which they are acting.

The nature of the $\mathbf{t}(\mathbf{n})$ dependence was stated by Cauchy in the Cauchy's Stress Principle and can be deduced with the help of the Cauchy tetrahedron shown in figure 2.1. Applying Newton's Second Law to this infinitesimal tetrahedron we obtain

$$\mathbf{t^{(-1)}}\Delta S_1 + \mathbf{t^{(-2)}}\Delta S_2 + \mathbf{t^{(-3)}}\Delta S_3 + \mathbf{t}(\mathbf{n})(\Delta S_n) = \rho(\Delta V)\mathbf{a}. \tag{2.3}$$

Shrinking the volume of the tetrahedron to zero and applying the action-reaction principle $\mathbf{t^{(-i)}} = -\mathbf{t^{(i)}}$, equation 2.3 results in

$$\mathbf{t}(\mathbf{n})\Delta S_n = \mathbf{t^{(1)}}\Delta S_1 + \mathbf{t^{(2)}}\Delta S_2 + \mathbf{t^{(3)}}\Delta S_3. \tag{2.4}$$

Expressing the outward normal to the inclined face in terms of the unit vectors we have $\mathbf{n} = n_1\mathbf{e_1} + n_2\mathbf{e_2} + n_3\mathbf{e_3}$. Besides, since ΔS_i, $i = 1, 2, 3$ are the projections of ΔS_n on the Cartesian coordinate planes, they are related by $\Delta S_i = n_i \Delta S_n$. Putting all this together, equation 2.4 becomes

$$\mathbf{t}(\mathbf{n}) = n_1\mathbf{t^{(1)}} + n_2\mathbf{t^{(2)}} + n_3\mathbf{t^{(3)}}. \tag{2.5}$$

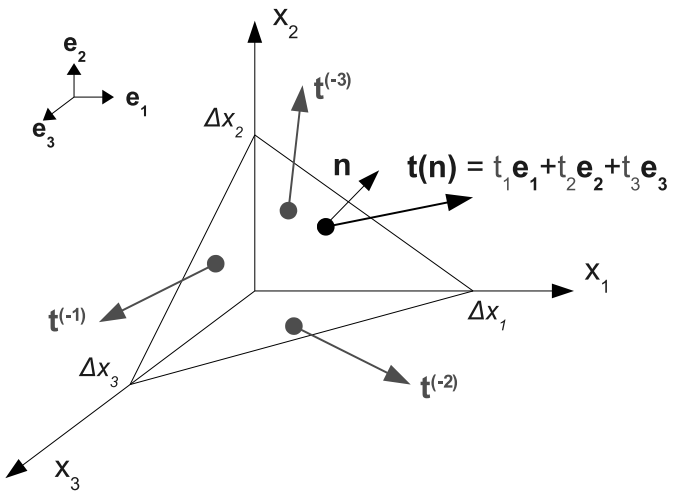

Figure 2.1: Cauchy tetrahedron showing the surface forces $\mathbf{t}^{(-\mathbf{i})}$ acting on each of its faces with outward normal $-\mathbf{e_i}$. The outward normal to the inclined face is given by $\mathbf{n}$.

Therefore, $\mathbf{t}(\mathbf{n})$ is a linear transformation of its argument $\mathbf{n}$. This leads us to the definition of the second-order *stress tensor* $\boldsymbol{\sigma}$ such that $\mathbf{t}(\mathbf{n}) = \boldsymbol{\sigma}\mathbf{n}$ and whose components can be derived from equation 2.5 to be $\sigma_{ij} = \mathbf{e_i} \cdot \mathbf{t}^{(\mathbf{j})}$. So, the component i of the stress vector $\mathbf{t}(\mathbf{n})$ is given by

$$t_i(\mathbf{n}) = \sum_j \sigma_{ij} n_j. \tag{2.6}$$

Note that the column i of $\boldsymbol{\sigma}$ represents the stress vector on the plane whose outward normal is $\mathbf{e_i}$. A representation of all the components of the stress tensor and its meaning is depicted in figure 2.2.

The component σ_{ij} of the stress tensor represents *normal stress* if $i = j$ and *shear stress* if $i \neq j$. The stress tensor is easily shown to be symmetric [Rice 1999]. The stress, as it was defined, has dimensions of ([Force]/[Length]^2), *i.e.*, it is measured in units of pressure.

Introducing equation 2.6 into equation 2.2 we obtain:

$$\int_S \sum_j \sigma_{ij} n_j dS + \int_V b_i dV = \int_V \rho a_i dV, \tag{2.7}$$

for each component $i = 1, 2, 3$.

Making use of the Divergence Theorem ($\int_S \boldsymbol{\sigma}\mathbf{n}dS = \int_V \nabla\boldsymbol{\sigma}dV$) we arrive to the (Cauchy's) equations of motion in local form for a solid body:

$$\sum_j \frac{\partial \sigma_{ij}}{\partial x_j} + \mathbf{b}_i = \rho \mathbf{a}_i. \tag{2.8}$$

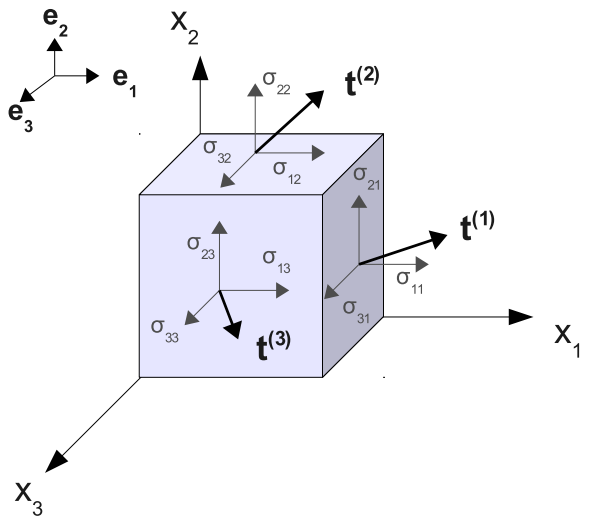

Figure 2.2: Stress components acting over an infinitesimal volume element.

2.1.1 Linear isotropic elastic solids

An extended representation of the material response to loading, independent of the specimen size and loading conditions, is the stress-strain curve. An example is shown in figure 2.3. In the limit of small deformations, it has been widely observed in experiments that there exists a linear relation between the applied load or stress and the deformation or strain in the material. In this regime, all deformations vanish as soon as the load is removed. This is known as *elastic* regime. Fracture occurring in this region is called *brittle fracture* and some of its characteristics will be studied in Chapter 3. However, some materials can exhibit a different behavior after the elastic regime and enter what is called a *plastic regime*. The fingerprint of plastic response is that deformations are permanent, as it can be observed in the unloading curves in figure 2.3. Depending on the material and experimental conditions, it is

usually characterized by either a strain increase with no more stress increments (perfect plasticity) or either a stress dependence on the strain (hardening) with a new slope determined by the hardening coefficient θ. Plastic response and the resultant ductile fracture surfaces will be addressed in Chapters 4 and 5.

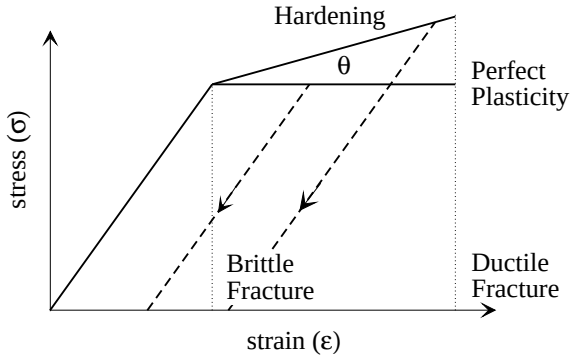

Figure 2.3: Stress-strain curve. Brittle behavior, perfectly plastic behavior, and hardening with its corresponding hardening coefficient θ are shown. Dashed lines indicate the unloading curves that will lead to strain accumulation with no stress imposed.

The first linear elastic regime of materials is called Hooke's Law. As the deformations are small, the infinitesimal strain theory is still valid. In order to have a linear dependence between the infinitesimal strain tensor and the Cauchy stress tensor, they must necessarily be related through a fourth-order tensor.

$$\sigma_{ij} = \sum_k \sum_l C_{ijkl} \epsilon_{kl}. \tag{2.9}$$

The tensor $\mathbf{C}$ is the Elasticity Tensor. The symmetry of the strain tensor imposes

$$C_{ijkl} = C_{ijlk}, \tag{2.10}$$

then reducing the number of independent coefficients to 54. The symmetry of the stress tensor requires

$$C_{ijkl} = C_{jikl}, \tag{2.11}$$

thus reducing the tensor to 36 independent components.

If the medium is isotropic, *i.e.*, its properties do not depend on the direction, the elasticity tensor must be isotropic too, *i.e.*, its components must be the same in all rotated coordinate systems. Any fourth order isotropic

tensor can be written as a linear superposition of the independent tensors $A_{ijkl} = \delta_{ij}\delta_{kl}$, $B_{ijkl} = \delta_{ik}\delta_{jl}$, $H_{ijkl} = \delta_{il}\delta_{jk}$:

$$C_{ijkl} = \lambda A_{ijkl} + \mu B_{ijkl} + \nu H_{ijkl}. \tag{2.12}$$

To preserve the symmetries of equations 2.10 and 2.11, we must have $\nu = \mu$. Therefore,

$$C_{ijkl} = \lambda\delta_{ij}\delta_{kl} + \mu(\delta_{ik}\delta_{jl} + \delta_{il}\delta_{jk}). \tag{2.13}$$

Plugging this into equation 2.9 leads us to the stress-strain relation for a linear isotropic elastic solid:

$$\sigma_{ij} = \lambda\delta_{ij}\sum_k \epsilon_{kk} + 2\mu\epsilon_{ij}, \tag{2.14}$$

where λ and μ are known as the Lamé Constants. Hence, the elastic properties of homogeneous and isotropic materials are fully described by these two constants or elastic moduli. Besides Lamé Constants, other elastic moduli are usually defined and employed, like the Young's modulus E that describes tensile elasticity, the shear modulus G defined as shear stress over shear strain, or the Poisson Ratio ν, the ratio of the transverse strain, perpendicular to the applied load, to the axial strain, in the direction of the applied load.

Now, going back to the Cauchy's equations of motion 2.8, we can obtain the Navier-Cauchy equations of motion for a linear isotropic elastic solid by directly substituting equation 2.14 along with 2.1 in equation 2.8:

$$(\lambda + \mu)\frac{\partial}{\partial x_i}\sum_j \frac{\partial u_j}{\partial x_j} + \mu\sum_j \frac{\partial^2 u_i}{\partial x_j^2} + b_i = \rho\frac{\partial^2 u_i}{\partial t^2}. \tag{2.15}$$

Or in vectorial form:

$$(\lambda + \mu)\nabla(\nabla\cdot\mathbf{u}) + \mu\nabla^2\mathbf{u} + \mathbf{b} = \rho\frac{\partial^2\mathbf{u}}{\partial t^2}. \tag{2.16}$$

Therefore, the equilibrium equation $\sum \mathbf{F} = 0$ for a linear isotropic elastic solid is:

$$(\lambda + \mu)\nabla(\nabla\cdot\mathbf{u}) + \mu\nabla^2\mathbf{u} + \mathbf{b} = 0. \tag{2.17}$$

2.2 Modeling materials: the statistical mechanics approach

Fracture mechanics is a topic that lies on the boundary among different fields. Materials scientists, mechanical engineers, and more recently, statistical physi-

cists have approached the problem from different standpoints, emphasizing and drawing attention to different questions and using different techniques.

An usual approach followed in engineering is the discretization of the continuum equations 2.16 with finite element methods. Disorder has been also included in a suitable way in these schemes [O. C. Zienkiewicz 2006].

A completely different approach to this continuum description consists in describing the material at an atomistic level. This is the aim of molecular dynamics simulations [Buehler 2008]. In this context, the Newton's Laws give the behavior of a set of atoms in an ordered or disordered structure in which the interatomic potentials are usually simplified, like for instance by using the Lennard-Jones potential. Elasticity, plasticity and fracture then arise naturally from the response at an atomic level. The main drawback is the huge computational cost that limits the number of atoms used in the simulations and the available time scales. However, this technique is useful to model nanosamples [Bitzek et al. 2008, Munilla et al. 2009] that are now under intense experimental study.

In heterogeneous materials, the final crack is the result of a complex interplay between the initial quenched disorder of the material and the heterogeneities created by the fracture as it evolves. Disorder is then a crucial ingredient in the development of cracks since defects or voids are usually precursors of fracture and have a large impact on the strength of the samples.

The perspective of applying to fracture the well-known toolbox of statistical physics for disordered systems seems promising. The irreversibility of fracture, the presence of long-range interactions, the experimental evidence of the self-affine rough nature of the fracture surfaces [Bonamy 2009] as well as the presence of long-tailed distributions in some of the variables involved -with exponents that might be universal- [Garcimartín et al. 1997, Guarino et al. 2002; 1998, Maes et al. 1998, Salminen et al. 2006; 2002], have put fracture into the critical phenomena jumble. The big question is whether fracture can be explained as a phase transition or not. Some approaches have tried to link it to other well-established theories like line deppining [Bonamy 2009], percolation (see [Alava et al. 2006] and references therein) or nucleation [Griffith 1921, Rundle and Klein 1989, Selinger et al. 1991, Wang et al. 1991] but the question still remains open.

In general, the aim of the statistical mechanics approach to fracture or plasticity is to find the universal laws behind the problem, exploring tractable models that can capture the basic features of the phenomenon. Due to the

relevant role of the heterogeneity, a desirable characteristic for these models is that disorder could be introduced and varied in a straightforward way.

One of the usual simplifications is to discretize the medium at a level where one can get rid of the atomic interaction and make use of the elastic equations 2.17 on elements that represent a coarse-graining of the smaller length scales. This coarse-grained description ignores irrelevant microscopic details and focuses on capturing the scaling laws of the system on large length scales. It is not a discretization of the equations like the finite elements methods but a discretization of the medium itself into discrete physical entities. In the last twenty five years several models of this kind have been introduced and much insight has been gained. Next, common characteristics of these models and the most extended variants will be described.

2.2.1 Discrete models

Lattice models describe solids at a mesoscopic level, with elements that represent the average behavior at that scale. These mesoscopic elements are connected to other similar neighboring elements forming a lattice. This approach transforms the partial differential equations 2.17 in a system of coupled linear equations. Since the equilibrium equations 2.17 are local, the physics at the mesoscale may be modeled by a lattice of elements that interact with their neighbors in the lattice. Each element displays very simple elastic and breaking characteristics (usually a linear constitutive law up to a failure threshold) and the system has a few control parameters. A certain rule for breakdown or plastic behavior must also be included in the model. The loading is imposed in a very simple way on the boundary of the lattice. Vectorial models allow for the imposition of different loading conditions. The three basic modes of fracture in which any load can be decomposed are shown in figure 2.4.

The aim is to study the emergence of macroscopic collective behavior in the presence of disorder which is introduced by imposing different constitutive laws on the elements. Disorder can be either quenched, *i.e.*, static and time-independent, or annealed, *i.e.*, the heterogeneities caused by the evolution of the system affect the disorder, that evolves too. Quenched disorder is usually introduced distributing the failure thresholds according to a certain probability distribution, simulating fluctuations in the material strength. Dilution, which can model the porosity of the material or the number of previous defects present, has been extensively used to study fracture in the context of percolation. The effect of disorder in the elastic modulus has also been studied and can be viewed as a study of heterogeneous materials [Alava et al. 2006].

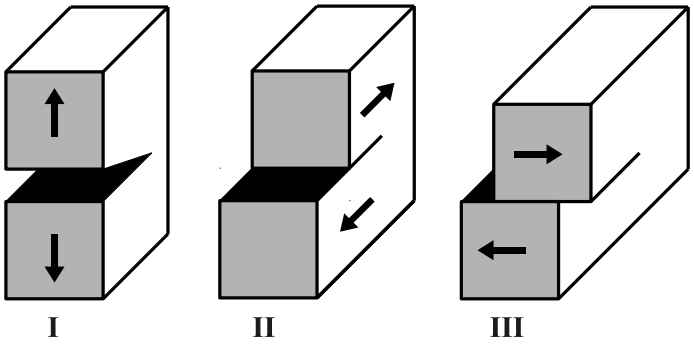

Figure 2.4: The three modes of loading. On the left, mode I (opening mode) where only tensile stress is present. Mode II (sliding mode) in the center corresponds to in-plane shear (a shear stress acting parallel to the plane of the crack and perpendicular to the crack front) and on the right, mode III (tearing mode) or out-of-plane shear loading (a shear stress acting parallel to the plane of the crack and parallel to the crack front).

An early attempt for a lattice model is the Fiber Bundle Model introduced in [Daniels 1945]. It consists of a set of fibers arranged in parallel with thresholds distributed according to a probability distribution and subject to tensile load. Once a fiber reaches its threshold, it irreversibly fails. The load can be redistributed locally among its neighbors (local load sharing) or equally among all the fibers in the system (equal load sharing), giving rise to a mean field (MF) model.

Most of the vectorial lattice models consist of a network of springs that connect nearest neighbors. Depending on the model, these springs are only allowed to stretch (central forces) or both stretch and bend (bond-bending forces). These two forces are present in the Bond-Bending Model [Sahimi and Arbabi 1993a;b] described by the Hamiltonian:

$$H = \frac{\alpha}{2} \sum_{ij} K_{ij} [(\mathbf{u_i} - \mathbf{u_j})\mathbf{e}_{ij}]^2 + \frac{\beta}{2} \sum_{jik} K_{ij} K_{ik} (\delta\theta_{jik})^2. \tag{2.18}$$

The first term is the central force term that governs the stretching and compressing of a spring, $\mathbf{u_i}$ is the displacement of node i, K_{ij} is the elastic constant of the bond between i and j, and $\mathbf{e_{ij}}$ is a unit vector in the direction $i - j$. If this were the only term present, we would have the Random Spring Model [Arbabi and Sahimi 1993, Nukala et al. 2005b].

The second term represents the changes in the angles between the springs due to the bond-bending forces, $\delta\theta_{jik}$ is the angle between two bonds ij and ik whose common vertex is i. The Bond-Bending Model is a rotationally invariant correction to the old Born Model [Kantor and Webman 1984].

Close to the Bond-Bending Model falls the Beam Model [Roux and Guyon 1985]. Between every two neighboring nodes, one places a beam characterized by an area, a moment of inertia and a certain Young and shear modulus. This allows to calculate the longitudinal and shear forces and the torque on the beam. The yield criterion takes into account both elongation and flexion since a beam can break by either of the two mechanisms and has different breaking thresholds in each case, assigned from a certain probability distribution.

So far we have discussed vectorial lattice models. In the following section we will introduce one further simplification, reducing our problem to a scalar lattice model.

2.2.2 A scalar analogue to elasticity

The equation of equilibrium of a body 2.17 resembles the Laplace's Equation, one of the possible expressions of charge conservation:

$$\nabla^2 V = 0. \tag{2.19}$$

The role of the vectorial displacement $\mathbf{u}$ in equation 2.17 is played here by the voltage V, a scalar variable. Besides, in the same way that Hooke's Law models the ideal linear elastic behavior of solids, Ohm's Law is the equivalent linear relationship for electric conductors:

$$i = kv. \tag{2.20}$$

The role of the elastic modulus is played here by the conductivity k, the voltage v is, as we said, equivalent to the displacement, and hence the current i is equivalent to the force in the elastic problem. The Ohm's law can also be expressed in terms of scalar stress and strain variables, equivalent to equation 2.9:

$$\mathbf{J} = k\mathbf{E}, \tag{2.21}$$

where the current density $\mathbf{J}$ and the electric field $\mathbf{E}$ are respectively equivalent to mechanical stress and strain.

Therefore, equation 2.19 is a partial differential equation that corresponds to a particular case of the vectorial Lamé Equation 2.17 where only the scalar

component is taken into account, thus representing scalar elasticity and reducing the complexity of the original equation.

One of the drawbacks of this simplified version with respect to the vectorial models is that, while in the former a wide variety of boundary conditions can be imposed and therefore many different loading conditions can be modeled, this scalar analogue can only mimic antiplane shear.

The discrete formulation of charge conservation turns equation 2.19 into the Kirchhoff Current Law (KCL). This discretized version of the electric problem in a lattice is the basis of the well-known Random Fuse Model (RFM) [de Arcangelis et al. 1985], corresponding to a scalar field in the Hamiltonian of the Random Spring Model seen in the previous section. The RFM will be described in detail in the following section.

2.3 The Random Fuse Model

This model was first introduced in [de Arcangelis et al. 1985] with the idea of having a simple model, easy to simulate yet including the basic ingredients of fracture. It consists of a network of fuses like the one shown in figure 2.5 subject to an external voltage difference between two horizontal bus bars.

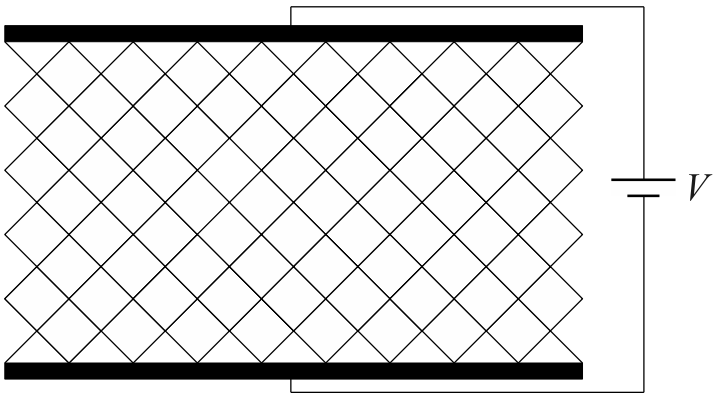

Figure 2.5: Random fuse network on a diamond lattice of lateral size $L = 9$, *i.e.*, $2L(L+1) = 60$ fuses. A voltage source V is imposed between top and bottom bus bars and periodic boundary conditions are set in the transverse direction.

We can obtain the equivalent stress σ and strain ϵ variables in this 2D discrete scalar scenario simply recalling the definition given in the previous

section:

$$\sigma = I/L_x$$
$$\epsilon = V/L_y, \tag{2.22}$$

where L_x (L_y) is the system size in the horizontal (vertical) direction that in the diamond lattice case is $L_x = 2L$ ($L_y = L + 1$).

Every fuse ij –attached to nodes i and j– in the system obeys Ohm's law given by equation 2.20 with a certain conductivity k up to a characteristic threshold current i_{ij}^{th} as it is shown in figure 2.6. Once this threshold is reached, the fuse can behave either *brittle* (left panel) or *ductile* (right panel). The ductile case was studied for the first time in [Hansen et al. 1991] and will be addressed in detail in Chapter 4. In the classic brittle case, ohmic (elastic) fuses are burnt (broken) as soon as its local threshold is reached and irreversibly become insulators ($k = 0$) from then on.

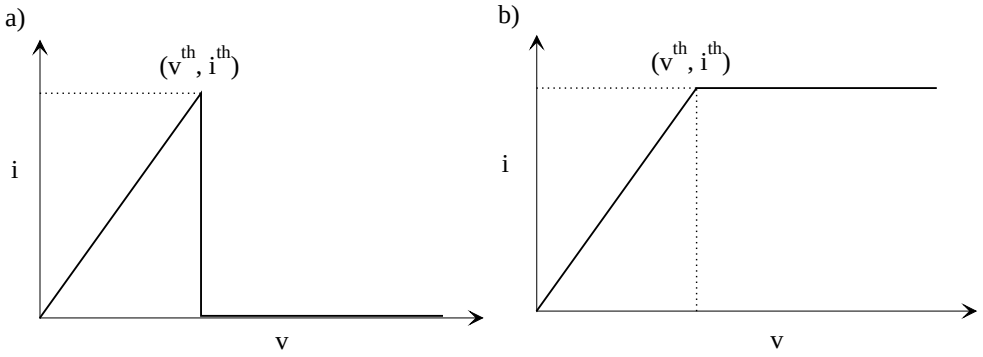

Figure 2.6: Current-voltage characteristics of a fuse. On the left, brittle behavior. On the right, ductile behavior.

The external voltage is slowly increased and therefore the local voltages increase proportionally. At some point, one fuse reaches its threshold and becomes an insulator. The currents are then redistributed according to the KCL to equilibrate the lattice again, so the entire system needs to be updated every time a fuse is burnt. This model assumes that the dynamics of the rupture of bonds is much slower than the dynamics of the currents in the network to relax to their new equilibrium state so that we can suppose that it happens instantaneously.

When a sufficiently large number of bonds have been broken, a continuous interface of insulators will appear from left to right, preventing the flux of

current from top to bottom and hence disconnecting the system into two independent parts. This is obviously characterized by a total conductance $K = 0$ and equivalent to a macroscopic fracture in an elasticity framework.

First developed as a conducting-insulator network with an evolving density of fuses p, the RFM took its actual form as a fully-occupied network with disorder in thresholds in [Kahng et al. 1988]. This kind of disorder is introduced by picking the threshold currents from a certain probability distribution. As said above, one of the advantages of lattice models is that introducing disorder is relatively easy. This has made possible a number of studies on the influence of disorder in the RFM [Alava et al. 2006] depending on how it is introduced (dilution, disordered thresholds or conductivities) and the effect that the form of the probability distribution has on the fracture process. Annealed disorder, describing a changing medium as fracture develops, has also been treated in [Sornette and Vanneste 1992].

The influence of lattice geometry (square, triangular and diamond lattices) has also been studied and no significant changes have been found [Alava et al. 2006]. Diamond lattices (square lattice with a tilt of 45 degrees) are used all through this thesis because we like the fact that this setup does not introduce any initial bias, *i.e.*, all the fuses carry the same current when the lattice is intact.

The RFM has been used to study strength, damage localization, avalanches, and almost all the relevant issues regarding fracture, becoming the paradigm of minimal fracture models [Alava et al. 2006]. Some of these properties have been tested against more complicated vectorial models [Nukala et al. 2005b] finding similar results and no significant differences. In the following section we will discuss in detail the implementation of the RFM for brittle fracture while the elastic-perfectly plastic version of the RFM will be described in Chapter 4.

2.3.1 Kirchhoff equations and iteration process

Our basic setup is shown in figure 2.5. It consists of a diamond network of fuses, each of them behaving brittle (see left panel of figure 2.6). All the fuses have the same conductivity $k = 1$ and the disorder is introduced in the thresholds, which are obtained from a uniform distribution $i^{th} \in (0, 1)$.

The horizontal top and bottom borders of the network are busbars where a voltage difference V is imposed by applying a voltage source to the top bar

and connecting the bottom to ground. Vertical borders are constrained by periodic boundary conditions.

We can write the KCL along with the Ohm's Law for each node in the network. The solution of this system of linear equations will give us the local voltages at each node. It must be taken into account that there are two types of nodes: *bulk nodes*, connected to other four neighboring nodes and *boundary nodes*, attached to busbars as it is sketched in figure 2.7.

The KCL, expressing the conservation of charge, states that the sum of the currents flowing into a node is equal to the sum of the currents flowing out of that node. Adopting the convention that currents flowing into the node are taken to be positive, and currents flowing out of the node are negative, this principle can be enunciated as $\sum_{m=1}^{n} i_m = 0$, n being the total number of branches that converge into the node.

Therefore, given the current flows depicted with grey arrows in figure 2.7, we have equations 2.23 a,c for boundary nodes (figure 2.7 a,c) while for bulk nodes (figure 2.7 b) we obtain equation 2.23 b.

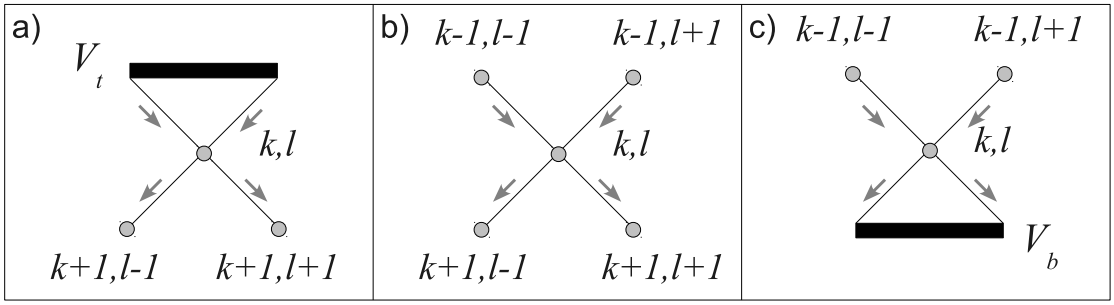

Figure 2.7: a) Node kl attached to top busbar. b) Node kl surrounded by other four neighboring nodes. c) Node kl attached to bottom busbar.

$$\begin{aligned}
&\text{a)} && 4kV_{k,l} - kV_{k+1,l-1} - kV_{k+1,l+1} = 2kV_t \\
&\text{b)} && 4kV_{k,l} - kV_{k-1,l-1} - kV_{k-1,l+1} - kV_{k+1,l-1} - kV_{k+1,l+1} = 0 \\
&\text{c)} && 4kV_{k,l} - kV_{k-1,l-1} - kV_{k-1,l+1} = 2kV_b.
\end{aligned} \tag{2.23}$$

In our case, the top busbar potential is $V_t = V = 1$ and $V_b = 0$ for the bottom busbar. For a lattice with $L \times L$ nodes, applying the KCL to each node

we will obtain a system of L^2 equations and L^2 unknowns (local voltages) that can be expressed as a matrix equation:

$$\mathbf{Kv} = \mathbf{b}, \tag{2.24}$$

where $\mathbf{v}$ is the solution vector with the L^2 local node voltages, $\mathbf{b}$ is the applied voltage source vector and $\mathbf{K}$ is the conductivity matrix. The resulting $\mathbf{K}$ matrix is symmetric and positive definite. It is known that this kind of matrices can be decomposed into a lower triangular matrix $\mathbf{L}$ and its transpose $\mathbf{L}^T$ (Cholesky decomposition). Besides, it happens to be a very sparse matrix, having at most four nonzero non-diagonal elements. When a given fuse burns, the conductivity of that fuse changes from $k = 1$ to $k = 0$. This only affects the two nodes it is attached to or, in case it is a boundary fuse, to one node and one entry of the voltage source vector. This means that every burning only affects a few entries of the $\mathbf{K}$ matrix and with a very specified pattern that does not affect the symmetry of the matrix and makes it even more sparse.

Due to the fact that the equations are linear, it is easy to see that the simulation algorithm can be sped up between two burning events since the only effect of any increment of the external voltage is to scale the local voltages by the same factor. We call the initial external voltage V_0. The fuses carry initial currents i_{ij}^0 and the thresholds are set to i_{ij}^{th}. Any external increment λV_0 will translate into $\lambda k i_{ij}$. Hence we can calculate the factor λ needed to burn the fuse closest to its threshold:

$$\lambda^{-1} = \max_{ij} \left(\frac{i_{ij}}{i_{ij}^{th}} \right), \tag{2.25}$$

and the external voltage can be set constant to $V = 1$, taking into account that the burning events actually occur at an external voltage $V = \lambda$.

Therefore, the update scheme is the following: solve the KCL system to calculate the local currents, apply equation 2.25 to determine the next fuse to blow. Then, update the system turning the chosen fuse to insulator and go back to the first step, recalculating the currents.

Although the linearity of the system saves us a huge amount of recalculations between two consecutive voltage increments, applying standard relaxation methods to solve the linear system only each time a fuse burns is not efficient due to their high computational cost. Furthermore, these techniques suffer from a kind of *critical slowing down* since the number of iterations needed for the system to relax to the solution grows faster than the volume

as the system approaches breakdown. In the past, Fourier-accelerated Conjugate Gradient Methods [Batrouni and Hansen 1988] with preconditioning were the best option for this kind of problem involving a vast number of linear equations. However, a new method was recently introduced in [Nukala and Simunovic 2003, Nukala et al. 2005a] that takes advantage of the sparsity and the peculiar structure of the conductivity matrix. A brief description of this method will be outlined in section 2.3.2.

2.3.2 Rank-one sparse Cholesky downdate

As we have seen in the previous section, the conductivity matrix $\mathbf{K}$ is symmetric and positive definite. This means that a Cholesky factorization may be performed:

$$\mathbf{K} = \mathbf{L}\mathbf{L}^T \tag{2.26}$$

or

$$\mathbf{K} = \mathbf{L}\mathbf{D}\mathbf{L}^T, \tag{2.27}$$

where $\mathbf{L}$ is a lower triangular matrix, and a forward substitution followed by a back-substitution will give us the solution vector $\mathbf{v}$ of equation 2.24.

Following a naïve approach, this process should be repeated till breakdown, recalculating the Cholesky factors each time a fuse is burnt and therefore the conductivity matrix changes. For large system sizes, this would need a huge number of refactorizations and, even taking advantage of the sparsity of the matrix, it would be computationally expensive. However, as said before, these burnings imply a small and well-known change in the matrix. In fact, burning the $(n+1)$th fuse ij attached to nodes i and j involves a modification of $\mathbf{K}_n$ (corresponding to n missing fuses) that can be expressed in the form:

$$\mathbf{K}_{n+1} = \mathbf{K}_n - k_{ij}\mathbf{w}_{ij} \cdot \mathbf{w}_{ij}^T, \tag{2.28}$$

with

$$\mathbf{w}_{ij}^T = (0 \dots 0 \underset{i}{1} 0 \dots 0 \underset{j}{-1} 0 \dots 0). \tag{2.29}$$

If one of the nodes, say i, is prescribed, as it is the case when the fuse is attached to the busbars, the load vector $\mathbf{b}$ is also affected and the update of the system can be expressed as:

$$\mathbf{w}_j^T = (0 \dots 0 \ \underset{j}{-1} 0 \dots 0) \tag{2.30}$$

$$\mathbf{b}_{n+1} = \mathbf{b}_n - \mathbf{w}_j^T. \tag{2.31}$$

In any of the two cases, the conductivity matrix is modified only by a rank-one matrix. Given the sparsity of the matrix, it is much more efficient to apply the corresponding rank-one downdate to the Cholesky factor instead of recalculating it completely. This can be done thanks to the [Davis and Hager 1999] algorithm that takes into account the change in the sparsity pattern of the matrix and the Cholesky factor. It is based on the analysis and manipulation of the underlying graph structure and it is computationally optimal since it depends only on the nonzero entries that change in each update/downdate. An implementation of this algorithm can be found in [Chen et al. 2008].

Once we have the new factor, the solution vector can be obtained by a simple backsolve. This scheme surpasses in more than two orders of magnitude in computational time the preconditioned conjugate gradient methods with Fourier acceleration [Nukala and Simunovic 2003].

Instead of updating the Cholesky factors after each fuse breaking, we could use the [Davis and Hager 2001] algorithm for multiple-rank updates to modify the Cholesky factor only after a certain number of burnings. In the meantime, the solution vector is obtained making use of the Sherman-Morrison-Woodbury formula [Nukala and Simunovic 2003]. Although a multiple-rank update is more efficient than several consecutive rank-one updates [Davis and Hager 2001], it turns out that the complete process of updating the solution by making use of the previous solution vector is less efficient than consecutive rank-one updates [Nukala and Simunovic 2003]. Therefore, the rank-one scheme has been used throughout this Thesis.

Chapter 3

Energy Dissipation in Brittle Fracture

When a system breaks, the accumulated elastic energy is released through several dissipative mechanisms as heat, stress waves and acoustic emission (AE). The latter, besides being a very useful tool to extract information of the microcracking process in materials, is very interesting itself since it is a an example of a broader phenomenon known as *crackling noise* [Sethna et al. 2001] that reveals similarities in the behavior of, a priori, very different systems.

Here we will focus on brittle or quasi-brittle materials. There are many materials of technological interest that behave brittle at least in a certain range of temperatures. Finding reliable indicators of an upcoming failure or how the presence of disorder in the material affects its response to loading are relevant issues from both the theoretical and the technological points of view. The mixture of fundamental open questions and its direct impact on applications makes this subject very appealing.

In this chapter we will begin with an introduction to *crackling phenomena* and a description of the experimental facts of AE and the insight gained with models. We will finish describing our contributions to the field [Picallo and López 2008]. We have compared different energy estimators and derived scaling relations that account for their statistical behavior. We have also been interested in the temporal evolution of the energy distribution to elucidate whether there are any indicators that could be used to predict the proximity

of final failure. Finally, we have relaxed the quasistatic loading condition to mimic dynamic fracture.

3.1 Introduction

A system crackles in response to an external driving, leading to energy dissipation in the form of avalanches of events with no characteristic size. A typical example is the Barkhausen effect in ferromagnets [Durin and Zapperi 2005]. At microscopic scale a magnet is composed of domains of spins with the same orientation. When an external magnetic field is applied, the domains reorganize and tend to orientate parallel to the field. It is observed that, when imposing a slowly changing external field, the net magnetization does not vary smoothly with the field but in irregular steps associated with fluctuations in the movements of the domain walls, mainly due to the disorder in the material. The resulting avalanches are self-similar and its duration and size follow scale-free distributions

$$\begin{aligned} \mathcal{P}(t) &\sim t^{-\alpha} g(t/t_0) \\ \mathcal{P}(s) &\sim s^{-\tau} g(s/s_0), \end{aligned} \tag{3.1}$$

where α and τ are critical exponents that take values $\alpha \simeq 1.5 - 2$ and $\tau \simeq 1.3 - 1.5$ for different materials.

The scale-free behavior suggests that this phenomenon should depend neither on the microscopic nor on the macroscopic structure of the system, since the same kind of behavior is observed at very different scales. Moreover, signatures of this sort of crackling noise appear in completely different systems.

A macroscopic example of crackling noise is found in the slow friction of the tectonic plates which suddenly produces abrupt releases of energy in the form of earthquakes. The absence of a characteristic size in earthquakes was expressed in the Gutenberg-Richter frequency-magnitude relationship that measures how often earthquakes of a given size occur. This scale-free behavior is reflected in the probability distribution of the seismic energy[1] released in the earthquake that follows a power law

$$\mathcal{P}(E) \sim E^{-\beta} \tag{3.2}$$

[1]The original formulation of the law by Gutenberg and Richter used by the geophysics community states that $\mathcal{P}(M) \sim e^{-bM}$ where the magnitude M is related to the seismic energy by $log_{10}E = 1.5M + 11.8$ and hence the exponents β and b are related by the expression $b = 1.5(\beta - 1)$.

with an exponent $\beta = 1.7$ [Utsu 1999]. The universality of this value is still controversial [Godano and Pingue 2000, Pacheco et al. 1992, Utsu 1999]. As occurs with the Barkhausen noise (equations 3.1), earthquakes also exhibit self-similarity in time and there is a power law relating the time intervals between the main shock and the subsequent aftershocks. This is known as the Omori Law.

$$\mathcal{P}(t) \sim t^{-\alpha} \tag{3.3}$$

with $\alpha \simeq 1.0$. We will see in the next subsection that similar laws appear in the AE from brittle fracture.

We could add examples coming from physics at very different length scales: crumpling paper [Houle and Sethna 1996], martensitic transitions [Bonnot et al. 2008], vortices in type II superconductors [Field et al. 1995], plastic deformation of materials [Miguel et al. 2001], etc. All these systems share in common that they have many degrees of freedom and respond to a slow external driving with a jerky succession of discrete events in space and time without any characteristic scale. This scale invariant behavior and its universality makes it appealing to search for the minimal ingredients that give rise to this behavior, since it seems that only symmetries and conservation laws should be involved in the phenomenon.

3.1.1 Experimental measures of acoustic emission in fracture

The sound produced when tearing a sheet of paper is an everyday verification of the existence of AE in fracture. The AE signal is comprised of a series of discrete events of a certain duration separated by intervals of silence, which are called *waiting times*. This is yet another example of crackling noise and its statistics is again nontrivial. It was first suggested in [Scholz 1968] that a small-scale analog of the earthquakes statistics should be found in the time series of AE from materials under stress as they are slowly driven towards catastrophic failure. Indeed, equations 3.2 and 3.3 for earthquakes have their counterpart in the context of fracture in the distribution of energy of the acoustic events and the distribution of waiting times, respectively.

AE is produced by a sudden release of elastic energy in the form of acoustic waves when a material is subjected to an external stress. The release of acoustic energy is related to microcracking (or plastic deformation, as will be addressed in the following chapters) and hence a most interesting feature of AE is that it gives an indirect measure of the microscopic damage accumulated in the material. This is why it has long been used as a non-destructive test

to scan materials in real time with industrial purposes (pipelines and vessels inspection, automatic crack detection during manufacturing processes, etc.).

The classical setup in an AE experiment (see for instance [Garcimartín et al. 1997]) makes use of piezoelectric crystal sensors attached to the specimen to detect the acoustic waves and transform them into an electrical signal. The energy of the acoustic events is calculated by summing the square of the amplitude of the received electrical signal and integrating it over the duration of an event. There exists a lower cutoff in the range of detectable events since a detection threshold must be imposed with a certain criterion to filtrate off the signal and avoid spurious events due to the noise present in the setup.

The sound attenuation in its way from the AE source to the transducers must also be taken into account since only if there is no attenuation in the material the output of the electronic device is proportional to the energy of the AE. This means that either the material employed has a small attenuation coefficient or either the position of the microfractures must be taken into account to calculate their energy. The transfer time of the acquisition system must also be shorter than the usual inter-event times to avoid losing events during this dead time.

With similar setups, tensile tests performed in a variety of materials (granite [Lockner et al. 1991], wood and fiberglass [Guarino et al. 1998], sandstone [Davidsen et al. 2007], plaster [Petri et al. 1994], (fiber-reinforced) concrete [Niccolini et al. 2009], paper [Salminen et al. 2002], etc.) found $\beta \sim 1-2$ and $\alpha \sim 1-1.5$. Neither the energy exponent β nor the temporal exponent α seem to be universal, exhibiting a considerable spread in the values depending on the material and the experimental conditions. The influence of loading the sample with a stress or a strain driving was studied in [Guarino et al. 1998]. The main difference between the two is that a strain driving allows stable crack growth after the critical stress while stress driving produces catastrophic failure. However, no differences were found in the statistics prior and post peak load in [Salminen et al. 2002] and no differences were found in [Guarino et al. 1998] between the two types of driving. The strain rate did not seem to affect the results either [Kuksenko et al. 2005, Salminen et al. 2002].

Placing several sensors on the sample, one can measure the differences in the arrival times of the signals and triangulate to detect the source of the noise where the microcrack was produced and, hence, determine the localization of the damage in the sample. The main source of error of this technique comes from the uncertainties in the determination of the arrival times. This method allowed to explore the localization of brittle fracture in granite [Lockner et al.

1991] and in plaster and wood [Garcimartín et al. 1997, Guarino et al. 1998]. Acoustic events were shown to be diffuse and damage uniform at the beginning of the process while the sample was being loaded up to the peak stress and then nucleate into a growing fault. In [Garcimartín et al. 1997] this was quantified through a measure of the Shannon entropy at different stages of loading.

In typical experiments, the crack is difficult to control once it is initiated and the failure happens in a catastrophic sudden way. That is why several setups, in which the crack propagates in a quasistatic fashion, have been developed[2]. In [Lockner et al. 1991] they adjusted the load applied to the sample to keep the acoustic emission rate constant and hence the crack growth after the critical stress could be observed under quasistatic conditions. Stable crack growth was also studied for paper in [Salminen et al. 2006] in a tensile peeling in nip setup. There, the post-failure stress curve could be followed quasistatically instead of occurring violently and the crack can be observed under quasistatic conditions. They obtained complex correlations in the waiting time distributions and an energy exponent $\beta = 1.8$ higher than the usual values for paper [Salminen et al. 2002]. Relating AE energy to local crack dynamics or the mechanical energy released is a difficult issue [Rosti et al. 2009]. To this aim, AE in simpler setups has been studied. In [Måløy et al. 2006] the propagation of a planar crack in a 2D sheet between two sealed Plexiglas plates was followed with the help of a CCD camera. Image analysis was performed to extract the length of the crack and quakes were defined as connected zones with a velocity above a certain threshold. With this setup, regardless of the threshold selected, both α and β took universal values similar to the exponents observed in real earthquakes.

Another relevant issue that inspired part of our work (to be described in section 3.2) is the fact that the acoustic signal is not stationary: acoustic events at the final stages of fracture are much more energetic than the initial events. Due to the non-stationary nature of the fracture process, the internal state of the material is constantly evolving till the final breakdown. This time evolution is not captured by the energy and waiting time distributions since they are typically measured integrating during the whole process. Indeed, in [Guarino et al. 1998] it was found that the energy exponent was not constant during a run of the experiment. They observed that the exponent of the events corresponding to the early stages of the process was slightly bigger than the exponent corresponding to the final events of the same run. Previously, [Lockner et al. 1991] had observed a minimum in the β value during the

[2]Out of the scope of this chapter are creep experiments [Koivisto et al. 2007, Santucci et al. 2004] in which a constant load is imposed.

nucleation of the crack. A systematic decrease in the β exponent to the value $\beta = 1$ has been found in [Carpinteri et al. 2009] as the failure was approached and a remarkable decrease in the β exponent was also observed in [Kuksenko et al. 2005]. These facts call for a deeper analysis that reflects the evolution of the system as it approaches breakdown.

A different analysis was carried out in [Rosti et al. 2010] discussing in detail the possible criticality signatures in tensile paper tests with and without a previous notch. They studied how the statistical distributions of energy and waiting times change in relation to the critical time at which the energy release rate reaches its maximum value. The energy distribution changes slightly around the critical time. However, these changes in the distribution are not as remarkable as the complex variations changes observed in the waiting time distribution.

A good knowledge of the temporal behavior of the relevant quantities in fracture could have failure forecasting prospects. More experiments are currently needed to extract reliable conclusions and to understand the puzzling differences in the experimental observations.

3.1.2 Numerical and theoretical approaches

Lattice models qualitatively reproduce the avalanches of activity observed in real experiments. As the external load is slowly increased, weak elements fail to hold the imposed local stress and break. Some internal load redistribution mechanism, whose details depend on the particular model, increases the local stress on the remaining elements and may cause further simultaneous local failures. As a result, the material may respond in avalanches of failure events whose size distribution is often very broad.

The size of the avalanche s is defined as the number of bonds involved in the avalanche. As it happens in the experiments, either a stress or a strain driving can be imposed but no significant differences are found. The avalanche signal is jerky and events of all sizes appear till the final avalanche, an enormous catastrophic event that corresponds to the formation of the macroscopic fracture. This is usually studied separately and it is known to follow a Gaussian distribution [Zapperi et al. 2005b].

There exist mean field predictions obtained with the Fiber Bundle Model [Hansen and Hemmer 1994, Hemmer and Hansen 1992] that indicate that the avalanche size distribution $P(s)$ is power-law shaped with an exponent $\tau = 5/2$. Restricting ourselves to loads smaller than the critical load the dis-

tribution of avalanche sizes exhibits an exponent $\tau = 3/2$ with an exponential cutoff dependent on the imposed load. It is only when the critical load is reached that the distribution exponent takes the value $\tau = 5/2$. However, the diverging cutoff may obscure this sharp transition and it can be interpreted as a smooth crossover [Pradhan et al. 2005; 2006]. This will be discussed in detail in the next section.

In the RFM, simulations suggest an avalanche distribution of the form

$$\mathcal{P}(s, L) \sim s^{-\tau} g(s/L^D), \tag{3.4}$$

with values for the avalanche exponent bigger than the MF predictions. Moreover, these values do not seem to be universal. In particular, for diamond lattices $\tau = 2.75$ while for triangular lattices $\tau = 3.05$ [Zapperi et al. 2005b]. In contrast, simulations in three dimensions suggest universality and exponents closer to the mean field values [Zapperi et al. 2005a], possibly indicating that, as it happens in critical phenomena, the results are closer to MF in higher dimensions.

Several studies have focused on the statistics of avalanches of failure events in lattice models [Hansen and Hemmer 1994, Pradhan et al. 2006, Zapperi et al. 1997; 1999] and improved simulation algorithms have recently allowed to study larger systems with much better statistics [Zapperi and Nukala 2006, Zapperi et al. 2005a;b]. In general, lattice models typically predict larger energy exponents β than those obtained in experiments. These numerical results evaluate the avalanches of events, each event being a microfracture. In contrast, experiments measure energy distributions through the AE signal. Direct estimations of the energy distributions in models are scarce and its connection with the quantities measured experimentally is not clear yet. A relationship between the distribution of events and the energy distribution was studied in [Minozzi et al. 2003] in a scalar model for dynamic fracture. Very recently, several tests for criticality under uniaxial compression were performed finding an energy exponent $\tau = 2.75$ in agreement with the results that will be shown in the next section where several definitions of energy will be discussed within the framework of the RFM, as well as their possible universality, the absence of time scale separation and the signatures of imminent failure.

3.2 Results

In the following sections we explain in detail our research work in the problem of AE in fracture published in [Picallo and López 2008].

Energy dissipation in the RFM occurs in bursts of breaking events which can be compared with the AE observed in experiments. In doing so, one is assuming that the main contribution to AE is given by the dissipated elastic energy. Also, it is worth to keep in mind that in real systems one expects that only a fraction of this dissipated energy leads to the AE observed, while the remaining losses are due to other dissipative mechanisms which are not described by purely elastic models like the RFM. Several ways to define the dissipated energy can be envisaged as we discuss below.

- **Global Energy:** A global definition assumes that the whole volume of the system contributes to the dissipated energy. The electric power dissipation in the fuse model is the product of the voltage drop across the network and the total current that flows through it. The power dissipation in the electrical model can be seen as an equivalent to the stored elastic energy in a mechanical system. In [Pradhan et al. 2006] they found that $\beta = 2.7$ for the RFM on diamond lattices under stress loading conditions and a similar energy definition.

- **Macroscopic Energy:** Alternatively, we can define the energy lost during a given avalanche event n as

$$E_n \sim V_n^2 \Delta G_n \sim V_n^2 s_n, \tag{3.5}$$

  where ΔG_n is the change in the elastic modulus due to the failure avalanche, s_n is the number of broken bonds (avalanche size) of the nth event, and V_n is the corresponding potential drop between the bus bars (strain imposed in the sample) [Salminen et al. 2002]. This definition makes use of the global strain imposed on the system and can be seen as a coarse-grained or macroscopic measure of the dissipated energy.

  Note that both global and macroscopic definitions of the dissipated energy take into account the whole volume of the system. However, there is strong experimental evidence indicating that AE is actually a localized phenomenon in space and time so that energy release actually occurs at microfractures [Garcimartín et al. 1997, Guarino et al. 1998], and it is not therefore spread across the system. This suggests one should consider other ways to define the dissipated energy in the model, in particular, it may be interesting to study measures of released energy that are directly linked to the bonds involved in avalanches of local breaking events. In this spirit, we introduce the next definition of dissipated energy.

- **Microscopic Energy:** It is defined as the sum of the energy losses at every element of the system involved in the nth failure avalanche. This can be calculated by adding up the energy dissipated by each individual broken bond, $\epsilon_{ij} = i_{ij}^2/k_{ij} = k_{ij}v_{ij}^2$, where v_{ij} is the local potential drop at bond ij, i_{ij} is the current through it and k_{ij} is its conductivity. Since fuses break right at the threshold we can define the *microscopic* dissipated energy due to the nth failure avalanche as

$$E_n = \sum_{ij}^{s_n} (i_{ij}^{\text{th}})^2, \tag{3.6}$$

  where the sum runs over each broken bond within the nth avalanche and $k_{ij} = 1$.

We devote the rest of the chapter to analyze the dissipated energy statistics in the fuse model for the case of infinitesimal strain (quasistatic model) and also under different finite strain rates (non quasistatic model). We shall be comparing the numerical results for the different measures of the dissipated energy discussed above for triangular and diamond lattices. One would expect that the three definitions give similar temporal behavior for the dissipated energy statistics, apart from constant factors. We will see that, although this is actually the case in the low energy range, dissipation statistics differs at high energies for different estimators.

3.2.1 Quasistatic case: infinitesimal strain rate

Let us first focus on infinitesimal driving. After each burning, the new current configuration is calculated according to Kirchhoff equations. This rearrangement can cause other fuses to overpass their thresholds without further voltage increase. All the fuses burnt at the same external voltage constitute an avalanche. This process is repeated until the network becomes disconnected and a macroscopic fracture like the one shown in figure 3.1 is observed.

Quasistatic dynamics results in two very well separated time scales, *i.e.*, a fast relaxation process and a slow external driving. As occurs in other systems exhibiting a well defined time scale separation (as for instance in self-organized criticality), the natural time scale is given by the slow time scale. Therefore, in the following, time refers to the number of avalanches occurred.

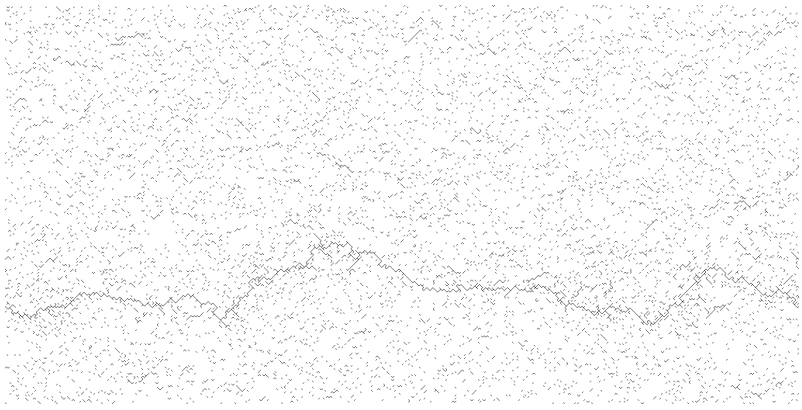

Figure 3.1: Final crack and damage in a single realization of a L=256 diamond lattice.

In figure 3.2 we show a typical realization of the temporal evolution for the dissipated energy according to equation 3.6 for different system sizes. One can see that for each realization the released energy grows in time as a power-law $E(t) \sim t^2$. At later times, fluctuations around the trend increase (the larger the bigger the system size) as the system approaches the final breakdown point. This dynamic behavior is very robust and independent of the system size or lattice type. Identical temporal behavior is found for the macroscopic dissipated energy, equation 3.5, and for the global dissipated electric energy for both diamond and triangular lattices.

In figure 3.3 we compare the temporal evolution of the ensemble average dissipated energy on the diamond lattice according to the three definitions. Notably, this behavior is also in agreement with that reported in [Minozzi et al. 2003] for a very different dynamical spring model that included acoustic waves. The origin of the robust t^2 growth law is perhaps more transparent in equation 3.5, where the driving potential is increasing linearly with time (as we are imposing a quasistatic dynamics).

The temporal power-law trend gives significant information about the functional form of the dissipated energy statistics in the RFM. The probability density function (PDF) of the dissipated energy at time τ in a system of lateral size L is given by

$$\mathcal{P}_\tau(E, L) = (1/\tau) \int_0^\tau dt\, \delta[E(t, L) - E], \tag{3.7}$$

where $\delta(u)$ is the Dirac delta distribution. This corresponds to the energy distribution to be observed after the first τ avalanche events. Note that the probability distribution $\mathcal{P}_\tau(E, L)$ is expected to be non-stationary, so it should depend explicitly on the observation time τ.

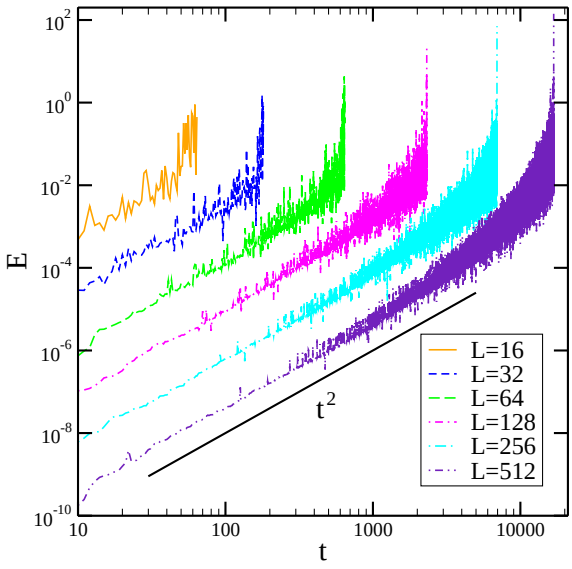

Figure 3.2: Temporal evolution of microscopic energy (equation 3.6) until breakdown for a typical realization of the disorder on diamond lattices ranging from $L = 16$ (top curve) to $L = 512$ (bottom curve). A first region with slope $\alpha = 2$ is followed by a second region dominated by fluctuations.

Let us now consider that the dissipated energy grows in time as a power-law with some exponent α,

$$E(t, L) \sim L^{-\sigma}\, t^{\alpha} + \eta(t), \tag{3.8}$$

where σ captures the scaling with system size observed in figure 3.2 and $\eta(t)$ is a noise term representing the random fluctuations around the trend.

The details of the noise term $\eta(t)$ are not known, but one can argue they may depend non-trivially on the interplay between the evolving currents and the disordered thresholds. Actually, as can be readily seen in figure 3.2, fluctuations are strongly asymmetric around the average, which immediately implies a non-Gaussian distribution of η, possibly including non-trivial correlations.

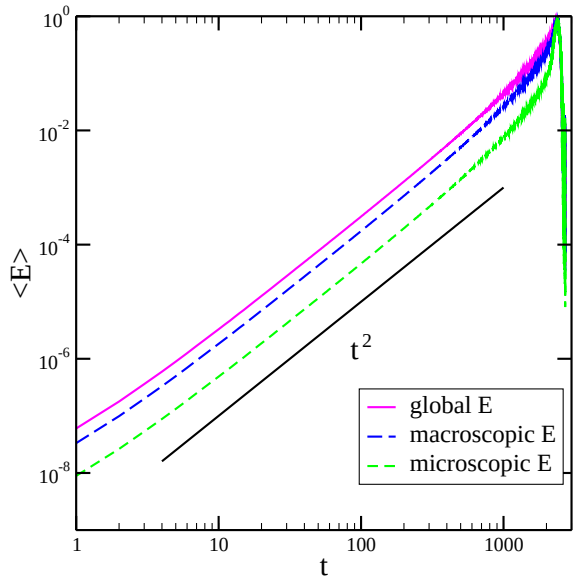

Figure 3.3: Temporal evolution of energy dissipation averaged over 10^4 realizations in a $L = 128$ diamond lattice. All the three energies, global, macroscopic and microscopic, exhibit the same t^2 trend. The three curves have been rescaled by its maximum for clarity.

Despite these difficulties one can perform the integral in equation 3.7 in certain limit, up to certain energy cut-off $E_\times$ below which fluctuations of the energy are negligible. Thus we have

$$\mathcal{P}_\tau(E,L) = \tau^{-1}\int_0^\tau dt\,\delta[L^{-\sigma}\,t^\alpha + \eta(t) - E] = \\ = \tau^{-1}L^{\sigma/\alpha}\,E^{-1+1/\alpha}\int_0^{\tau/(L^\sigma E)^{1/\alpha}} ds\,\delta[s^\alpha + \eta(L^{\sigma/\alpha}E^{1/\alpha}s)/E - 1], \quad (3.9)$$

where we made use of the change of variable $s = t(L^\sigma E)^{-1/\alpha}$. Keeping only the lowest-order term in equation 3.9 we arrive at

$$\mathcal{P}_\tau(E,L) \sim \tau^{-1}L^{\sigma/\alpha}E^{-1+1/\alpha} \quad (3.10)$$

for $\tau/(L^\sigma E)^{1/\alpha} \gg 1$. This immediately leads to the existence of a characteristic energy scale $E_\times \sim L^{-\sigma}\tau^\alpha$ above which energy fluctuations dominate the statistics. It is clear that the details of the noise statistics (including the distribution and temporal correlations) would be required to obtain the specific mathematical form of the dissipated energy distribution above the characteristic energy $E_\times$. For the RFM we have an algebraic growth with exponent

$\alpha \approx 2$ (see figure 3.2), so from equation 3.10 we expect to have an energy distribution decaying as $\sim E^{-1/2}$ for energies $E < E_\times$.

We are interested here in the distribution statistics after complete breakdown is attained. The characteristic time to total failure is expected to scale with system size as $T_{\text{break}} \sim L^z$, where z is the dynamic exponent. From equation 3.10 the energy statistics after failure, $\mathcal{P}(E, L) \equiv \mathcal{P}_{\tau=T_{\text{break}}}(E, L)$, reads

$$\mathcal{P}(E, L) \sim L^{-z+\sigma/\alpha} E^{-1+1/\alpha}, \tag{3.11}$$

for energies below a crossover energy $E_\times \sim L^{\alpha z-\sigma}$.

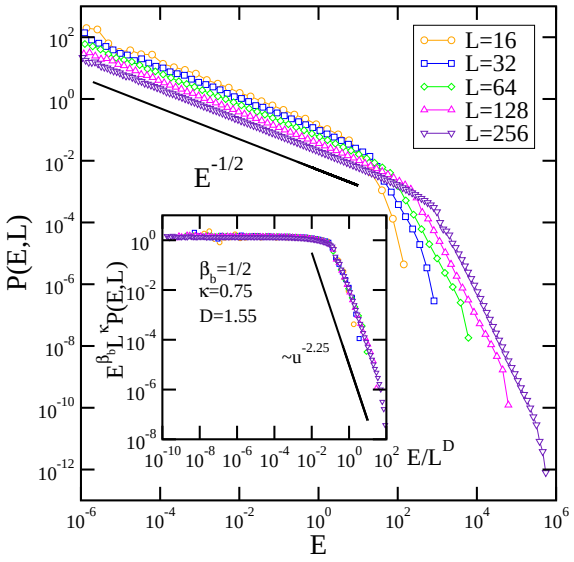

Figure 3.4: Probability distribution of the global dissipated energy for different system sizes. The low energy region decays as a power-law with exponent $\beta = 1/2$ and shows a crossover at $E_\times$. The inset shows data collapse according to equation 3.12. The values of κ and D are in good agreement with the expected relation $D = \alpha\kappa$. Logarithmic binning has been employed.

Figure 3.4 shows the probability distribution, $\mathcal{P}(E, L)$, with statistics collected up to total failure for the above introduced global dissipated energy. Two regions can be readily distinguished. The low energy statistics is in excellent agreement with a power-law decay $\sim E^{-1/2}$ over several decades in energy.

Similar behavior is observed in figure 3.5 for the macroscopic energy measure defined in equation 3.5. The dependence with system size of the numerical

data observed in figures 3.4 and 3.5 can be better characterized by means of a finite-size scaling analysis.

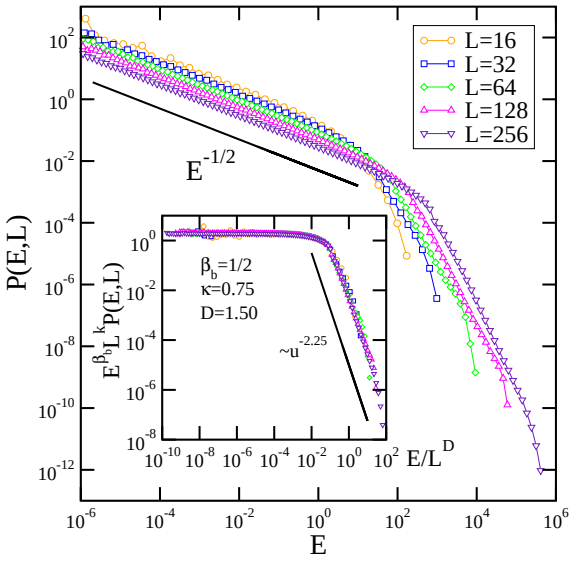

Figure 3.5: Probability distribution of macroscopic dissipated energy, equation 3.5, for different system sizes and the corresponding data collapse (inset). The same behavior and exponents as in the global definition are found.

The behavior of the energy distribution suggests the scaling ansatz

$$\mathcal{P}(E,L) \sim E^{-\beta_\mathrm{b}} L^{-\kappa} \mathcal{G}(E/E_\times), \tag{3.12}$$

where the scaling function $\mathcal{G}(u) \sim$ const for $u \ll 1$ and becomes $\mathcal{G}(u) \sim u^{\beta_\mathrm{b}-\beta_\mathrm{a}}$ for $u \gg 1$. β_a and β_b are the scaling exponents of the distribution above and below the crossover, respectively. The crossover energy scales with system size as $E_\times \sim L^D$ with some critical exponent D. We can now make use of the theoretical relation we derived in equation 3.11 to prove that the two scaling exponents κ and D are not independent. Comparing equations 3.12 and 3.11 one obtains that the following scaling relations must be fulfilled:

$$\begin{aligned} D &= \alpha z - \sigma \\ \kappa &= z - \sigma/\alpha, \\ \beta_\mathrm{b} &= 1 - 1/\alpha \end{aligned} \tag{3.13}$$

which immediately imply that $D = \alpha\kappa$. Also, according to our estimate $\alpha = 2$ from figure 3.2 we should have $\beta_\mathrm{b} = 1/2$. This reduces the number of

free exponents to achieve a good data collapse. We can also determine the dynamic exponent $z = 1.75$ by counting the average number of avalanches taking place before total failure in a system of lateral size L which should scale as $T_{\text{break}} \sim L^z$. It is interesting to note that the specific value of z is not required to produce the data collapse in equation 3.12.

The insets of figures 3.4 and 3.5 show a data collapse according to equation 3.12 with exponents $\kappa = 0.75$, $D = 1.55$ and $\kappa = 0.75$, $D = 1.50$, respectively, and the energy exponent below the crossover $\beta_{\text{b}} = 1/2$. The fit of the scaling function for $u \gg 1$ corresponds to the difference $\beta_{\text{b}} - \beta_{\text{a}} = -2.25$, and implies that the scaling exponent of the energy distribution above the crossover is $\beta_{\text{a}} = 2.75$, identical within error bars for both energy measures. This exponent is to be compared with the one calculated by Pradham *et*. al. for the electric power dissipation in the high energy region for the diamond lattice in reference [Pradhan et al. 2006], where they report $\beta = 2.7$ over two decades of energy. The macroscopic energy defined in equation 3.5 not only exhibits the same behavior but the same exponents in the two regions indicating that both definitions are completely equivalent.

However, as we show below this is not the case for the microscopic energy statistics. Figure 3.6 shows the behavior of the microscopic energy defined in equation 3.6. Recall that this measure is intended to collect only those contributions to the released energy coming from sites participating in the failure avalanche.

We find that in the low-energy region the distribution also decays as $\mathcal{P}(E, L) \sim E^{-1/2}$. However, in this case we observe that the probability does not seem to depend significatively on system size, $\kappa \approx 0$. Correspondingly, $D = \alpha\kappa \approx 0$ and the crossover energy $E_{\times}$ does not vary with system size. The lack of system size dependence of the microscopic energy may be related to the fact that the macroscopic and global estimators are sensible to the whole volume of the system, while the microscopic energy is not. The inset of figure 3.6 shows a zoom of the high energy region, where strong finite-size effects are demonstrated by the variation of the exponent β_{a} with system size. Data in figure 3.6 obviously fail to exhibit finite-size scaling.

It is worth to stress here that the PDF for all the three energy definitions exhibits identical scaling behavior at low energies, $\sim E^{-1/2}$, and is robust to changes in system size and lattice type. This universality arises from the t^2 growth law of the dissipated energy which is a feature shared by all the three definitions for any system size and lattice geometry. However, the lack

of scaling behavior with system size of the microscopic energy has a direct impact on the high energy regime of its probability distribution.

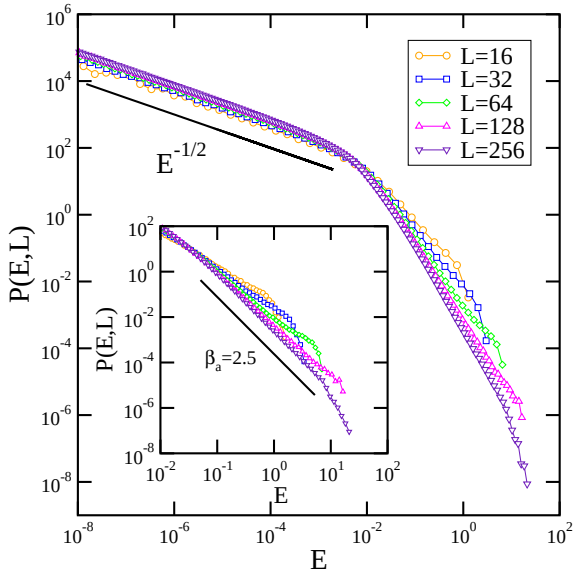

Figure 3.6: Probability distribution of microscopic dissipated energy, equation 3.6, for different system sizes. The inset shows a zoom of the high-energy region which decays with an exponent around $\beta = 2.5$ over two decades for the largest system.

3.2.2 Nonstationarity and signatures of imminent failure

The temporal series of the dissipated energy in the RFM are highly non stationary as can be easily noticed in figure 3.2, and hence the probability density $\mathcal{P}_\tau(E, L)$ depends explicitly on the observation time τ. This has been claimed to be useful to signal the onset of catastrophic failure [Pradhan et al. 2005; 2006], with evident practical applications for diagnosing damage in loaded materials. In [Pradhan et al. 2006] the power dissipation avalanche distribution for the entire breakdown process was compared with that obtained only in a very narrow window around breakdown. In order to do this, those authors first computed the average over disorder samples of the number of fuses $\langle N_{\text{break}} \rangle$ blown before catastrophic failure and, for every realization, collected statistics from events after almost $\langle N_{\text{break}} \rangle$ fuses have blown. A drawback of that procedure is that, since the time required to reach total failure largely varies among different disorder samples, one is mixing realizations that are very close to complete failure with others that are, say, half way into it, which

obey a different statistics. Our procedure to obtain the statistics differs significantly from that used in references [Pradhan et al. 2005; 2006] and has the advantage that it is not affected by this undesired effect. Moreover, in contrast to [Pradhan et al. 2005; 2006], we want to compare here the distribution of released energy until breakdown with that obtained when the system is at the very beginning of its evolution and how it changes as we approach failure.

For each disorder realization we let the system evolve up to total breakdown, which gives the corresponding T_{break} for that particular disorder realization. We then compare the collected statistics with that observed for that particular disorder realization up to two intermediate times, $\tau = T_{\text{break}}/8$ and $T_{\text{break}}/2$, that is, with the probability density when only the first one eighth and half of the failure avalanches are counted, respectively. In this way we collect statistics from realizations at the same evolution stage.

For each observation time, the probability density $\mathcal{P}_\tau(E, L)$ decays as $\sim E^{-1/2}$ until the crossover energy $E_\times(\tau, L)$. In figure 3.7 we plot the behavior of the distribution for the macroscopic energy, equation 3.5, for different system sizes and different observation times, rescaled according to equation 3.12.

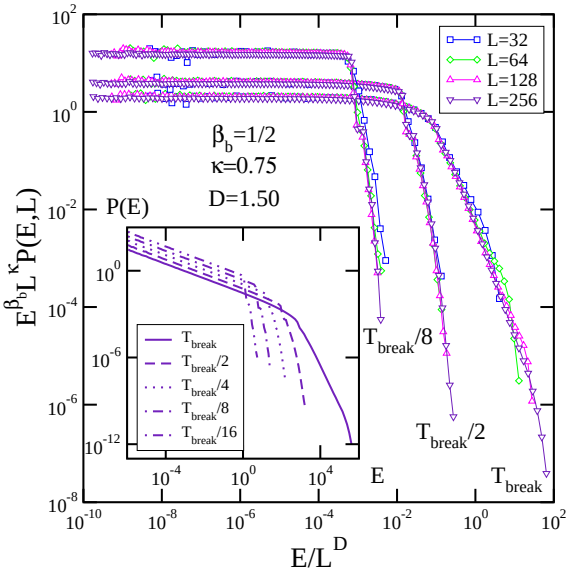

Figure 3.7: Macroscopic energy distribution for different final observation times. The inset shows the slope change at breakdown for more intermediate observation times for $L = 256$.

It can be observed that, while the crossover shifts to larger energy values as we approach complete breakdown, the scaling exponent in the second region is conserved as we increase the observation times. However, an abrupt change of exponent is observed only at the breakdown time T_{break}. This effect is perhaps better visualized in the inset of figure 3.7 where we plot the unscaled distribution data for the largest system $L = 256$ and different observation times. Despite we used a different measure of the dissipated energy and a different way to collect events these results are in agreement with the crossover picture between the two limiting behaviors reported in references [Pradhan et al. 2005; 2006]. This indicates that non-stationary effects of the dissipated energy temporal signal may actually be useful to characterize damage in stressed materials.

3.2.3 Finite driving rate

The lack of time scale separation in real experiments has been suggested as a possible reason for the discrepancy with the typical exponents found in numerical simulations of quasistatic models and real experiments [Alava et al. 2006]. In order to investigate this point we have studied the RFM under finite driving rates, so that the model evolution is no longer quasistatic. We have analyzed both stress and strain loading conditions and our results were not affected by the loading mode we used.

Strain is applied on the system by imposing a small potential drop between the bus bars in such a way that all the fuses are initially below threshold. The voltage is then increased at a fixed rate dV/V letting all the fuses over threshold burn, instead of the slow driving setup studied above. As usual, an avalanche is defined as all the fuses burnt between two consecutive voltage increments. In this setup, we can still observe an effective time scale separation at the early stages of the evolution, while potential increments are small. Figure 3.8 summarizes our numerical results for the time evolution of the microscopic dissipated energy, equation 3.6, at different strain rates in diamond lattices of linear size $L = 128$.

We observe that a power-law trend $E \sim t^{\alpha}$ is satisfied with a larger exponent α as the strain rate increases. If the strain rate is large enough (about $dV/V = 0.01\%$) the evolution is no longer described by a power-law, but it becomes exponential in time. The same behavior is also observed if either the macroscopic or global energy are used instead.

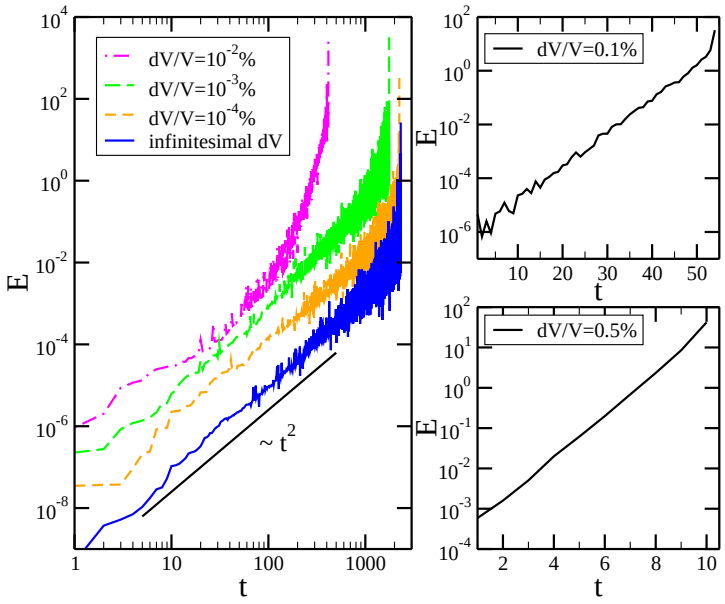

Figure 3.8: Temporal evolution of microscopic energy in an $L = 128$ diamond lattice for several finite driving rates. On the left panel, it can be observed how, as the driving is increased, the energy starts to deviate from t^2 growth. On the right panels one can see that, for large enough driving, the energy grows exponentially in time. Note the linear-log scale in the latter.

According to our simple calculation in equation 3.10, we expect that, in the limit of exponential growth, *i.e.*, $\alpha \gg 1$, the PDF of the dissipated energy becomes $\mathcal{P}_\tau(E) \sim E^{-1}$ for $E \ll E_\times$. We observe that the crossover energy $E_\times$ diverges as the strain rate is increased. In figure 3.8 one can clearly see that when we increase the strain rate the energy fluctuations become much smaller. In fact, fluctuations are negligible for the whole temporal (energy) range for large enough driving rates, when the exponential growth sets in (see figure 3.8). This means that the fall-off tail of the distribution corresponding to energies $E \gg E_\times$ is completely washed out in the case of large enough strain rates. Therefore, for large driving rates, if we let the system evolve up to complete breakdown, $\tau = T_{\text{break}}$, as well as for any other intermediate times, we expect the dissipated energy probability to be

$$\mathcal{P}(E) \sim E^{-1} f_{\text{cutoff}}\left(E/E_\times\right), \tag{3.14}$$

where the cut-off function is $f_{\text{cutoff}}(u) \sim$ const. for $u \ll 1$ and exponentially decreasing $f_{\text{cutoff}}(u) \to 0$ for $u \gg 1$. $E_\times \sim L^D$ is the maximum avalanche size possible for a finite-size system with fractal avalanche dimension D.

In Figure 3.9 we show the PDF of the macroscopic dissipated energy under a strain loading rate $dV/V = 0.1\%$ measured for all events up to total failure in the diamond lattice for different system sizes. Our numerical results are in excellent agreement with the prediction for finite loading rates in equation 3.14. The probability distribution for the microscopic energy also scales as E^{-1} for the whole range of energies in the case of finite-driving (not shown), but in this case the crossover energy shows no dependence with system size, in agreement with our above discussed results $D \approx 0$.

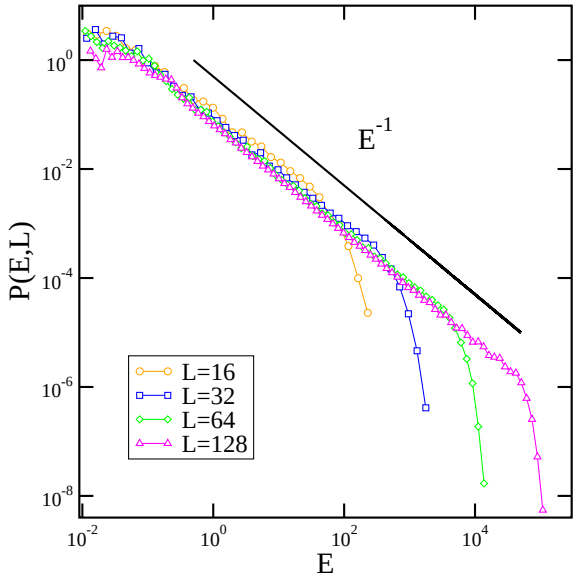

Figure 3.9: Macroscopic energy distribution for $L = 16, 32, 64$ and 128 diamond lattices under finite strain increments $dV/V = 10^{-1}\%$. A single power-law regime with the predicted exponent $\beta = 1$ is observed over the whole range of energies up to a finite-size cutoff.

The lack of time scale separation leads to a significant change in the distribution of the dissipated energy in the fuse model, as it should be expected. From a physical point of view there are strong differences in the system dynamics in the case of infinitesimal driving as compared with finite driving. If the system is driven at finite rates, relaxation to one of the infinitely many metastable configurations is not reached before a new perturbation acts on

the system. This gives rise to a highly nonlinear superposition of cascades of released energy instead of individual well-defined avalanche events. A finite driving rate generically leads to a growth of the dissipated energy at a much faster rate than the usual quasistatic dynamics, possibly exponential for any finite driving rate in large enough systems. In turn, this fast growth takes the crossover energy $E_\times$ to exponentially large values. The result is that the range of energies in which the PDF of the dissipated energy is described by equation 3.14 becomes very large, actually covering the whole range of energies.

3.3 Discussion

We have studied the dissipated energy in the RFM in order to compare with the AE statistics observed in real experiments in loaded materials. Different ways to define the released energy have been discussed, including a microscopic quantity that takes into account just the energy losses at each broken bond during an avalanche. Our results indicate that, for quasistatic dynamics, the dissipated energy statistics exhibits two very different regions depending on the energy scale one is looking at. These two scaling regions are separated by a typical energy $E_\times \sim L^{\alpha\, z-\sigma}$ and obey finite-size critical behavior. The low-energy region, for $E < E_\times$, is well described by a power-law decay $\mathcal{P}(E) \sim E^{-1/2}$, which is robust and independent of lattice geometry. We gave a simple scaling argument showing that this robustness is linked to the generic t^2 growth law of the dissipated energy; a feature shared by all the energy estimators we studied on any system size and lattice type and that it is directly linked to the quasistatic nature of the model. The statistics above the typical energy $E > E_\times$ crosses over to $\mathcal{P}(E) \sim E^{-2.75}$ and ranges several decades in energy.

Apart from scaling factors, the three energy definitions used here were expected to show similar statistics. However, while the behavior of macroscopic and global energies can be captured by the same scaling exponents and the high-energy region exponent is well defined, this is not the case for the microscopic energy that, although it obeys the same scaling form, shows no system size dependence and a different size-dependent exponent for the high energy region is obtained. Regarding the microscopic energy we introduced here, not only the numerical value of the exponent depends on the lattice size and fails to exhibit finite-size scaling, but also the scaling region covers a very narrow energy range. This should be particularly relevant when comparing with real fracture experiments that have shown that dissipated energy participating in

AE is not released all across the sample, but, quite the opposite, localized at microfractures [Garcimartín et al. 1997, Guarino et al. 1998].

Finally, we also studied the fuse model at finite driving rates. It is an often expressed belief that relaxing the quasistatic condition might lead to β exponents that compare better with experiments. We showed that under finite driving the cut-off energy diverges exponentially, so that the scaling $\mathcal{P}(E) \sim E^{-1}$ dominates all the energy range at any given time for large enough driving rates, possibly for any finite driving rate in large enough systems. The conclusion is that relaxing the quasistatic condition cannot give account of experiments, where β typically ranges between 1.2 – 2.0 depending on the material. The evidence we have up to now about the RFM indicates that it might well be the case that other essential aspects to quantitatively account for AE energy exponents in real materials are missing in the admittedly oversimplified fuse model.

Chapter 4

Perfect Plasticity and Optimization

This chapter deals with the irreversible deformations that materials exhibit when subject to large loads. We will focus on the so-called perfect plasticity (PP) limit using a perfectly plastic version of the random fuse model (PPRFM) introduced in [Hansen et al. 1991]. This problem has long been believed to belong to the universality class of directed polymers (DP). In particular it has been identified with a minimum energy (ME) surface. We will begin with the presentation of the model, an introduction to the topic of DP and the algorithms used in this chapter, and finish with a description of our contributions to the field [Picallo et al. 2009] in section 4.2. We will argue that the relation between PP and ME should be revised. The yield surfaces are shown to be different from the so-called ME surfaces. As a result, the global yield stress is lower than that expected from naïve optimization and the difference persists as the sample size increases. At variance with ME surfaces, height-height fluctuations of yield surfaces will be shown to exhibit multi-scaling. A theoretical argument will be provided to explain how this behavior arises due to the very different nature of the optimization problem in both cases.

4.1 Introduction

As we introduced in Chapter 2, perfect plasticity is a regime that can be characterized by an increase of the strain without any further increase of the

stress in the material, producing a stress-strain curve similar to figure 2.3. This is not just an idealized situation since this extreme behavior is found in experiments both in crystals [Champion et al. 2003] and amorphous materials [Gu et al. 2008, Schroers and Johnson 2004, Wang et al. 2007] as it can be observed in figure 4.1.

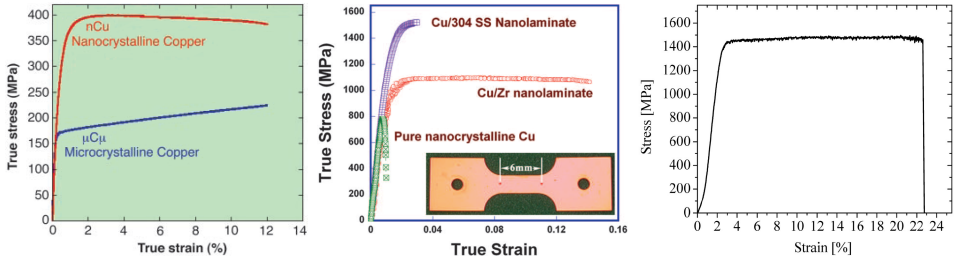

Figure 4.1: From left to right: Near-perfect elastoplasticity in tensile tests performed on pure bulk copper cylindrical specimens with nanometer grain size [Champion et al. 2003]. Tensile true stress–strain curves of Cu/Zr nanocrystalline–amorphous nanolaminates in comparison with those of Cu/304 stainless steel crystalline multilayer with an individual layer thickness of 25 nm and pure nanocrystalline Cu with an average grain size of $\approx$ 30nm [Wang et al. 2007]. Stress-strain curve of of a 3mm$\times$3mm$\times$6mm bar shaped sample of amorphous monolithic $Pt_{57.5}Cu_{14.7}Ni_{5.3}P_{22.5}$ under quasistatic compression [Schroers and Johnson 2004].

Macroscopically, plasticity seemed to correspond to an steady flow of the material under applied stress that could be described by the continuum theory of plasticity [Lubliner 2008]. However, early works pointed out the existence of fluctuations [Becker and Orowan 1932] and, thanks to recent experiments of AE in ice and intense subsequent research activity in this direction [Dimiduk et al. 2006, Miguel et al. 2001, Richeton et al. 2006, Schwerdtfeger et al. 2007, Wang et al. 2009, Weiss et al. 2007, Zaiser et al. 2008], we now know that at the microscale the dynamics in plastic materials is in fact governed by intermittent spatiotemporal avalanches of activity through the material. This will be discussed in detail in Chapter 5.

Just as the RFM emerged as a simple stochastic model of BF, able to capture some of the main ingredients of the problem and well suited for the exploration of the possible critical nature of the phenomenon, early attempts to develop a statistical mechanics treatment of plasticity lead to the development of the simplest scalar model for elastic-perfectly plastic behavior, the so called perfectly plastic random fuse model (PPRFM) [Hansen et al. 1991, Roux and Hansen 1992], in which every individual unit behaves elastic-perfectly plastic

as shown in the right panel of figure 2.6. However, that model lacks a very important ingredient in plasticity: avalanches. This is due to the fact that in the PPRFM there is no current (stress) enhancement after a yield event and thus stress is not redistributed, in contrast with the brittle RFM and other models with avalanches [Alava et al. 2006]. Hence, the PPRFM as it stands has a clear drawback, intermittency cannot be studied since the coarse-graining is done well above the microscopic plasticity limit where we can get rid of the jumps that are now known to occur at smaller scales.

The PPRFM was proposed as the electrical analog of an elastic-perfectly plastic amorphous medium, the plastic counterpart of the brittle RFM. Both brittle and perfectly plastic RFMs had since long been identified to belong to the directed polymer universality class [Roux and Hansen 1992]. However, the brittle RFM was numerically shown to behave far from what is expected for DP [Zapperi et al. 2005b]. In this chapter, the relationship of the RFM plastic version to DP will also be revised.

4.1.1 The elastic-perfectly plastic Random Fuse Model

To mimic the mechanical plastic response, each fuse ij in the PPRFM behaves ohmic up to its threshold current and, from then on, the local current remains constant and equal to the yield current,

$$i_{ij} = \begin{cases} kv_{ij}, & \text{for } v_{ij} < v_{ij}^{th} \\ \pm i_{ij}^{th}, & \text{for } v_{ij} \geq v_{ij}^{th}. \end{cases} \tag{4.1}$$

despite the local voltage keeps increasing due to the external voltage increase. This can be done using the *tangent algorithm* introduced in [Roux and Hansen 1992] that can be derived as follows.

Let us consider a perfectly plastic lattice and a brittle one (the tangent lattice). Let us call $\mathbf{v}$ the the local voltage solution we are seeking in the perfectly plastic lattice while $\mathbf{u}$ is the solution in the brittle lattice. As usual, we will call $\mathbf{K}$ and $\mathbf{b}$ the stiffness matrix and the source vector, respectively, and V_i the imposed external voltage ($V_0 = 1$) corresponding to the source vector $\mathbf{b}_i = V_i \mathbf{b}_0$. When the lattice is still intact we have

$$\mathbf{K}_0 \mathbf{u}_0 = \mathbf{b}_0, \tag{4.2}$$

and $\mathbf{u}_0 = \mathbf{v}_0$ since in the plastic lattice there is no plastic damage accumulated yet and, hence, both brittle and plastic lattices are still identical. For the same

reason, the system is still linear and we can increase the voltage of the weakest fuse up to exactly its threshold by just increasing the external voltage,

$$\mathbf{K}_0\mathbf{u}_{th} = V_1\mathbf{b}, \tag{4.3}$$

and therefore,

$$V_1 = V_0 \min_{ij}\left(\frac{u_{ij}^{th}}{u_{ij}^{0}}\right). \tag{4.4}$$

Once V_1 is known, we can determine $\mathbf{v}_1 = \mathbf{u}_{th} = V_1\mathbf{u}_0$. Right at threshold in the plastic lattice, we will have

$$\mathbf{K}_0\mathbf{v}_1 = V_1\mathbf{b}, \tag{4.5}$$

that can be equivalently written as

$$\mathbf{K}_1\mathbf{v}_1 = V_1\mathbf{b} + \mathbf{i}_{th}, \tag{4.6}$$

where $\mathbf{K}_1$ corresponds to a lattice with the plastic fuse missing and its threshold current included in $\mathbf{i}_{th}$. In order to bring the next fuse to threshold by increasing the external voltage, we should take into account that in equation 4.6 only the elastic part will be affected by the voltage increase, *i.e.*,

$$\mathbf{K}_1\mathbf{v}_{th} = V_2\mathbf{b} + \mathbf{i}_{th}. \tag{4.7}$$

From equation 4.6 we have $\mathbf{v}_1 = V_1\mathbf{K}_1^{-1}\mathbf{b} + \mathbf{K}_1^{-1}\mathbf{i}_{th}$ and from (4.7) we obtain $\mathbf{v}_{th} = V_2\mathbf{K}_1^{-1}\mathbf{b} + \mathbf{K}_1^{-1}\mathbf{i}_{th}$. With these two expressions we arrive to $\mathbf{v}_{th} - \mathbf{v}_1 = (V_2 - V_1)\mathbf{u}_1$ and hence we can obtain V_2 with

$$V_2 = V_1 + \min_{ij}\left(\frac{v_{ij}^{th} - v_{ij}^{1}}{u_{ij}^{1}}\right). \tag{4.8}$$

Once we know V_2 we can obtain the voltage vector $\mathbf{v}_2$ as

$$\mathbf{v}_2 = \mathbf{v}_1 + (V_2 - V_1)\mathbf{u}_1. \tag{4.9}$$

If we repeat this scheme till the tangent lattice $\mathbf{u}$ gets disconnected, *i.e.*, a continuous path of insulator fuses traverses the network, in the plastic lattice there will be a continuous path of fuses at threshold. Since there is a continuous path of fuses at its yield point, any increment of the external voltage will have no effect on the currents and thus we have found the PP yield surface of the system which is univocally determined for each disorder realization.

Hence, in summary, the simulation of the plastic process consists of yield iterations: at each update, the Kirchhoff equations are solved to determine the local currents flowing through the lattice. We then calculate the external voltage needed in order to make the most unstable fuse yield. After each yield event, the new currents are computed with the tangent algorithm and the process is iterated. After a large number of iterations, a yield surface is eventually formed across the sample.

4.1.2 Polymers in random media

The problem of finding the yield surface in a disordered material can be regarded in a more general context as connected with the problem of a directed polymer or manifold in a random medium. The study of directed polymers in random media (DPRM) has attracted a lot of attention during the last twenty-five years and a great number of interesting analytical and numerical results exist [Halpin-Healy and Zhang 1995]. This term comes originally from the studies of polymers stretched in a gel matrix and it is applied in a broad sense to any linear elastic object in a disordered environment like domain walls in ferromagnets [Huse and Henley 1985] or flux lines in superconductors [Nattermann and Lipowsky 1988, Nelson 1988].

A discrete coarse-grained description of such object can be formulated on a lattice in which each bond i has been assigned a random energy e_i picked from a certain probability distribution. A polymer grows along the t direction as it is shown in figure 4.2. Each step has an energetic cost equal to the random energy of the lattice bond and this produces a path $\mathcal{P}$ whose energy is given by the sum of the energies of the steps taken along the trajectory,

$$E_{\mathcal{P}} = \sum_{i \in \mathcal{P}} e_i, \tag{4.10}$$

and the partition function of the system at temperature T is then given by

$$Z(\mathbf{x}, t) = \sum_{\{\mathcal{P}\}} \exp\left(-\frac{E_{\mathcal{P}}}{k_B T}\right), \tag{4.11}$$

where $\{\mathcal{P}\}$ is the ensemble of all the possible univaluated paths starting at the origin $(0, 0)$ and ending at $(\mathbf{x}, t)$.

For a given disordered lattice not all of the paths are equally likely, its probability being proportional to the Boltzmann factor $\exp(-E_{\mathcal{P}}/k_B T)$, where $E_{\mathcal{P}}$ is the energy of the path. For a given temperature T, more energetic configurations are exponentially less probable.

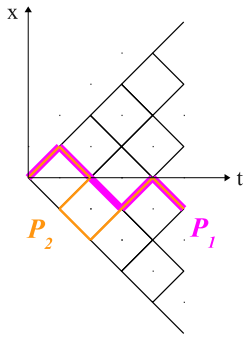

Figure 4.2: A typical configuration of a polymer growing in a discrete lattice from a fixed origin with (orange) and without (magenta) overhangs. The strictly directed polymers develop no overhangs since backward steps are not allowed.

The transverse growth is limited by the fact that each forward step implies only one transverse step. However, the impurities (random energy distribution) present in the medium induce the polymer to wander as much as possible in the search for energetically advantageous bonds. If there were no disorder, all paths would be equally probable and hence, in average, the final **x** coordinate would be zero with gaussian fluctuations as in the well-known random walk problem. Since we are mostly interested in the effect of the medium, there are two magnitudes useful to describe the configurations of the polymer: the wandering $\Delta x \equiv \langle (x - \langle x \rangle)^2 \rangle^{1/2}$ of the paths and the fluctuations of their free energy $\Delta E \equiv \langle (E - \langle E \rangle)^2 \rangle^{1/2}$. Both quantities exhibit power law scaling with exponents that characterize the universality class of DP:

$$\Delta x \sim t^{\zeta_{\rm DP}}, \quad \zeta_{\rm DP} = 2/3 \tag{4.12}$$

$$\Delta E \sim t^{\theta_{\rm DP}}, \quad \theta_{\rm DP} = 1/3. \tag{4.13}$$

These exponents were calculated numerically for 1+1 dimensions via transfer matrix studies [Derrida and Vannimenus 1983] at zero temperature in the context of the random bond Ising model [Huse and Henley 1985] and later for finite temperature in [Kardar 1985]. They were shown to be temperature-independent and exact values that can be calculated analytically with dynamic renormalization group techniques [Forster et al. 1977, Huse et al. 1985] and satisfy the relation $\theta_{\rm DP} = 2\zeta_{\rm DP} - 1$ [Huse and Henley 1985]. Several other results regarding the full probability distributions have been obtained [Halpin-Healy and Zhang 1995]. For our purpose here, it is of particular interest the

free energy distribution whose finite size correction is known to obey the law:

$$\frac{\langle E \rangle}{t} = E_\infty + At^{-2/3}, \tag{4.14}$$

with $A > 0$ and hence the free energy approaches its thermodynamic limit from above [Krug et al. 1992].

The DP problem can also be formulated in the continuum. In this case, the partition function 4.11 for a path from the origin to $(\mathbf{x}, t)$ takes the form

$$Z(\mathbf{x}, t) = \int_{(0,0)}^{(\mathbf{x},t)} \mathcal{D}\mathbf{x} \exp\left(- \int_0^t ds \left[\frac{1}{4\Gamma} \left(\frac{d\mathbf{x}(s)}{ds} \right)^2 - \mathcal{V}(\mathbf{x}, s) \right] \right), \tag{4.15}$$

or in differential form

$$\dot{Z}(\mathbf{x}, t) = \left(\Gamma \nabla^2 + \mathcal{V} \right) Z(\mathbf{x}, t), \tag{4.16}$$

where Γ is the inverse line tension and $\mathcal{V}$ describes the disorder in the medium. An interesting point is that under a simple Hopf transformation the latter equation can be mapped to the KPZ equation [Kardar et al. 1986] for kinetic roughening phenomena where the free energy of the polymer plays the role of the height of the interface with $\zeta_{\mathrm{DP}} = 1/z_{\mathrm{KPZ}}$ and $\theta_{\mathrm{DP}} = \beta_{\mathrm{KPZ}}$ [Barabási and Stanley 1995]. This equivalence thus also gives us the exact values of the DP exponents in 1+1 dimensions since the exponents $z_{\mathrm{KPZ}} = 3/2$ and $\beta_{\mathrm{KPZ}} = 1/3$ are exact for KPZ in 1+1 dimensions [Kardar et al. 1986]. Also the scaling relation $\theta_{\mathrm{DP}} = 2\zeta_{\mathrm{DP}} - 1$ corresponds to the Galilean invariance $\beta_{\mathrm{KPZ}} = 2/z_{\mathrm{KPZ}} - 1$ in KPZ, valid in any dimension.

As the temperature decreases, the configurations with lower energies will dominate in the partition function 4.11. At zero temperature only the lowest energy path survives. This means that at $T = 0$, the DPRM problem is just a global optimization problem in which, for a given quenched energy landscape, the path of overall ME is searched. The same exponents as in the finite temperature case hold ($\zeta_{\mathrm{ME}} = 2/3, \theta_{\mathrm{ME}} = 1/3$). The problem of finding the zero temperature solution is also called the *optimal path* problem and has been also extensively studied [Buldyrev et al. 2006, Cieplak et al. 1994, Hansen and Kertész 2004, Porto et al. 1997; 1999, Schwartz et al. 1998]. Results with different configurations and searching techniques have shown that optimal paths in 1+1 and 2+1 dimensions in the presence of weak disorder [Cieplak et al. 1994, Hansen and Kertész 2004] exhibit the same scaling properties with and without overhangs, with the same values of the scaling exponents [Schwartz et al. 1998]. This means that in this problem overhangs are irrelevant at long length scales since they do not grow with the system volume but have a characteristic size.

4.1.3 Finding the minimum energy surface

Although the transfer matrix methods are well-suited for directed configurations, the study of the ME surface in certain contexts [Alava and Duxbury 1996, Middleton 1995] posed new questions like the influence of the overhangs in the surface or the determination of the optimal paths in a lattice with no origin restrictions. Algorithms from graph theory resulted computationally more efficient than transfer matrix ones and very easy to implement. It was first noticed in [Ogielski 1986] and later in [Middleton 1995] that the search of the $T = 0$ ground state in the context of the random field and random bond Ising model could be reformulated as a problem of finding the minimum cut in a graph and solved thanks to the so called max-flow min-cut algorithms [Cormen et al. 2001].

Consider a network composed of a set of nodes and weighted links between them. The links can be viewed as pipes with a certain capacity (*i.e.*, the flow the pipe can carry) given by the weight of the link. One of the nodes is the source from which flow is injected in the network and another one is the sink of the system to which the flow must be pumped. The question is, what is the maximum flow the network can carry? And consequently, what path from source to sink should one take to achieve this optimum flow? The max-flow min-cut theorem states that in any network, the maximum flow equals the minimum capacity of a cut. A cut consists of a set of links such that if they are removed, the source and sink are disconnected and there is no path from the source to the sink as shown in figure 4.3. Hence, to obtain either the minimum cut of a network we can obtain the maximum flow or the other way round. The only restrictions to the problem are that pipes cannot carry negative flows or flows above its capacity and the conservation of mass must be fulfilled, *i.e.*, the flow into a vertex must be equal to the flow out of the vertex except for the source and sink nodes.

To find the maximum flow we will use the Ford-Fulkerson method that involves finding *augmenting* paths, that is, paths that allow us to increase the flow in the network. The flow that can be pumped through this path is given by the minimum of the capacities of the bonds along the path. Subtracting this flow to the capacities of the path we find the residual network. We continue looking for new augmenting paths in the subsequent residual networks until this task becomes impossible. When no more paths can be found, we know that we have obtained the maximum flow. The minimum cut is then formed by the bonds in the last residual network whose starting node can be reached from the source but whose ending node cannot.

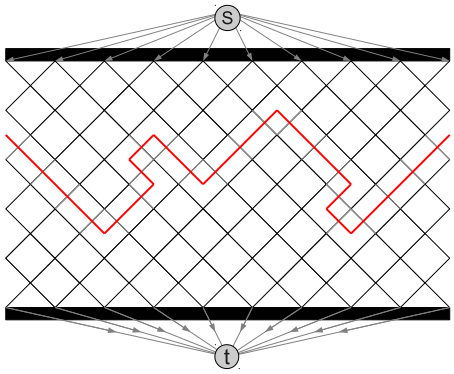

Figure 4.3: Source and sink nodes and an example of a cut in the network and the resulting interface.

The Ford-Fulkerson algorithm does not indicate how the paths must be found. The particular case of the Ford-Fulkerson algorithm in which the paths are shortest paths selected through a breadth-first search strategy (with equal weights in the bonds) [Cormen et al. 2001] is called Edmonds-Karp algorithm. In short this is a search algorithm that beginning at the source node, it first explores the neighboring nodes and for those nearest nodes, their unexplored neighbors and so on until it finds the searched node. The Edmonds-Karp variant has the advantage that its computational cost is $\mathcal{O}(NE^2)$, (N=nodes, E=edges) independent of the maximum flow of the network, and the termination is guaranteed. Although here we will focus in an Edmonds-Karp algorithm that will be employed later in this Thesis [Middleton 1995], there exist faster approaches like the push-relabel algorithms [Cormen et al. 2001] that run in $\mathcal{O}(N^3)$ (N =number of nodes). However, note that for sparse graphs like ours, the Edmonds-Karp algorithm can be even faster than the push-relabel techniques.

In our case, the ME surface can be seen as the minimum-cut of the lattice taking the energy of the bonds as the capacities of pipes. Once we obtain the maximum flow, we are sure that we have obtained the value of the ME for a given disorder realization. Finding the links belonging to the minimum cut we will hence find the ME surface. Two imaginary nodes must be added to the lattice to act as source and sink nodes (see figure 4.3) that are linked to the lattice through high capacity links so we make sure that they are not going to be included in the search. Both directed and undirected ME surfaces can be found with this implementation. A directed ME surface is found if the links between the nodes are set unidirectional and, in contrast, overhangs are

allowed if flow can be pumped backwards taking the bonds as bidirectional pipes. ME surfaces with fixed origin(end) can be obtained by simply imposing high capacities in the bonds belonging to the column corresponding to the origin(end) except for the selected node [Middleton 1995].

4.1.4 Analogies between yield and minimum energy surfaces

In our problem, the energy landscape is given by the random yield thresholds in the lattice. The ME surface in this context is the surface whose sum of yield thresholds is minimum. And hence, we will call *energy* to the sum of yield thresholds of any path in the network.

It was generally believed that strain localization in the PP limit could be related to the problem of finding the ME surface in a disordered medium [Hansen et al. 1991, Roux and Hansen 1992]. The conjectured equivalence between PP and ME comes from the observation that, at the yield point, it is not possible to find an elastic path along which the stress could increase spanning the sample from end to end [Hansen et al. 1991, Roux and Hansen 1992] since at the yield point there is a continuous band of bonds across the network in which all the bonds have reached their threshold and hence the stress cannot be further increased.

In a disordered medium, the local yield stress σ_i of a given cross-section is in general a quenched random quantity. Therefore, according to references [Hansen et al. 1991, Roux and Hansen 1992], the global yield stress σ_c could be obtained by finding the surface $\mathcal{S}$ where the sum of the local yield stresses (the energy) is minimized, *i.e.*, $\sigma_c = \min_{\mathcal{S}}[\sum_{i\in\mathcal{S}} \sigma_i]$. When this value of the stress is reached, the system would be divided into two disconnected elastic parts and would thus behave as perfectly plastic.

Following [Hansen et al. 1991, Roux and Hansen 1992], this maximal stress must be equal to the sum of the threshold stresses of each bond belonging to the path, as each threshold is equal to the maximum current the bond can carry. Hence, the band that is first to appear is the one where this sum is minimum and the problem is identical to the random directed polymer problem with the exception that there is no a priori directness imposed on the minimum current path. However, flowing through the network would actually impose a directness on the paths.

Thus, all the scaling laws for ME surfaces should be obeyed but here the role of the energy in the surfaces is played by the stress and hence one would

expect the following scaling relationships to ve valid:

$$\begin{aligned} \Delta y &\sim L_x{}^{\zeta_{\rm DP}}, \quad \zeta_{\rm DP} = 2/3 \\ \Delta \sigma &\sim L_x{}^{\theta_{\rm DP}}, \quad \theta_{\rm DP} = 1/3 \\ \sigma_c &= \sigma_\infty + AL^{\theta_{\rm DP}-1}, \quad A > 0. \end{aligned} \tag{4.17}$$

A critical revision of the analogies presented above will be the goal of next section.

4.2 Results

In the left panel of figure 4.4 it can be observed that a lattice of PP individual fuses subject to an external voltage is able to produce macroscopic perfectly plastic behavior. On the right panel, different colors indicate the fuses that yield during the corresponding region of the stress-strain curve. At the beginning the fuses that reach its yield point are randomly spread throughout the network. As the voltage increases, more and more yielding areas form up to the appearance of a yield surface by nucleation, as can be observed in the temporal sequence.

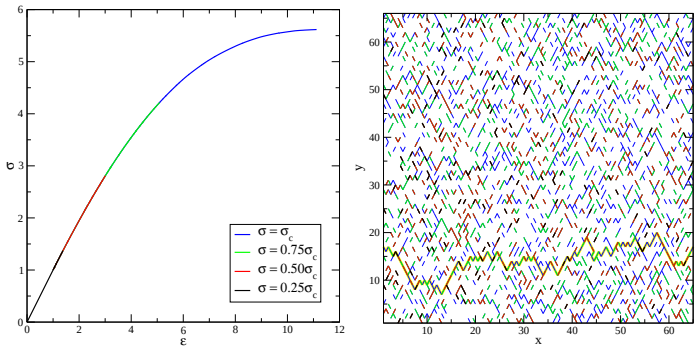

Figure 4.4: Left: Simulation of the PPRFM. Stress-strain curve in an $L = 64$ diamond lattice. Different colors indicate the maximum stress reached respect to the yield stress. Right: Plastically deforming sites up to the corresponding stresses in the left panel. The final yield surface is highlighted in yellow.

Trying to reveal the similarities between the PP and ME problems, we compared the resulting ME and PP yield surfaces for the very same disorder configuration. In figure 4.5 a typical realization with the PP surface obtained

with the PPRFM (section 4.1.1) and the ME surface with the Edmonds-Karp algorithm (section 4.1.3) is shown.

One can clearly see that the resulting interfaces may partially overlap but are clearly different. In particular, the PP surface presents very visible overhangs. As a consequence, the *energy* of the PP surface which corresponds to the sum of thresholds over the yield path is indeed higher than that for the ME surface which, although overhanging is allowed, takes a pretty directed path as it is expected for this type of disorder [Schwartz et al. 1998]. However, we find that the actual yield stress or the current through the PP surface is lower than its energy, and also lower than that for the ME surface. We will try to explain these facts in the next section.

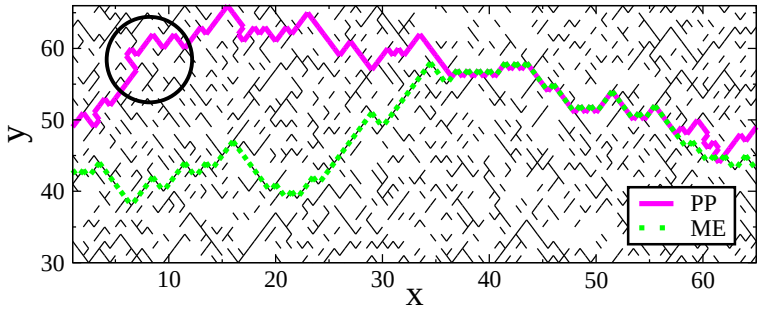

Figure 4.5: Typical ME and PP yield surfaces for the same disorder realization in a $L = 64$ diamond lattice. A region of the PP surface exhibiting overhangs is highlighted within the black circle.

4.2.1 A theoretical argument against the equivalence between perfect plasticity and minimum energy

The difference between PP and ME surfaces for the same disorder realization can be explained by the following theoretical argument. The equivalent yield stress for the ME problem in a system of lateral size L_y is given by

$$\sigma_{c,ME} = \sum_{i \in \mathcal{S}} i_i^{th} / L_y, \tag{4.18}$$

where i runs over all the bonds in the yield surface $\mathcal{S}$ that minimizes (4.18). In contrast, the PP surface $\mathcal{S}'$ would be the surface that requires a lowest external stress to appear and, therefore, the one that minimizes

$$\sigma_{c,PP} = \sum_{i \in \mathcal{S}'} (\mathbf{n}_i \cdot \mathbf{j}_i)\, i_i^{th} / L_y, \tag{4.19}$$

where $\mathbf{n}_i$ is the unit vector locally normal to the surface at i, and $\mathbf{j}_i = \mathbf{J}_i/|J_i|$ is the local current flow direction as corresponds to the definition of the current flowing through an arbitrary surface.

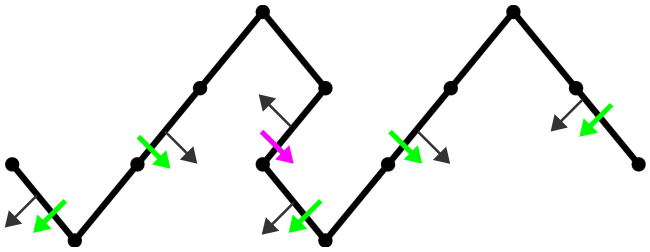

Figure 4.6: Grey arrows indicate the normal to the surface in each region. Thick arrows indicate how the current traverses the surface. In the overhang the current (magenta arrow) and the normal vector are opposed while in the rest of the surface both of them point in the same direction.

If the surface had no overhangs we would have $\mathbf{n}_i \cdot \mathbf{j}_i = 1$ for all i and the same surface $\mathcal{S} = \mathcal{S}'$ would minimize both equation 4.18 and equation 4.19. However, in the presence of overhangs, it could happen that locally $\mathbf{n}_i \cdot \mathbf{j}_i = -1$ so that the surfaces $\mathcal{S}$ and $\mathcal{S}'$ are no longer the same. This is illustrated in figure 4.6. Indeed, we find that

$$\sigma_{c,PP} < \sigma_{c,ME}, \tag{4.20}$$

although the sum of thresholds along the PP path is naturally higher than $\sigma_{c,ME}$. Therefore, the mapping between ME and yield stress exists only for fully directed surfaces ($\mathbf{n}_i \cdot \mathbf{j}_i = 1$ for all i), where the total yield stress can be calculated as the sum of local yield stresses. Physically, this means that PP and ME actually correspond to two different optimization problems. A PP path may find it very advantageous to develop overhangs in order to minimize equation 4.19 due to the negative contributions coming from the $\mathbf{n}_i \cdot \mathbf{j}_i < 0$ terms. On the contrary, for the ME surface one has to minimize equation 4.18 and overhangs generally increase the global energy and are thus normally avoided, unless disorder has a very broad distribution [Buldyrev et al. 2006]. The yield surface would in fact be the result of a ME problem in which, unlike in the simple ME, only bonds of the path in the direction of the flow increase the global energy by a quantity equal to the energy cost of the bond, while bonds passed by opposing to the flow (*i.e.*, overhangs), decrease the global energy of the path by a quantity equal to the energy cost of that bond

4.2.2 Energy and yield stress scaling

The difference between the ME and PP yield stresses can be observed in figure 4.7. Two different boundary conditions have been studied: the two ends of the path are either left free or pinned at mid-system $y(0) = y(L_x) = L_y/2$. These two situations correspond to finding either a global or a local minimal surface, respectively. Left panel shows the yield stress scaling with system size for fixed boundary conditions while right panel shows the free ends case. In both cases the existence of a finite size correction becomes apparent, as well as the fact that $\sigma_{c,PP}(L) < \sigma_{c,ME}(L)$ is always satisfied.

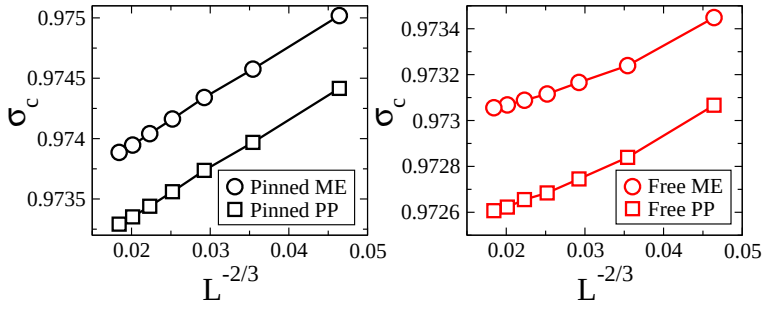

Figure 4.7: Scaling of critical stress with system size in ME and PP for both fixed and free ends

For fixed boundary conditions we find $\sigma_c = \sigma_\infty + AL^{-2/3}$ leading to $\theta = 1/3$, which is the expected result for the ME universality class and likewise so for the PP problem. It is interesting to note that the same scaling relation for σ_c was deduced for the growth of a slip line in a crystal with also a positive A constant but larger scaling exponent [Leoni and Zapperi 2009]. This kind of dependence of the yield strength with system size is also usually observed in microscopic to nanoscopic plasticity experiments [Lee et al. 2007, Uchic et al. 2004].

As can be observed in the previous figure, for free boundary conditions this scaling holds only for small system sizes. This can be understood as follows. As we saw in section 4.1.2, a ME surface in a system of length L_x develops height fluctuations of width $\sim L_x^{2/3}$. Thus in a system of height L_y there is room for $(L_y/L_x^{2/3}) \sim L^{1/3}$ independent valleys of energy as it is sketched in figure 4.8. Hence, letting the starting point free, for each disorder realization we are effectively averaging over $L^{1/3}$ fixed starting point independent surfaces and picking the minimum of them. This means that we are affecting

the finite size scaling mixing two different scales: the energy scaling related to the length of the ME surface and the extremal statistics related to the transverse optimization. This explains the fact that large system sizes deviates from the expected scaling (equation 4.14) since only for small system sizes $(L_y/L_x^{2/3}) \sim 1$ and thus the transverse scale does not enter the scaling.

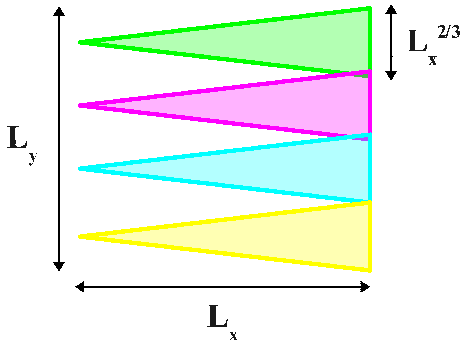

Figure 4.8: Independent energy valleys in a system of size (L_x, L_y).

We can also study the average yield strength difference $\langle \sigma_{c,ME} - \sigma_{c,PP} \rangle$. In figure 4.9 it is observed that it systematically increases with L for free boundary conditions or remains constant in the case of fixed boundary conditions but the difference never vanishes as we increase the system size indicating that the difference between the two problems is not a finite-size effect but will remain in the thermodynamic limit.

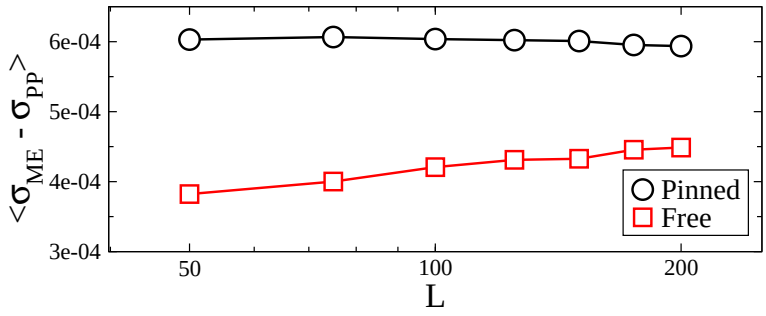

Figure 4.9: The difference between the critical stress for ME and PP grows slowly but systematically or remains approximately constant with system size for free or pinned ends, respectively.

4.2.3 Yield stress distribution

The scaling of the yield stress is reminiscent of size effects traditionally studied in brittle fracture problems where one expects extreme value statistics to apply [Alava et al. 2009, Weibull 1951]. Although size effects and stress fluctuations have been recorded in micro-plasticity [Lee et al. 2007, Uchic et al. 2004], it is not clear if they have the same origin as in fracture. In particular, it has been observed both in crystals [Uchic et al. 2004] and amorphous materials [Lee et al. 2007] that strong size effects appear when decreasing the sample sizes to micron scales and below. This manifests itself in way higher strengths than the observed values for bulk samples of the same materials. This size-dependence vanishes with sample diameters only tens of microns larger whose properties again resemble the bulk behavior. Although some experiments claim for size-independent properties at micron scales [Dubach et al. 2009, Schuster et al. 2008], the dependence of the strength on system size seems to be a fact. A good knowledge of the behavior of samples of such small sizes is obviously an important issue from a technological point of view.

We have explored the behavior of the yield stress distribution for the PP and ME models. Figure 4.10 shows the rescaled yield stress cumulative distributions for both ME and PP problems with free and pinned boundary conditions. The latter corresponds to the usual ME problem studied in the literature while the *free* case is closer to experimental reality.

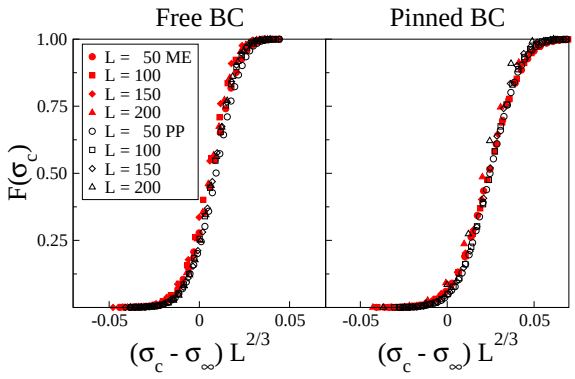

Figure 4.10: Cumulative distributions of yield stress for free and pinned boundary conditions for ME and PP. The distributions can all be collapsed with the same exponent, related to $\theta = 1/3$.

We see that for both boundary conditions the distributions for PP and ME collapse with the same exponent into a very similar scaling function. Since for the ME problem with pinned boundary conditions we know that asymptotically the scaling function should converge to the Tracy-Widom distribution [Monthus and Garel 2006], we can speculate that this is also true for PP. Weibull and other extremal distributions are not appropriate to fit the data.

4.2.4 Geometrical properties

We will now analyze the spatial properties of the yield surfaces. This study again shows that PP and ME surfaces are different objects with distinct scaling properties. Measuring only the height fluctuations $\langle \Delta y \rangle \sim t^{\zeta_{\mathrm{DP}}}$ both PP and ME surfaces yield values very close to $\zeta_{\mathrm{DP}} = 2/3$ and are hence indistinguishable. However, one can test the *multi-affinity* of the surfaces by studying the qth order correlation functions,

$$C_q(\ell) = \langle \overline{|y(x+\ell) - y(x)|^q} \rangle \sim \ell^{\,q\,\zeta_q}. \tag{4.21}$$

If all the exponents result $\zeta_q = \zeta$ independent of the order q, it means that the surface is self-affine and it is completely characterized by one single roughness exponent ζ. In contrast, if different q give different ζ_q exponents, the surface is said to be multi-affine and the roughness exponent alone is not enough to characterize the surface since the roughness changes from one region of the surface to another. The calculation of the correlation functions 4.21 needs a univaluated height function. In order to eliminate the overhangs we carried out a *solid-on-solid* transformation in which for each site x we take the maximum value of the height $y(x)$.

In the case of ME surfaces, they are expected to exhibit simple self-affine scaling with the same roughness exponent $\zeta_q^{ME} = \zeta^{ME} = 2/3$ for all q. This is observed in figure 4.11 and is in agreement with previous studies showing that overhangs are irrelevant in ME surfaces below the strong disorder limit [Buldyrev et al. 2006, Schwartz et al. 1998].

In contrast, PP surfaces show strong deviations from simple self-affinity and the existence of multi-scaling becomes readily evident in figure 4.12 where at small length scales it is clearly observed that different order correlation functions scale with different exponents. Self-affinity is recovered above a certain length scale that increases with system size indicating that overhangs are indeed relevant in PP surfaces.

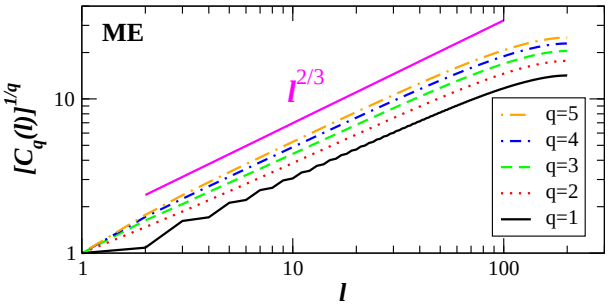

Figure 4.11: Height-height correlation function of order $q = 1$ to $q = 5$ for ME in a system of size $L = 200$.

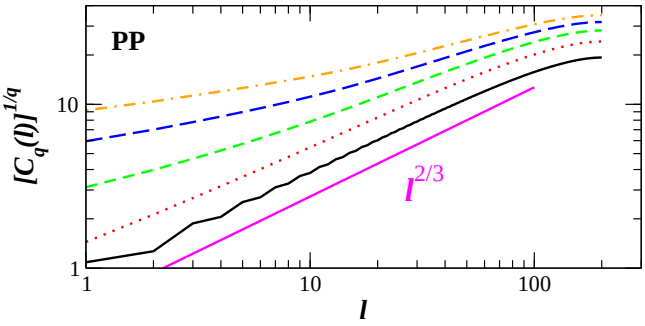

Figure 4.12: Height-height correlation function of order $q = 1$ to $q = 5$ for the PP problem in a system of size $L = 200$. Multi-scaling of the surface fluctuations is clearly observed.

To obtain further insight on the role of overhangs we can study the distribution of height differences at different length scales,

$$\mathcal{P}\left(|\Delta_\ell y|\right) \text{ with } \Delta_\ell y \equiv y\left(x+\ell\right) - y\left(x\right). \tag{4.22}$$

For a self-affine interface, this distribution is expected to scale as

$$\mathcal{P}\left(|\Delta_\ell y|\right) \sim \ell^{-\alpha} f\left(|\Delta_\ell y|/\ell^{-\alpha}\right). \tag{4.23}$$

In figure 4.13 it is shown that for ME surfaces $\mathcal{P}\left(|\Delta_8 y|\right)$ is narrow and independent of L, whereas for the PP surfaces the tail grows with L and approaches asymptotically a power-law shape, $\mathcal{P}\left(|\Delta_8 y|\right) \sim |\Delta_8 y|^{-2}$. However, as shown in the center and right panels of figure 4.13 for $\ell = L/4$ and $\ell = L/2$ respectively, if we study the height differences at intermediate length scales $\ell \ll L$,

both distributions get more and more similar up to the point they become almost indistinguishable at the macroscopic scale.

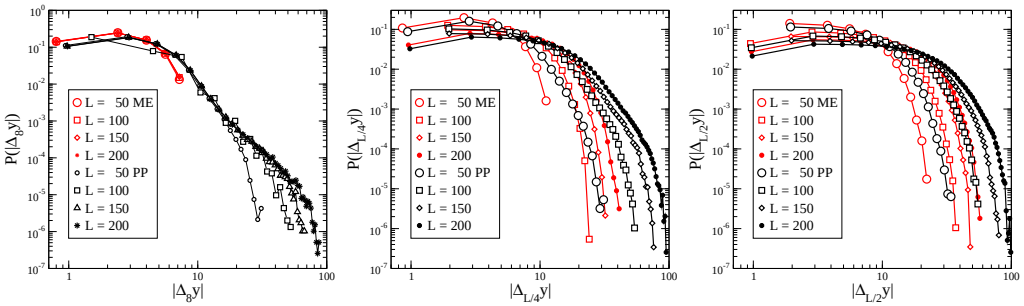

Figure 4.13: Distribution of height differences at distances, from left to right, $\ell = 8$, $\ell = L/4$, and $\ell = L/2$ in PP and ME for different system sizes. For PP the tail of the distribution grows with system size, while it remains constant for ME surfaces.

4.3 Discussion

We have studied the plastic yielding of disordered media using the perfectly plastic random fuse model. By numerical simulations and theoretical arguments we have shown that, in contrast with a generally accepted conjecture, PP and ME actually correspond to two different optimization problems in disordered media. This ends with the long-standing assumed equivalence between PP and DP problems. In the past, DP had been also claimed to be equivalent to BF [Hansen et al. 1991] and was recently refuted [Zapperi et al. 2005b]. The reason for the non-equivalence between ME and PP surfaces arises from the fact that an actual yield surface –with signed currents– is created in a yielding material at lower critical stress than the ME surface. This is intimately related to the peculiar properties of PP surfaces such as the existence of relevant overhangs, large height-height fluctuations, and lack of simple self-affinity. In addition, the yield stress displays a finite-size scaling form with corrections due to the boundary conditions.

The yield stress for PP is indeed smaller than the one observed for the equivalent ME problem, while the critical exponents of the surface and energy fluctuations appear to be the same. The yield surfaces have a roughness exponent of approximately $\zeta = 2/3$ and the yield stress fluctuations scale with an exponent close to $\theta = 1/3$, that coincide with those of the ME universality class. However, the specific surfaces are different in the two cases. Indeed, the

geometry of the surface in the PP problem shows the presence of overhangs and large steps that lead to multi-scaling, a dependence of the q-th order roughness exponent on the order of the correlation function. The presence of overhangs has a significant effect on the global yield stress. Contrary to what happens in the common ME problems, overhangs lower the global yield stress so that a trivial minimization of the sum of local yield stresses is not accomplished.

Despite the attractive simplicity of this scalar model for PP, we cannot forget that it has an unavoidable drawback since it lacks the intermittent behavior widely observed in experiments and hence the properties of burst avalanches cannot be studied in this context. It would then be interesting to study numerically more realistic albeit simple models of plasticity and for this purpose in the next chapter we will introduce a scalar model of fuses that, while preserving the simplicity of the RFM, is able to correctly capture the mesoscopic behavior of amorphous plastic solids.

Chapter 5

From Brittle to Ductile Fracture

In this chapter we will focus on plastic deformation in amorphous media. To this aim we introduce a model that tries to combine the simplicity of the scalar models based on fuse networks but at the same time incorporates the observed phenomenology arising at the microscale that has strong influence on the final behavior of materials. We will begin with a brief review of the experimental findings, then describe the different approaches to plasticity, and we will finish with the description of our ductile random fuse model (DRFM) in section 5.2 and our contribution [Picallo et al. 2010a;b] in section 5.3. The lattice model introduced here is able to describe damage and yielding in heterogeneous materials ranging from brittle to ductile ones. The model exhibits a smooth transition from brittleness to ductility, depending on how much plastic deformation is accumulated prior to fracture. Very ductile fracture surfaces, obtained when the system breaks once the strain is completely localized, are shown to correspond to ME surfaces. The similarity of the resulting fracture paths to the limits of brittle fracture or minimum energy surfaces is quantified. The dynamics of yielding exhibits avalanches with a power-law distribution in agreement with mean field calculations and experimental findings.

5.1 Introduction

5.1.1 Macro and micro-plasticity

In crystalline materials plasticity is explained by the motion of defects or dislocations in the crystalline lattice that act as carriers of slip in response to the applied stress [Zaiser 2006]. This implies that plasticity at the scale of dislocations has a discrete nature both in space and time which, at least at that scale, is in conflict with the paradigm of continuous flow. The hypothesis was that dislocation movements at the microscale could average out to give the appearance of a smooth and steady flow. This is in fact observed in experiments with bulk samples due to the incoherent superposition of deformation events from different parts of the specimen producing stress-strain curves that resemble figure 2.3. However, as one goes down to the micrometer scales the intermittent nature of the phenomenon is clearly revealed. Acoustic emission measurements performed in compression tests of millimeter ice single crystal samples showed that the dynamics is in fact intermittent and gives rise to power law distributed events [Miguel et al. 2001, Weiss and Grasso 1997] that suggested an interpretation in terms of critical phenomena. Hence, the smooth appearance of the ductile stress-strain curve in figure 2.3 hides in reality a much more complex behavior. The superposition of motions is not incoherent but produces scale-free bursts of activity with long-range correlations both in space and time that leads to the characteristic stress-strain curves in steps shown in left panel of figure 5.1 corresponding to direct measures of deformation events in metallic microcrystals [Dimiduk et al. 2006, Uchic et al. 2004]. The stress-strain curve is formed by small jumps and plateaus that cannot be accounted for within the framework of continuous theories and the whole process is governed by the intermittent avalanches of activity in the material.

In analogy with brittle fracture, general scaling laws like acoustic emission and strain avalanche distributions [Dimiduk et al. 2006, Schwerdtfeger et al. 2007, Uchic et al. 2004, Zaiser et al. 2008] are also observed in plastic deformation. Both indirect evidence by means of acoustic emission experiments [Miguel et al. 2001, Richeton et al. 2006], and direct micro-compression measurements [Dimiduk et al. 2006, Schwerdtfeger et al. 2007, Zaiser et al. 2008] have shown that the distribution of strain bursts sizes decays as a power-law with an exponent that lies within the range $\tau = 1.4 - 1.6$.

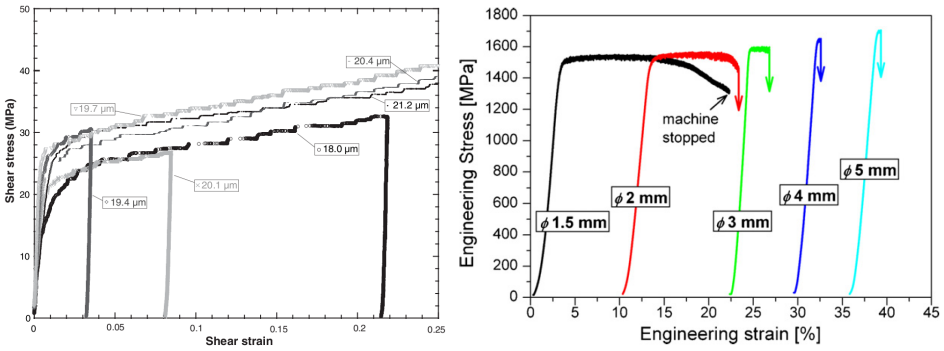

Figure 5.1: Experiments revealing the jerky nature of the plastic flow and the impact of sample size on the yield strength. Left: Shear stress versus shear strain curve in a 20 mm diameter sample of pure crystalline Ni [Dimiduk et al. 2006]. Right: Compressive engineering stress-strain curves of $Zr_{65}Cu_{17.5}Ni_{10}Al_{7.5}$ alloy specimens with different casting diameters [Han et al. 2009].

But here we are interested in amorphous materials that do not have an underlying ordered structure as crystals do. In the absence of internal structure or long range order, plasticity is believed to be due to irreversible atomic rearrangements. These rearrangements are highly localized in certain regions composed of a few atoms where shear transformations happen more likely and seem to be related to enhanced structural disorder regions [Christopher A. Schuh 2003]. These are called *shear transformation zones* (STZs) [Argon 1979, Falk and Langer 1998] and only recently have been observed in colloidal glasses [Schall et al. 2007] following the microscopic strain distribution. These regions were shown to be irreversible. Moreover, the existing zones induced the appearance of new zones in their vicinity as more strain is accumulated.

The fingerprint of the stress-strain curves of plastic deformation in amorphous materials is the serrated flow that can be observed in the right panel of figure 5.1. This has been hypothesized to be related to the formation of shear bands where strain localizes [Dubach et al. 2009, Schuh and Nieh 2003] and can then induce final failure [Li and Li 2005; 2007, Schall et al. 2007, Yao et al. 2008]. As happens in crystalline materials, amorphous plasticity is characterized by power law distributed avalanches with an exponent around $\tau = 1.4$ [Wang et al. 2009].

Metallic glasses (MG) are an example of amorphous alloys that offer good prospectives for technological purposes and are currently a fertile ground for research [Guo et al. 2007, Lee et al. 2007, Schuster et al. 2008, Shan et al. 2008].

In macroscopic samples, the strain is very inhomogeneous and localizes into a few shear bands leading to cracking and catastrophic failure (top panel in figure 5.2). As size is decreased to submicron samples, the flow becomes more homogeneous, more bands appear (bottom panel in figure 5.2), and ductility increases [Shan et al. 2008].

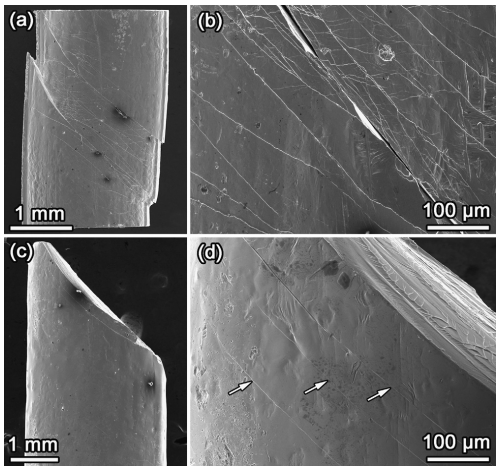

Figure 5.2: SEM images showing the side views of $Zr_{65}Cu_{17.5}Ni_{10}Al_{7.5}$ BMG samples –2mm (left) and 3 mm diameter (right)– after compression tests. In the 3mm case few shear bands are found and hence the behavior is quasi-brittle. Taken from [Han et al. 2009]

MGs usually show little ductility at room temperature and behave quasi-brittle but with the appropriate composition and treatment they can be tuned and MG ranging from brittle to very ductile and with very different hardening coefficients can be obtained [Schuh et al. 2007]. Hence, since amorphous materials form a motley group with very diverse behaviors, it is appealing to propose models that can account in a simple way for brittleness and ductility allowing to study both limits tuning a small set of parameters. This will be the goal of section 5.3.

5.1.2 Numerical and theoretical approaches

In crystalline systems the theoretical framework seems to be well established and yielding can be described as a non-equilibrium phase transition at the yield stress point. The onset of plasticity in this context seems to correspond to a transition from a jammed phase, in which dislocations are immobile, to

the phase of flow with sustained motion of dislocations [Laurson et al. 2010, Leoni and Zapperi 2009, Miguel et al. 2002, Zaiser and Moretti 2005]. The theoretically predicted value for the exponent of the avalanche distribution $\tau = 3/2$ agrees with numerical simulations [Zaiser and Moretti 2005] and is close to experimental observations.

In amorphous materials, modeling appears to be a more complex task since there is no underlying structure for defects. However, the similarities of behavior that appear in very different materials call for an explanation that does not require a detailed description of the material-dependent microscopic processes. In fact both crystalline and amorphous materials exhibit similar phenomena, which makes it appealing to find a description independent of the existence of a subyacent crystal lattice.

Thanks to molecular dynamics simulations with molecules interacting via Lennard-Jones potentials, the existence of STZs involving tens of molecules was proved [Falk and Langer 1998] and mean field theories based on the role of the localized events in the STZs were developed (see [Langer 2008] and references therein). STZs are created and annihilated during the irreversible deformations of a material and localization in the form of shear banding also appears. However, plastic events are not random but occur as correlated cascades of events [Maloney and Lemaître 2006], whose size seems to depend on the strain rate [Lemaître and Caroli 2009], indicating that mean-field theories based on independent events would not be an accurate description of the phenomenon. In [Bailey et al. 2007] an exponent close to $\tau = 3/2$ was measured for a 3D Mg-Cu system, in agreement with experiments in both amorphous and crystalline materials.

The development of an adequate numerical and theoretical framework of amorphous plasticity to understand deformation and failure mechanisms is a challenge since many applications of technological relevance can be envisaged and new materials could be developed under the guidelines provided by theoretical understanding. The drawback of atomic-level simulations for this purpose is that the system sizes and computing times available are very limited. Besides, bridging gap between the length scales of microscopic models and continuum theories is yet one of the most exciting problems in materials science. To go beyond the atomic scale in plasticity, efforts have been made to study plastic deformations at mesoscopic scales [Baret et al. 2002, Cowie et al. 1993, Lee et al. 1999, Miltenberger et al. 1993, Picard et al. 2004, Roux and Hansen 1992]. Very recently, a stick-slip model was successfully applied to reproduce experimental observations of intermittent behavior of metallic glasses [Sun et al. 2010]. In general, these models explicitly include

the long-range elastic interactions and disorder. If a local threshold is reached a rearrangement occurs that produces a plastic event. The local stress thus relaxes and the elastic redistribution of stresses in the medium can induce other local events, giving rise to a complex macroscopic spatiotemporal behavior with intermittency and bursts of correlated events. In the following section our goal is to introduce a mesoscopic model that, unlike the oversimplified model [Roux and Hansen 1992] used in the previous chapter, is able to account for the typical phenomena present in amorphous materials like serrated flow, shear banding, and spatiotemporal intermittency, while preserving the simplicity of the scalar RFM model.

5.2 A tunable ductile Random Fuse Model

In our DRFM, whenever a fuse ij reaches its threshold i_{ij}^{th}, a permanent deformation is imposed to the element and becomes elastic again as it is shown in figure 5.3. This defines a *healing cycle* of the individual element.

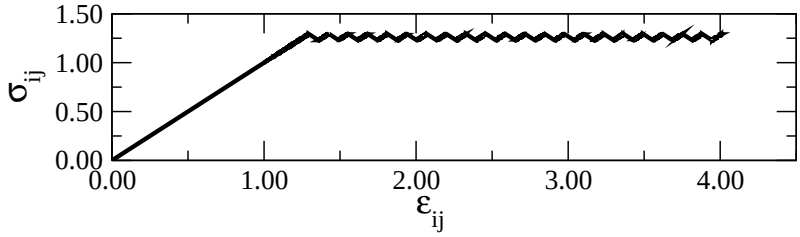

Figure 5.3: A typical stress-strain response curve for a single element of the DRFM in a diamond lattice of size $L = 75$ with disordered thresholds uniformly distributed in the interval $[0.5, 1.5]$ for $\beta = 0.1$.

In our electrical analogue this healing is done by adding a voltage source (*i.e.* an electric battery) in series with the fuse in the adequate polarization to generate an opposite current through it, so that elastic deformation (due to the ohmic behavior of the fuse) is relaxed below threshold while permanent deformation (the voltage fixed by the added voltage source) accumulates in the element. In figure 5.3, each of the current drops corresponds to a healing cycle during which the fuse reached its threshold, accumulated plastic deformation by the addition of a voltage source and became elastic again.

The addition of a voltage source between two nodes of the network modifies the voltage equations of the system in a very simple way. Let us consider a fuse with a battery in series like shown in the next figure.

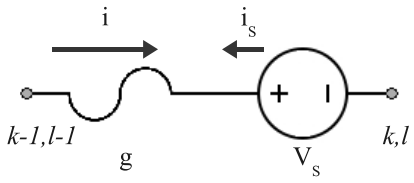

Figure 5.4: A fuse in series with a voltage source.

Then the KCLs of two nodes $(k-1, l-1)$ and (k, l) are modified from

$$\begin{aligned} 4kV_{k-1,l-1} - kV_{k-2,l-2} - kV_{k-2,l} - kV_{k,l-2} - kV_{k,l} &= 0 \\ 4kV_{k,l} - kV_{k-1,l-1} - kV_{k-1,l+1} - kV_{k+1,l-1} - kV_{k+1,l+1} &= 0, \end{aligned} \tag{5.1}$$

for a single fuse between them to

$$\begin{aligned} 4kV_{k-1,l-1} - kV_{k-2,l-2} - kV_{k-2,l} - kV_{k,l-2} - kV_{k,l} &= V_S \\ 4kV_{k,l} - kV_{k-1,l-1} - kV_{k-1,l+1} - kV_{k+1,l-1} - kV_{k+1,l+1} &= -V_S, \end{aligned} \tag{5.2}$$

for the fuse in series with the battery. In our model we choose the magnitude of the voltage source used to heal a fuse ij to be linearly related to its threshold current,

$$\Delta = \beta\, i_{ij}^{th}/k_{ij}, \tag{5.3}$$

where β is a control parameter that tunes how much deformation is allowed to be accumulated at each healing cycle and the local conductivity is fixed to $k_{ij} = 1$ without loss of generality. In the double limit $\mathcal{N}_{HC} \to \infty$ and $\beta \to 0$, one would obtain an elastic-perfectly plastic response.

At each step of the simulation both the fuse closest to threshold and the external voltage required to reach it can be exactly calculated. Therefore, in order to save computational time, the external voltage is increased exactly up to the point where the next fuse in the network reaches its threshold. To do this one just needs to take into account that only the elastic part of the network will be affected by an increase of the external voltage while the plastic part remains constant. The next fuse ij to burn will be the one that fulfills:

$$\min_{ij} \left(\frac{i_{ij}^{th}/k_{ij} - v_{ij}^{p} + \sum \Delta}{v_{ij}^{e}} \right), \tag{5.4}$$

where v_{ij}^{p} is the the plastic part of the voltage solution, *i.e.*, the corresponding to the permanent currents, v_{ij}^{e} is the elastic part corresponding to the ohmic behavior, and $\sum \Delta$ is the sum of all the voltage sources imposed along the history of the fuse at consideration.

We repeat the healing cycle a fixed number of times $\mathcal{N}_{HC}$ for each fuse going above threshold until it definitely breaks. The number of healing cycles $\mathcal{N}_{HC}$ that each individual element can go through before failure is fixed for all the fuses and parametrizes in a simple and convenient manner the yielding characteristics (ductility) of the material. At any given time in the simulation, different sites of the network have gone through a different number of healing cycles, reflecting the spatially varying distribution of strain in the system. A fuse is forced to burn (or break) after having gone through its fixed number of healing cycles $\mathcal{N}_{HC}$. The fuse then irreversibly becomes an insulator following the usual rules for the RFM (see section 2.3.1) and all the voltage sources that were imposed as plastic deformation are removed hence affecting the equations of the neighboring fuses. The current redistribution after the healing of a fuse can cause other fuses to also reach their thresholds. Therefore, avalanches of plastic events are observed similar to the strain bursts observed in experiments. When a continuous path of insulating bonds is formed, the system is disconnected and fails completely producing an observable macroscopic fracture.

5.3 Results

Depending on the material properties the DRFM is able to exhibit fracture in situations that range from brittle to ductile behavior. Figure 5.5 (left panel) shows the global stress-strain curves for $\beta = 0.1$ for different realizations and increasing mean value of the disorder distribution, as the number of healing cycles $\mathcal{N}_{HC}$ before breakdown is increased, allowing to accumulate more plastic strain in the material until fracture. For comparison, right panel shows a replot of stress-strain curves obtained in recent experiments [Gu et al. 2008] with amorphous steel alloys of Fe–Cr–Mo–P–C–B with different ductility produced by changing the metal-metalloid composition. This illustrates how the index $\mathcal{N}_{HC}$ in our model can parametrize in a simple manner the ductility of the experimental samples. The maximum number of healing cycles $\mathcal{N}_{HC}$ describes the ability of the system to sustain local deformation and different values of $\mathcal{N}_{HC}$ allow us to study systems ranging from quasi-brittle materials ($\mathcal{N}_{HC} \to 1$) to very ductile ones ($\mathcal{N}_{HC} \to \infty$). Our results are also in excellent

agreement with very recent experiments [Sun et al. 2010] on ductile metallic glasses showing the cycles of sudden stress drops followed by elastic reloading associated with shear-band motions.

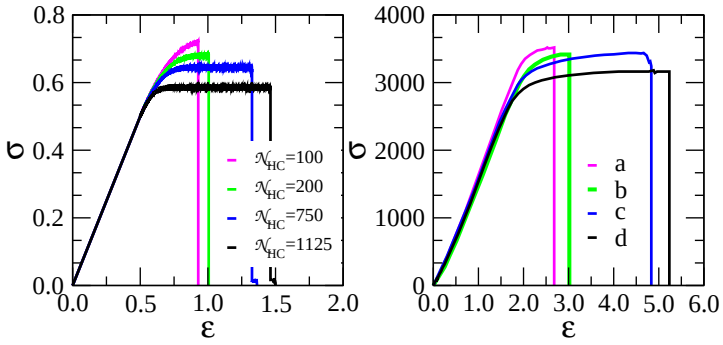

Figure 5.5: Left: DRFM in an $L = 75$ diamond lattice of size with increasing mean threshold value and different disorder realizations. Right: experimental data from [Gu et al. 2008] for BMGs with increasing ductility from a to d. (a) $Fe_{63}Cr_3Mo_{12}P_{10}C_7B_5$, (b) $Fe_{64}Cr_3Mo_{10}P_{10}C_{10}B_3$, (c) $Fe_{63}Cr_3Mo_{10}P_{12}C_{10}B_2$ and (d) $Fe_{71}Mo_5P_{12}C_{10}B_2$.

The parameter β mimics the characteristic serrated flow present in amorphous materials (see for instance [Schuh and Nieh 2003]). The effect of β can be better observed in the figure below.

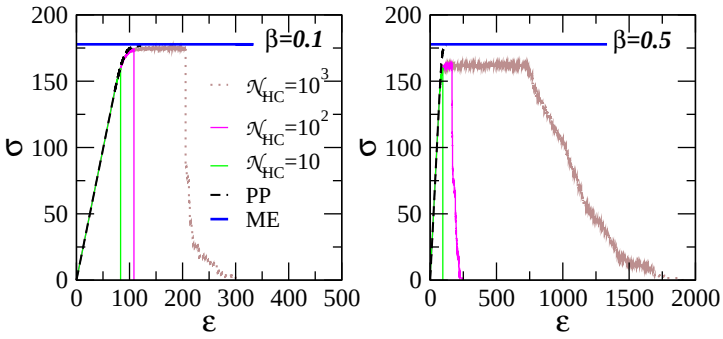

Figure 5.6: Global stress-strain curves for different typical disorder realizations and different number of healing cycles for $\beta = 0.1$ and $\beta = 0.5$. The ME yield stress is also shown.

Figure 5.6 shows that the data corresponding to $\mathcal{N}_{HC} = 10$ and $\mathcal{N}_{HC} = 10^2$ are much closer to the final expected ME steady-state (horizontal solid line)

in the case $\beta = 0.5$ than those in the case $\beta = 0.1$. This is caused by the fact that the stress relief is proportional to β. Therefore, while a lower β tends to quench the activity in some areas of the system for long periods of time, a higher β allows the system to explore much faster different regions of the phase space of configurations. This is also the reason for the noisier nature of the stress-strain curve for higher β; since $\Delta_i j = \beta\, i_{ij}^{th}/k_{ij}$, the amplitude of these fluctuations is proportional to β. Interestingly, the strain rate only affects the dynamics but not the final state of the system. Hence, in our simulations we used $\beta = 0.1$ unless stated otherwise.

5.3.1 Brittleness to ductility transition

Figure 5.7 shows the resulting fracture paths in the DRFM for the same conditions and disorder configuration as in the simulations shown in figure 5.6. One immediately notices that the final fracture surface configuration depends on the number of healing cycles $\mathcal{N}_{HC}$ and therefore on the accumulated plastic strain. These surfaces are to be compared with the ones emerging from the perfect plasticity limit ($\mathcal{N}_{HC} \to \infty$) that was discussed in Chapter 4 [Picallo et al. 2009]. As a reference, we plot the ME surface [Middleton 1995] and the PP path found with the algorithm of Roux and Hansen [Picallo et al. 2009, Roux and Hansen 1992] for exactly the same disorder configuration. As we showed in section 4.2 of this Thesis, these two surfaces minimize the sum of the local yield stresses and the stress flowing through the surface, respectively [Picallo et al. 2009]. It becomes apparent that the deeper the system is allowed into the plastic steady-state ($\mathcal{N}_{HC} \gg 1$), the closer the resulting fracture surface is to the ME path for the same disorder configuration. In contrast, the PP path [Picallo et al. 2009, Roux and Hansen 1992], seems to play no obvious role in the space of configurations. This can be observed in figure 5.7, where the fracture surface almost overlaps with the ME surface already for $\mathcal{N}_{HC} = 10^3$. To quantify how similar the fracture surface is to the brittle fracture and ME limits as ductility, $\mathcal{N}_{HC}$, increases, we define the overlap between two given paths $\{x_i\}$ and $\{y_i\}$ as

$$O = (1/Z) \sum_i \delta(x_i - y_i), \tag{5.5}$$

where Z is a normalization constant so that the overlap becomes unity for two identical surfaces.

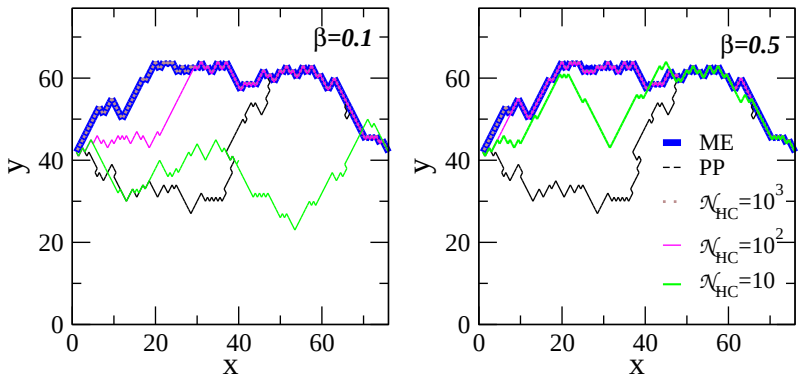

Figure 5.7: ME, PP and DRFM surfaces in a realization of a $L = 75$ system for $\beta = 0.1$ (left) and $\beta = 0.5$ (right).

In figure 5.8 we plot the overlap between the plastic fracture surface and the directed ME surface for the same disorder realization. For the sake of comparison we also compute the overlap with the corresponding purely brittle fracture surface [de Arcangelis et al. 1985] for the same disorder realization (*i.e.*, setting $\mathcal{N}_{HC} = 0$).

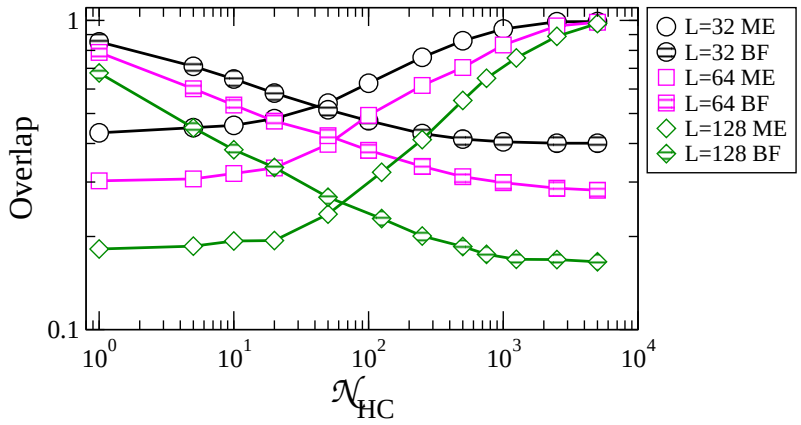

Figure 5.8: Average over 10^3 disorder realizations of the total spatial overlap of the DRFM final crack with both the corresponding ME and brittle fracture ($\mathcal{N}_{HC} = 0$) surfaces for $\beta = 0.1$.

The PP surface resulting from the PPRFM seems to be irrelevant for this problem and, consequently, the overlap is negligible for all $\mathcal{N}_{HC}$. Figure 5.8

demonstrates that the system is quasi-brittle for low values of $\mathcal{N}_{HC}$ where the fracture surface largely overlaps with the purely brittle fracture surface. In contrast, if the material is allowed to accumulate locally more strain (*i.e.* for larger $\mathcal{N}_{HC}$) then the overlap with the brittle fracture rapidly decreases, while the path becomes progressively closer to the directed ME path. This requires a large value of the $\mathcal{N}_{HC}$ index so that the system is able to explore adequately the space of optimum configurations before complete failure. The latter results are in agreement with the results reported in more complex models [Miltenberger et al. 1993].

It can be observed in figure 5.9 the finite-L behavior of the overlap which decays as $\sim \log(1/L)$ with system size. This is true in both $\mathcal{N}_{HC} \to \infty$ (ME) and $\mathcal{N}_{HC} = 1$ (quasi-brittle) limits.

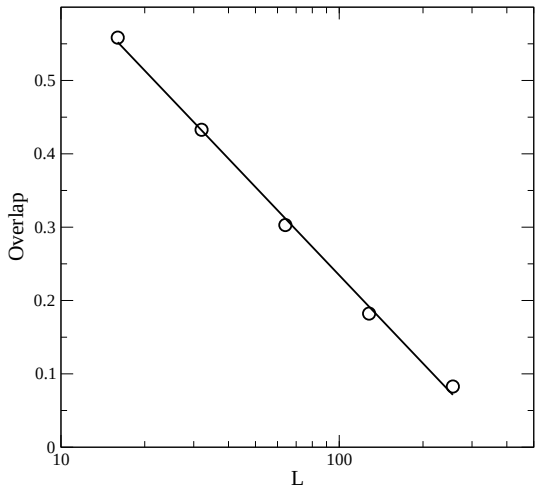

Figure 5.9: Average overlap between $\mathcal{N}_{HC} = 1$ fracture surfaces and the corresponding ME surfaces for the same disorder realization. Note the semi-logarithmic scale.

5.3.2 Roughness of brittle and ductile surfaces

The brittle fracture and ME surfaces are both self-affine fractals but the corresponding (local) roughness exponents are quite close: $\zeta_{\mathrm{BF}} \approx 0.7$ [Alava et al. 2006] for the brittle RFM, while the exact roughness exponent is $\zeta_{\mathrm{ME}} = 2/3$ [Halpin-Healy and Zhang 1995] for the ME surface. The dependence of the roughness exponent with the number of healing cycles is studied in figure 5.10 where it is shown the structure factor $S(k) = \langle \hat{y}(k)\hat{y}(-k) \rangle$, where

$\hat{y}(k)$ is the Fourier transform of the interface, as a function of the number of healings. This quantity gives the roughness exponent of the interface since it scales as $S(k) \sim k^{-(2\zeta+1)}$ in two dimensions [Barabási and Stanley 1995]. For comparison, ME and brittle fracture roughness exponents for the same disorder realizations are also shown. Although the roughness exponents of both problems are very close and hence are difficult to distinguish, a smooth transition from one exponent to the other is clearly observed as we increase the ductility.

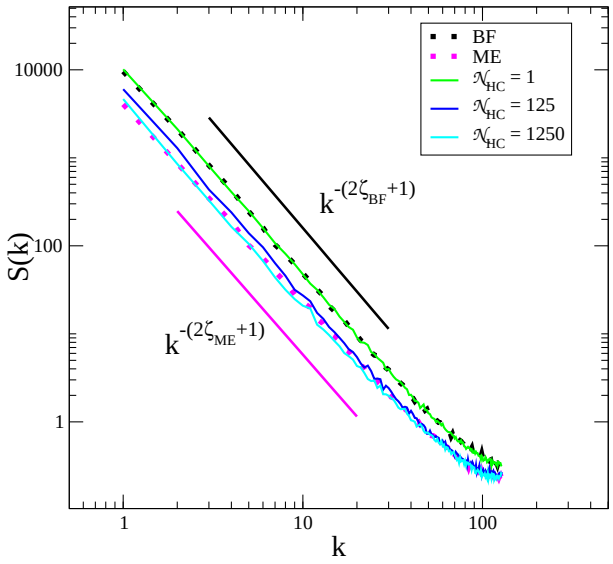

Figure 5.10: Structure factor for increasing number of healing cycles in a $L = 128$ system. ME and brittle fracture data are also shown for comparison.

5.3.3 Damage accumulation and localization

When only a small number of healing cycles is allowed prior to fracture, the system still behaves quasi-brittle and the fracture path and damage resemble the usual brittle fracture in the RFM. In figure 5.11, the consequences of breaking the system during the early stages of evolution are evidenced.

We impose fracture after only one healing cycle, $\mathcal{N}_{HC} = 1$, so the damage is still randomly spread in the system and fuses burn throughout the entire lattice, giving rise to a fracture path far from the ME surface. In fact, the system is behaving quasi-brittle since almost no deformation is allowed to accumulate before breakdown. The damage in the form of broken bonds is

spatially distributed throughout the sample in a randomly uniform fashion, in analogy to the brittle RFM.

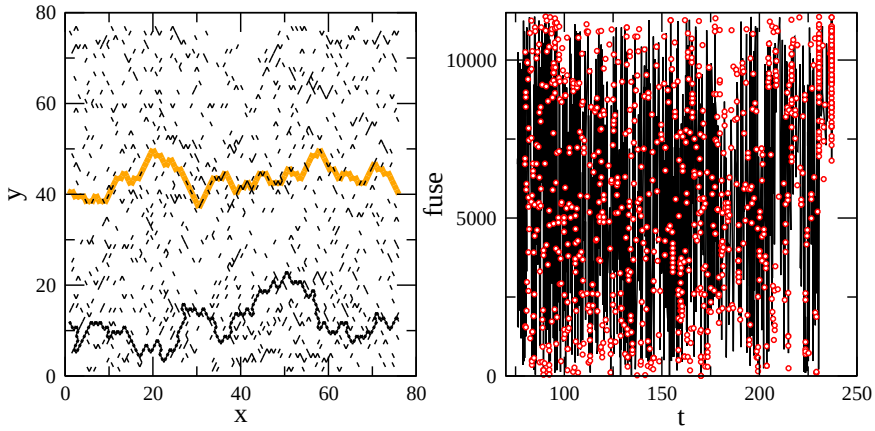

Figure 5.11: Realization of a $L = 75$ system for $\mathcal{N}_{HC} = 1$. Left: Fracture (black) and ME (orange) surface. Notice that the damage is diffuse all across the system. Right: fuse (running from 1 to the total number of fuses) that is healed/burnt each time step.

In contrast, figure 5.12 shows the effect of breaking the system after damage has accumulated onto certain shear bands. If we start burning fuses after $\mathcal{N}_{HC} = 10^3$ healing cycles, which corresponds to an average accumulated plastic strain of order $10^3 \beta i_{ij}^{th}/(k_{ij} L_y)$ per site, this surface is so weak due to the accumulation of deformation that is burnt very fast, with no trace of damage away from the fracture surface. In the steady-state, the strain would be completely localized and the ductile surface would be exactly the ME surface for a finite but large $\mathcal{N}_{HC}$ in a finite sample. The small differences that persist in figure 5.12 between the ductile fracture surface after $\mathcal{N}_{HC} = 10^3$ and ME are due to the yet incomplete localization of the system that was broken before it reached the plastic steady-state.

In the DRFM the yield localization behaves randomly for small $\mathcal{N}_{HC}$ as we saw in the right panel of figure 5.11, except that, due to stress enhancements, a degree of local "clustering" exists, and it increases slowly along the stress-strain curve until the final localization of damage and yielding as the fracture surface starts to be formed, as it is depicted in the right panel of figure 5.12. Such a trend is analogous to what is seen in the brittle RFM for damage accumulation [Alava et al. 2006]. This is interesting since such local plastic strains can be measured in experiments.

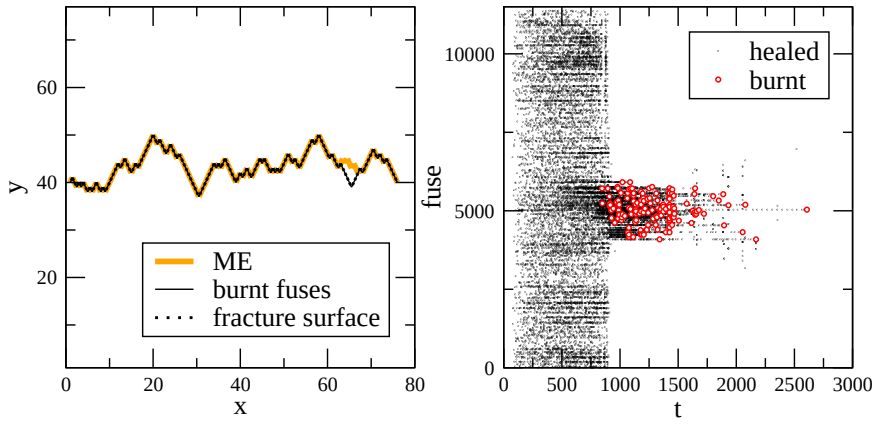

Figure 5.12: Realization of a $L = 75$ system for $\mathcal{N}_{HC} = 10^3$. Left: Fracture and ME surface. Notice that, in contrast with figure 5.11, there are no broken bonds away from the main fracture path. Right: fuse (running from 1 to the total number of fuses) that is healed/burnt each time step showing the strong and progressive localization of damage in time.

In figure 5.13, we study the damage localization degree by calculating the average ratio between the number of fuses needed to be burnt in order to disconnect the system, n_{D}, and the number of fuses of the corresponding ME surface, n_{ME}.

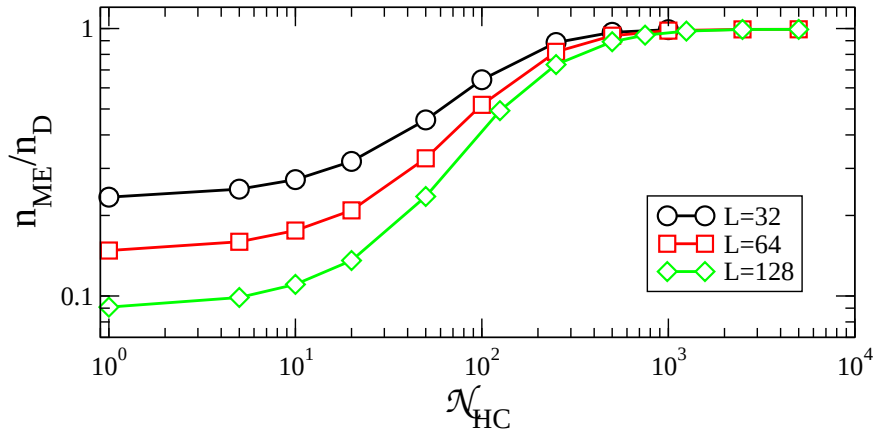

Figure 5.13: Average localization curves for different system sizes showing the transition from randomly spread damage to localization onto a line.

In the plastic steady-state ($\mathcal{N}_{HC} \to \infty$), the strain is completely localized and $n_{\rm D} = n_{\rm ME}$, as shown in figure 5.13. This quantifies how, as we increase the number of healing cycles, the fracture occurs only in the previously damaged surface, that progressively tends to the ME path for the corresponding disorder realization.

In figure 5.14 we depict the spatial distributions of damage. The average damage profile $p(y)$ is calculated from the fraction of broken bonds $n_b(y)$ along the y direction and is computed as $p(y) = \langle n_b(y) \rangle / L_x$, where the averaging is obtained by first shifting the damage profiles by the center of mass and then averaging over different samples [Nukala et al. 2004].

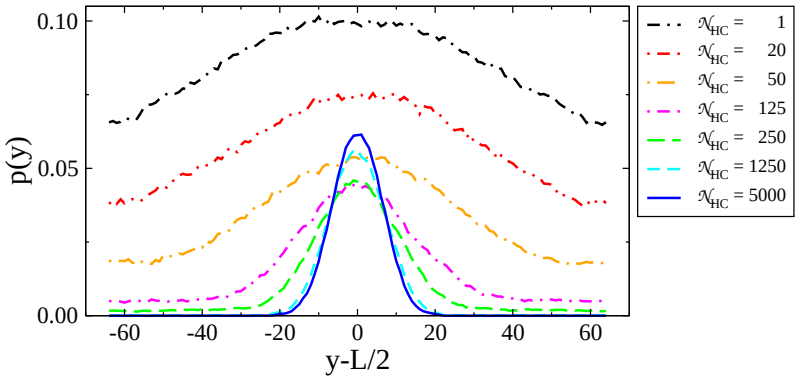

Figure 5.14: Average damage profiles for the DRFM in a system of size $L = 128$ for different values of $\mathcal{N}_{HC}$.

Strong localization of damage is demonstrated by the distribution $p(y)$ becoming narrower for larger $\mathcal{N}_{HC}$, as the material is allowed to accumulate more local irreversible strain. Prior to the growth of the final crack, there appears to be only local correlations in the damage similarly to what happens for the brittle RFM [Nukala et al. 2004, Reurings and Alava 2005], and the maxima in the profiles arise from the crack path. This demonstrates again how, with an increased number of healing cycles, fractures tend to only occur in the final crack surface, which progressively tends to the ME path as the material is made more ductile.

Figure 5.15 shows the excellent finite-size data collapse with the functional form

$$p(y) = p(L/2) f[(y - L/2)/L^{\zeta_{\rm ME}}], \tag{5.6}$$

for the average profiles of accumulated damage for very ductile samples ($\mathcal{N}_{HC} = 5 \times 10^3$) with the local roughness exponent $\zeta_{\mathrm{ME}} = 2/3$ corresponding to ME.

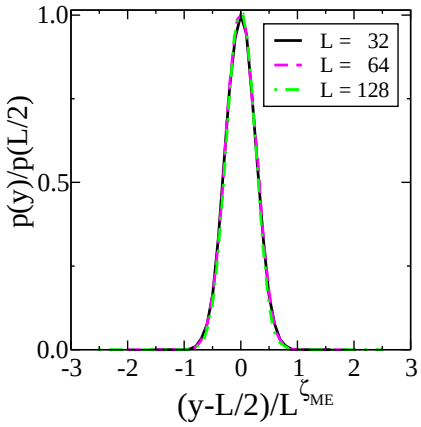

Figure 5.15: The corresponding data collapse for different system sizes in the case of large ductility $\mathcal{N}_{HC} = 5 \times 10^3$.

We also observe in figure 5.16 that, in the quasi-brittle limit, damage is volume-like, as expected for RFM [Nukala et al. 2004], while in the extremely ductile case damage scales as $\sim L$, as the failing elements concentrate at the one-dimensional crack.

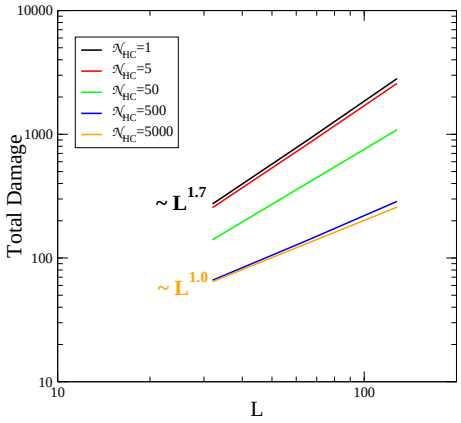

Figure 5.16: Scaling of the total number of broken fuses with system size. As the number of healing cycles increases, there is a transition from damage spread across the whole system, as expected for the brittle RFM, to damage localized onto a line.

5.3.4 Avalanche distribution

We measure strain avalanches as the total strain accumulated in the system between two external stress increments. In the DRFM the avalanche size is given by

$$s = \sum_{i=1}^{n} \Delta_i / L_y, \tag{5.7}$$

which corresponds to the sum of the voltage sources Δ_i added to the fuses between two external voltage increments and n is the number of fuses involved in the avalanche.

Figure 5.17 shows how the distribution of strain bursts for a sample of size $L = 128$ evolves towards the yielding point. It can be observed that the cutoff increases as the stress reaches the critical point, with an exponent that approaches $\tau = 3/2$. This is in agreement with theoretical predictions [Zaiser and Moretti 2005] and experiments [Dimiduk et al. 2006, Miguel et al. 2001, Richeton et al. 2006, Schwerdtfeger et al. 2007, Wang et al. 2009, Zaiser et al. 2008]. In particular, recent measurements of the distribution of shear avalanches in ductile metallic glasses [Sun et al. 2010] have reported very similar values of the avalanche exponent.

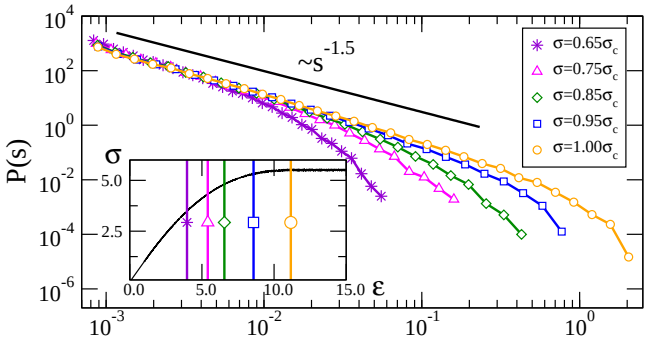

Figure 5.17: Statistics of strain avalanches in the DRFM for $\beta = 0.1$ in a very ductile sample. Avalanche distribution for a single realization in a system of size $L = 128$ collected up to different times in the evolution as marked in the inset.

On the other hand, well above the yielding point the material response is fully plastic and we measure a different strain avalanche distribution in this plastic steady-state, *i.e.* when the strain has already become completely localized and the average response in the global stress-strain curve in figure 5.5 is constant. To do this we start to record statistics of strain avalanches

well above the yielding point and obtain $\mathcal{P}(s) = L^{-D}(s/L^D)^{-\tau} f(s/L^D)$ with $\tau = 1.1 \pm 0.01$ and $D = 0.2 \pm 0.01$, where f is a finite-size scaling function obtained by a data collapse for different system sizes. $\tau \to 1$ corresponds to the plastic flow regime where the path of yielding sites effectively separates the system into two parts.

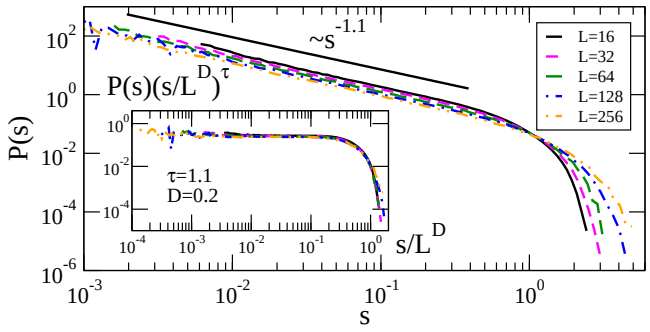

Figure 5.18: Avalanche distribution for the DRFM in the plastic steady-state, well above the yielding point. Inset shows the corresponding data collapse.

5.4 Discussion

We have discussed a scalar lattice model for plastic deformation and fracture in elasto-plastic heterogeneous materials from brittle to ductile behavior that was developed as part of this Thesis. The model is a generalization of the well-known random fuse model [de Arcangelis et al. 1985] for brittle fracture but it could readily be extended to tensorial models with more degrees of freedom such as beam models [Alava et al. 2006]. Our ductile random fuse model is able to accumulate plastic deformation before complete failure. Depending on a model parameter, the model can interpolate between brittle failure or perfect plasticity depending on how ductile the system is, or how much it can yield. Due to the two intertwined dynamics of fracture and yielding the DRFM presents a very rich behavior. In analogy to dislocation dynamics and other scenarios of plastic deformation, for ductile systems the dynamics of yielding is characterized by strain bursts [Dimiduk et al. 2006, Miguel et al. 2001, Richeton et al. 2006, Schwerdtfeger et al. 2007, Wang et al. 2009, Zaiser et al. 2008] that are found to be power-law distributed with an exponent $\tau \approx 1.5$, which is to be compared with experiments reporting $\tau = 1.4 - 1.6$ [Dimiduk et al. 2006, Miguel et al. 2001, Richeton et al. 2006, Schwerdtfeger et al. 2007, Wang et al. 2009, Zaiser et al. 2008] and close to an earlier theoretical pre-

diction, $\tau = 3/2$ [Zaiser and Moretti 2005]. Plastic deformation localizes into shear bands until a crack develops. The model exhibits a transition from purely brittle to fully ductile fracture, and includes both limits. A small accumulation of yield strain corresponds to quasi-brittle behavior. In contrast, as ductility is increased the resulting fracture paths gradually approach ME surfaces, and the damage spread decreases. Future directions from here include studying the DRFM in three dimensions, exploring the effect of adding hardening to the non-elastic part of the element response, and studying the correlations between serrated flow and shear banding.

Appendix A

List of Abbreviations

AE	Acoustic Emission
(B)MG	(Bulk) Metallic Glass
DP(RM)	Directed Polymer (in Random Media)
DRFM	Ductile Random Fuse Model
KCL	Kirchhoff Current Law
ME	Minimum Energy
MF	Mean Field
PDF	Probability Density Function
PP	Perfect Plasticity
PPRFM	Perfectly Plastic Random Fuse Model
RFM	Random Fuse Model
STZ	Shear Transformation Zone

Appendix B

List of Publications

B.1 Publications related to this Thesis

Picallo, C. B. and López, J. M. Energy dissipation statistics in the Random Fuse Model. *Phys. Rev. E* **77**, 046114 (2008).

Picallo, C. B., López, J. M., Zapperi, S., and Alava, M. J. Optimization and plasticity in disordered media. *Phys. Rev. Lett.* **103**, 225502 (2009).

Picallo, C. B., López, J. M., Zapperi, S., and Alava, M. J. From brittle to ductile fracture in disordered materials. *Phys. Rev. Lett.* **105**, 155502 (2010).

Picallo, C. B., López, J. M., Zapperi, S., and Alava, M. J. *In preparation* (2010).

B.2 Other publications

Picallo, C. B. and Riecke, H. Adaptive oscillator networks with conserved overall coupling: sequential firing and synchronized states. *Submitted to Phys. Rev. E* (2010).

Picallo, C. B., Pazó D., and López J. M. Influence of long-range links on dynamical diversity in excitable integrate-and-fire small world networks. *To be submitted to Phys. Rev. E* (2010).

Appendix C

Resumen en Castellano

La dinámica de fractura y el origen de la plasticidad en medios amorfos, es decir, aquellos que no cuentan con una estructura cristalina subyacente, es de gran interés tanto desde el punto de vista fundamental como desde la perspectiva del interés tecnológico en diversos frentes. El desarrollo de nuevos materiales se nutre del conocimiento en profundidad de los procesos que dominan la deformación en los materiales. Es especialmente importante conocer los efectos de tamaño sobre las leyes de comportamiento de los materiales para el desarrollo de tecnologías a la nanoescala. Asimismo, las estructuras jerárquicas presentes en los tejidos biolólogicos constituyen un campo que comienza a ser explorado actualmente y que abre la puerta a numerosas aplicaciones en el ámbito de los biomateriales [Buehler and Keten 2010]. Es por ello que el conocimiento de las propiedades que rigen la deformación y fractura de los materiales a nivel fundamental es de gran importancia. En este sentido son de gran interés los llamados modelos mesoscópicos [Alava et al. 2006] que abogan por describir el material a un nivel en el que las interacciones atómicas dejan de ser esenciales y el sistema se puede tratar como un conjunto de elementos interactuantes, cada uno de ellos con una determinada ley constitutiva. Estos modelos simplificados se inspiran en el hecho de que los mismos fenómenos de deformación y fractura pueden observarse a todas las escalas, desde en los terremotos en la corteza terrestre hasta en muestras de materiales de tamaño nanométrico y, además, exhiben el mismo tipo de comportamiento intermitente, con presencia de distribuciones de ley de potencias tanto en el espacio como en el tiempo. Esta universalidad sugiere que los mecanismos esenciales del fenómeno no deben encontrarse ni en la estructura microscópica

ni en la macroscópica del sistema sino que responden a leyes más elementales como simetrías y leyes de invarianza del problema. Estas propiedades colocan a la fractura y la plasticidad en la cercanía de los fenómenos críticos y su posible explicación como una transición de fase es aún controvertida [Alava et al. 2006, Zaiser 2006].

El objetivo de esta tesis es el estudio de la deformación y fractura de materiales amorfos. Para ello, describiremos el medio de manera discreta mediante elementos que pueden comportarse de manera frágil o dúctil. Los materiales frágiles se comportan de manera elástica –es decir, la deformación desaparece una vez que la fuerza que la causa es retirada– hasta que fallan de manera definitiva produciéndose una fractura macroscópica. Por contra, los materiales dúctiles comienzan a acumular deformaciones de tipo plástico tras una primera fase elástica. Las deformaciones plásticas son irreversibles, de carácter permanente y la fractura en este régimen es diferente, incluso a veces a simple vista, de las fracturas en materiales frágiles. El límite de plasticidad perfecta se alcanza cuando, en el régimen plástico, la deformación aumenta de manera indefinida sin incremento de la tensión mecánica en el medio, de manera similar a lo que ocurre en un fluido.

Dado que no estamos interesados en una descripción fenomenológica de los materiales sino más bien en los mecanismos fundamentales responsables de los procesos de deformación y fractura, usaremos un sencillo modelo escalar, el *Random Fuse Model* (RFM) [de Arcangelis et al. 1985], en el que se estudian las propiedades mecánicas del medio a través de un análogo eléctrico, donde cada elemento de la rejilla es un fusible que se comporta de manera óhmica –elástica– hasta un cierto umbral a partir del cual se puede convertir en aislante –fractura frágil– o mantener su corriente constante –plasticidad perfecta–. El desorden en el material se puede introducir de manera muy sencilla asignando valores a los umbrales de los fusibles de acuerdo a una cierta distribución de probabilidad.

Cuando un material se rompe, la energía acumulada se disipa a través de varios procesos. Entre ellos destaca la emisión acústica por su utilidad para extraer información del proceso de fractura a nivel microscópico. Este fenómeno presenta una estructura espacio-temporal definida que se caracteriza por la presencia de distribuciones de actividad que obedecen leyes de escala en forma de ley de potencias con exponentes característicos. Este tipo de comportamiento parece ser de carácter universal y está presente en otros muchos sistemas a diversas escalas, desde terremotos en la corteza terrestre al ruido de Barkhausen en materiales ferromagnéticos [Sethna et al. 2001]. Todos ellos se distinguen porque la dinámica se produce en forma de avalanchas carac-

terizadas por una distribución de tamaños y tiempos de espera en forma de ley de potencias, similares a las observadas en las inmediaciones de un punto crítico.

En el Capítulo 3 hemos estudiado la energía disipada en el RFM con el objetivo de comparar su estadística con la de la emisión acústica en experimentos de fractura frágil. Hemos estudiado la distribución de probabilidad de diferentes estimadores de la energía liberada. Nuestros resultados indican que existen dos regiones muy diferentes dependiendo de la escala de energías en que centremos nuestra atención, separados por una energía típica. La región de energías bajas se caracteriza por un decaimiento en ley de potencias de la forma $\mathcal{P}(E) \sim E^{-1/2}$ que es robusta e independiente del tipo de rejilla utilizado y su aparición está ligada a la naturaleza cuasi-estática del modelo, tal y como se demuestra en la sección 3.2 por medio de relaciones de escalado. La estadística por encima de la energía típica $E_\times$ presenta un escalado $\mathcal{P}(E) \sim E^{-2.75}$ que se extiende a lo largo de varias décadas en energía. Este régimen de energías altas resulta ser de gran interés debido a su papel como indicador de la proximidad de la fractura en el material ya que, mientras que el exponente de las energías bajas es constante a lo largo de todo el proceso de carga del material, el exponente de energías altas está en evolución constante. La influencia de relajar la dinámica cuasi-estática del medio también es analizada. De esta manera, aparece un único régimen $\mathcal{P}(E) \sim E^{-1}$ que domina toda la distribución. Estos resultados fueron publicados en [Picallo and López 2008].

En el Capítulo 4 nos hemos centrado en materiales que se comportan de manera elástica-perfectamente plástica utilizando una versión elasto-plástica del RFM. Mediante simulaciones numéricas y argumentos teóricos hemos demostrado que las superficies de fluencia y las superficies de mínima energía en el medio corresponden a problemas de optimización diferentes y, de hecho, el límite de fluencia es menor en el caso perfectamente plástico. Se han estudiado además las propiedades de rugosidad, distribuciones de energía y distribuciones de tensión de fluencia demostrando que la superficie de fluencia perfectamente plástica no es univaluada y es esto lo que le proporciona unas características de multiafinidad que evidencian las diferencias con las superficies de mínima energía, de carácter autoafín. Estos resultados fueron publicados en [Picallo et al. 2009].

En el clásico RFM elástico-perfectamente plástico no existen avalanchas de deformación, al contrario de lo que se observa experimentalmente en los medios que exhiben deformaciones plásticas. Es por ello que en el Capítulo 5 introducimos un modelo que, preservando la atractiva simplicidad del RFM,

es capaz de reproducir avalanchas de deformación. De hecho, mostramos que su distribución escala con el mismo exponente encontrado usualmente en experimentos y predicho también por teorías de campo medio. Este modelo puede describir materiales tanto frágiles como dúctiles –tanto perfectamente plásticos como con endurecimiento– ajustando un único parámetro que mide la ductilidad del material. La deformación se localiza en bandas hasta que el material supera su umbral de ruptura y se desarrolla la fractura final. Se estudian propiedades de localizacion, distribución del daño en el material y la transición del límite frágil al perfectamente plástico. El modelo exhibe un comportamiento muy rico y que proporciona gran cantidad de posibilidades por explorar. Estos resultados se encuentran en [Picallo et al. 2010a;b].

Bibliography

Alava, M. J. and Duxbury, P. M. (1996). Disorder-induced roughening in the three-dimensional Ising model. *Phys. Rev. B*, 54(21):14990–14993.

Alava, M. J., Nukala, P. K. V. V., and Zapperi, S. (2006). Statistical models of fracture. *Adv. Phys.*, 55:349–476.

Alava, M. J., Nukala, P. K. V. V., and Zapperi, S. (2009). Size effects in statistical fracture. *J. Phys. D. Appl. Phys.*, 42(21):214012.

Arbabi, S. and Sahimi, M. (1993). Mechanics of disordered solids. I. Percolation on elastic networks with central forces. *Phys. Rev. B*, 47(2):695–702.

Argon, A. (1979). Plastic deformation in metallic glasses. *Acta Metallurgica*, 27(1):47 – 58.

Bailey, N. P., Schiøtz, J., Lemaître, A., and Jacobsen, K. W. (2007). Avalanche size scaling in sheared three-dimensional amorphous solid. *Phys. Rev. Lett.*, 98(9):095501.

Barabási, A.-L. and Stanley, H. E. (1995). *Fractal concepts in surface growth*. Cambridge University Press.

Baret, J.-C., Vandembroucq, D., and Roux, S. (2002). Extremal model for amorphous media plasticity. *Phys. Rev. Lett.*, 89(19):195506.

Batrouni, G. G. and Hansen, A. (1988). Fourier acceleration of iterative processes in disordered systems. *J. Stat. Phys.*, 52:747–773.

Becker, R. and Orowan, E. (1932). Über sprunghafte dehnung von zinkkristallen. *Zeitschrift für Physik A: Hadrons and Nuclei*, 79(9-10):566–572.

Bitzek, E., Brandl, C., Derlet, P. M., and Van Swygenhoven, H. (2008). Dislocation cross-slip in nanocrystalline fcc metals. *Phys. Rev. Lett.*, 100(23):235501.

Bonamy, D. (2009). Intermittency and roughening in the failure of brittle heterogeneous materials. *Journal of Physics D: Applied Physics*, 42(21):214014.

Bonnot, E., Vives, E., Mañosa, L., Planes, A., and Romero, R. (2008). Acoustic emission and energy dissipation during front propagation in a stress-driven martensitic transition. *Phys. Rev. B*, 78(9):094104.

Buehler, M. J. (2008). *Atomistic modeling of materials failure*. Springer.

Buehler, M. J. and Keten, S. (2010). Colloquium: Failure of molecules, bones, and the Earth itself. *Rev. Mod. Phys.*, 82(2):1459–1487.

Buldyrev, S. V., Havlin, S., and Stanley, H. E. (2006). Optimal paths in strong and weak disorder: A unified approach. *Phys. Rev. E*, 73(3):036128.

Carpinteri, A., Lacidogna, G., and Puzzi, S. (2009). From criticality to final collapse: Evolution of the b-value from 1.5 to 1.0. *Chaos, Solitons and Fractals*, 41(2):843 – 853.

Champion, Y., Langlois, C., Guerin-Mailly, S., Langlois, P., Bonnentien, J.-L., and Hytch, M. J. (2003). Near-perfect elastoplasticity in pure nanocrystalline copper. *Science*, 300(5617):310–311.

Chen, Y., Davis, T. A., Hager, W. W., and Rajamanickam, S. (2008). Algorithm 887: CHOLMOD, supernodal sparse Cholesky factorization and update/downdate. *ACM Trans. Math. Softw.*, 35(3):1–14.

Christopher A. Schuh, A. C. L. (2003). Atomistic basis for the plastic yield criterion of metallic glass. *Nat. Mater.*, 2(7):449–452.

Cieplak, M., Maritan, A., and Banavar, J. R. (1994). Optimal paths and domain walls in the strong disorder limit. *Phys. Rev. Lett.*, 72(15):2320–2323.

Cormen, T. H., Leiserson, C. E., Rivest, R. L., and Stein, C. (2001). *Introduction to Algorithms*. MIT Press.

Cowie, P. A., Vanneste, C., and Sornette, D. (1993). Statistical physics model for the spatiotemporal evolution of faults. *J. Geophys. Res.*, 98(B12):21809–21821.

da Vinci, L. (1940). *I libri di meccanica nella ricostruzione ordinate da Arturo Uccelli*. Hoepli.

Daniels, H. E. (1945). The statistical theory of the strength of bundles of threads. *Proceedings of the Royal Society of London. Series A, Mathematical and Physical Sciences*, 183(995):405–435.

Davidsen, J., Stanchits, S., and Dresen, G. (2007). Scaling and universality in rock fracture. *Phys. Rev. Lett.*, 98(12):125502.

Davis, T. A. and Hager, W. W. (1999). Modifying a sparse Cholesky factorization. *SIAM Journal on Matrix Analysis and Applications*, 20(3):606–627.

Davis, T. A. and Hager, W. W. (2001). Multiple-rank modifications of a sparse Cholesky factorization. *SIAM Journal on Matrix Analysis and Applications*, 22(4):997–1013.

de Arcangelis, L., Redner, S., and Herrmann, H. J. (1985). A random fuse model for breaking processes. *J. Phys. Lett. (Paris)*, 46:585–590.

Derrida, B. and Vannimenus, J. (1983). Interface energy in random systems. *Phys. Rev. B*, 27(7):4401–4411.

Dimiduk, D. M., Woodward, C., LeSar, R., and Uchic, M. D. (2006). Scale-free intermittent flow in crystal plasticity. *Science*, 312(5777):1188–1190.

Dubach, A., Raghavan, R., Löffler, J., Michler, J., and Ramamurty, U. (2009). Micropillar compression studies on a bulk metallic glass in different structural states. *Scripta Mater.*, 60:567–570.

Durin, A. and Zapperi, S. (2005). The Barkhausen effect. In Bertotti, G. and Mayergoyz, I., editors, *The Science of Hysteresis*, volume 2, chapter 3, pages 181–267. Elsevier Academic Press.

Falk, M. L. and Langer, J. S. (1998). Dynamics of viscoplastic deformation in amorphous solids. *Phys. Rev. E*, 57(6):7192–7205.

Field, S., Witt, J., Nori, F., and Ling, X. (1995). Superconducting vortex avalanches. *Phys. Rev. Lett.*, 74(7):1206–1209.

Forster, D., Nelson, D. R., and Stephen, M. J. (1977). Large-distance and long-time properties of a randomly stirred fluid. *Phys. Rev. A*, 16(2):732–749.

Galilei, G. (1638). *Discorsi e dimostrazioni matematiche intorno à due nuoue scienze attenenti alla mecanica & i movimenti locali*. Louis Elsevier, Leiden.

Garcimartín, A., Guarino, A., Bellon, L., and Ciliberto, S. (1997). Statistical properties of fracture precursors. *Phys. Rev. Lett.*, 79(17):3202–3205.

Godano, C. and Pingue, F. (2000). Is the seismic moment-frequency relation universal? *Geophysical Journal International*, 142:193–198.

Greer, A. L. (2009). Metallic glasses on the threshold. *Materials Today*, 12(1-2):14 – 22.

Griffith, A. A. (1921). The phenomena of rupture and flow in solids. *Royal Society of London Philosophical Transactions Series A*, 221:163–198.

Gu, X., Poon, S. J., Shiflet, G. J., and Widom, M. (2008). Ductility improvement of amorphous steels: Roles of shear modulus and electronic structure. *Acta. Mater.*, 56(1):88 – 94.

Guarino, A., Ciliberto, S., Garcimartín, A., Zei, M., and Scorretti, R. (2002). Failure time and critical behaviour of fracture precursors in heterogeneous materials. *Eur. Phys. J. B*, 26(2):141–151.

Guarino, A., Garcimartín, A., and Ciliberto, S. (1998). An experimental test of the critical behaviour of fracture precursors. *Eur. Phys. J. B*, 6(1):13–24.

Guo, H., Yan, P. F., Wang, Y. B., Tan, J., Zhang, Z. F., Sui, M. L., and Ma, E. (2007). Tensile ductility and necking of metallic glass. *Nat. Mater.*, 6:735–739.

Halpin-Healy, T. and Zhang, Y. (1995). Kinetic roughening phenomena, stochastic growth, directed polymers and all that. Aspects of multidisciplinary statistical mechanics. *Phys. Rep.*, 254:215–414.

Han, Z., He, L., Zhong, M., and Hou, Y. (2009). Dual specimen-size dependences of plastic deformation behavior of a traditional Zr-based bulk metallic glass in compression. *Mater. Sci. Eng. A*, 513-514:344 – 351.

Hansen, A. and Hemmer, P. C. (1994). Burst avalanches in bundles of fibers: Local versus global load-sharing. *Phys. Lett. A*, 184:394–396.

Hansen, A., Hinrichsen, E. L., and Roux, S. (1991). Roughness of crack interfaces. *Phys. Rev. Lett.*, 66(19):2476–2479.

Hansen, A. and Kertész, J. (2004). Phase diagram of optimal paths. *Phys. Rev. Lett.*, 93(4):040601.

Hemmer, P. C. and Hansen, A. (1992). The distribution of simultaneous fiber failures in fiber bundles. *J. Appl. Mech*, 59(4):909–914.

Hooke, R. (1678). *De Potentia Restitutiva*. Royal Society of London.

Houle, P. A. and Sethna, J. P. (1996). Acoustic emission from crumpling paper. *Phys. Rev. E*, 54(1):278–283.

Huse, D. A. and Henley, C. L. (1985). Pinning and roughening of domain walls in Ising systems due to random impurities. *Phys. Rev. Lett.*, 54(25):2708–2711.

Huse, D. A., Henley, C. L., and Fisher, D. S. (1985). Huse, Henley, and Fisher respond. *Phys. Rev. Lett.*, 55(26):2924.

Irwin, G. R. (1948). Fracture dynamics. *Trans. ASM*, 40A:147–166.

Kahng, B., Batrouni, G. G., Redner, S., de Arcangelis, L., and Herrmann, H. J. (1988). Electrical breakdown in a fuse network with random, continuously distributed breaking strengths. *Phys. Rev. B*, 37(13):7625–7637.

Kantor, Y. and Webman, I. (1984). Elastic properties of random percolating systems. *Phys. Rev. Lett.*, 52(21):1891–1894.

Kardar, M. (1985). Roughening by impurities at finite temperatures. *Phys. Rev. Lett.*, 55(26):2923.

Kardar, M., Parisi, G., and Zhang, Y.-C. (1986). Dynamic scaling of growing interfaces. *Phys. Rev. Lett.*, 56(9):889–892.

Koivisto, J., Rosti, J., and Alava, M. J. (2007). Creep of a fracture line in paper peeling. *Phys. Rev. Lett.*, 99(14):145504.

Krug, J., Meakin, P., and Halpin-Healy, T. (1992). Amplitude universality for driven interfaces and directed polymers in random media. *Phys. Rev. A*, 45(2):638–653.

Kuksenko, V., Tomilin, N., and Chmel, A. (2005). The role of driving rate in scaling characteristics of rock fracture. *J. Stat. Mech.: Theory Exp.*, 2005(06):P06012.

Lai, W. M., Rubin, D., and Krempl, E. (1999). *Introduction to Continuum Mechanics*. Butterworth Heinemann.

Langer, J. S. (2008). Shear-transformation zone theory of plastic deformation near the glass transition. *Phys. Rev. E*, 77(2):021502.

Laurson, L., Miguel, M.-C., and Alava, M. J. (2010). Dynamical correlations near dislocation jamming. *Phys. Rev. Lett.*, 105(1):015501.

Lee, C. J., Huang, J. C., and Nieh, T. G. (2007). Sample size effect and microcompression of $Mg_{65}Cu_{25}Gd_{10}$ metallic glass. *Appl. Phys. Lett.*, 91(16):161913.

Lee, M. W., Sornette, D., and Knopoff, L. (1999). Persistence and quiescence of seismicity on fault systems. *Phys. Rev. Lett.*, 83(20):4219–4222.

Lemaître, A. and Caroli, C. (2009). Rate-dependent avalanche size in athermally sheared amorphous solids. *Phys. Rev. Lett.*, 103(6):065501.

Leoni, F. and Zapperi, S. (2009). Slip line growth as a critical phenomenon. *Phys. Rev. Lett.*, 102(11):115502.

Li, Q.-K. and Li, M. (2005). Effects of surface imperfections on deformation and failure of amorphous metals. *Appl. Phys. Lett.*, 87(3):031910.

Li, Q.-K. and Li, M. (2007). Assessing the critical sizes for shear band formation in metallic glasses from molecular dynamics simulation. *Appl. Phys. Lett.*, 91(23):231905.

Lockner, D., Byerlee, J., Kuksenko, V., Ponomarev, A., and Sidorin, A. (1991). Quasi-static fault growth and shear fracture energy in granite. *Nature*, 350:39–42.

Lubliner, J. (2008). *Plasticity Theory*. Dover Publications.

Måløy, K. J., Santucci, S., Schmittbuhl, J., and Toussaint, R. (2006). Local waiting time fluctuations along a randomly pinned crack front. *Phys. Rev. Lett.*, 96(4):045501.

Maes, C., Van Moffaert, A., Frederix, H., and Strauven, H. (1998). Criticality in creep experiments on cellular glass. *Phys. Rev. B*, 57(9):4987–4990.

Maloney, C. E. and Lemaître, A. (2006). Amorphous systems in athermal, quasistatic shear. *Phys. Rev. E*, 74(1):016118.

Middleton, A. A. (1995). Numerical results for the ground-state interface in a random medium. *Phys. Rev. E*, 52(4):R3337–R3340.

Miguel, M.-C., Vespignani, A., Zaiser, M., and Zapperi, S. (2002). Dislocation jamming and Andrade creep. *Phys. Rev. Lett.*, 89(16):165501.

Miguel, M.-C., Vespignani, A., Zapperi, S., Weiss, J., and Grasso, J.-R. (2001). Intermittent dislocation flow in viscoplastic deformation. *Nature*, 410:667 – 671.

Miltenberger, P., Sornette, D., and Vanneste, C. (1993). Fault self-organization as optimal random paths selected by critical spatiotemporal dynamics of earthquakes. *Phys. Rev. Lett.*, 71(21):3604–3607.

Minozzi, M., Caldarelli, G., Pietronero, L., and Zapperi, S. (2003). Dynamic fracture model for acoustic emission. *Eur. Phys. J. B*, 36(2):203–207.

Monthus, C. and Garel, T. (2006). Probing the tails of the ground-state energy distribution for the directed polymer in a random medium of dimension $d = 1, 2, 3$ via a Monte Carlo procedure in the disorder. *Phys. Rev. E*, 74(5):051109.

Munilla, J., Castro, M., and Carnicero, A. (2009). Surface effects in atomistic mechanical simulations of Al nanocrystals. *Phys. Rev. B*, 80(2):024109.

Nattermann, T. and Lipowsky, R. (1988). Vortex behavior in high-T_c superconductors with disorder. *Phys. Rev. Lett.*, 61(21):2508.

Nelson, D. R. (1988). Vortex entanglement in high-T_c superconductors. *Phys. Rev. Lett.*, 60(19):1973–1976.

Niccolini, G., Durin, G., Carpinteri, A., Lacidogna, G., and Manuello, A. (2009). Crackling noise and universality in fracture systems. *J. Stat. Mech.: Theory Exp.*, 2009(01):P01023.

Nukala, P. K. V. V. and Simunovic, S. (2003). An efficient algorithm for simulating fracture using large fuse networks. *J. Phys. A*, 36:11403–11412.

Nukala, P. K. V. V., Simunovic, S., and Gudatti, M. N. (2005a). An efficient algorithm for modelling progressive damage accumulation in disordered materials. *Int. J. Numer. Meth. Engng.*, 62:1982–2008.

Nukala, P. K. V. V., Simunovic, S., and Zapperi, S. (2004). Percolation and localization in the random fuse model. *J. Stat. Mech.: Theory Exp.*, 2004(08):P08001.

Nukala, P. K. V. V., Zapperi, S., and Simunovic, S. (2005b). Statistical properties of fracture in a random spring model. *Phys. Rev. E*, 71(6):066106.

O. C. Zienkiewicz, R. L. T. (2006). *The Finite Element Method for Solid and Structural Mechanics*. Elsevier.

Ogielski, A. T. (1986). Integer optimization and zero-temperature fixed point in Ising random-field systems. *Phys. Rev. Lett.*, 57(10):1251–1254.

Pacheco, J. F., Scholz, C. H., and Sykes, L. R. (1992). Changes in frequency-size relationship from small to large earthquakes. *Nature*, 355:71–73.

Petri, A., Paparo, G., Vespignani, A., Alippi, A., and Costantini, M. (1994). Experimental evidence for critical dynamics in microfracturing processes. *Phys. Rev. Lett.*, 73(25):3423–3426.

Picallo, C. B. and López, J. M. (2008). Energy dissipation statistics in the random fuse model. *Phys. Rev. E*, 77(4):046114.

Picallo, C. B., López, J. M., Zapperi, S., and Alava, M. J. (2009). Optimization and plasticity in disordered media. *Phys. Rev. Lett.*, 103(22):225502.

Picallo, C. B., López, J. M., Zapperi, S., and Alava, M. J. (2010a). From brittle to ductile fracture in disordered materials. *Phys. Rev. Lett.*, 105(15):155502.

Picallo, C. B., López, J. M., Zapperi, S., and Alava, M. J. (2010b). In preparation.

Picard, G., Ajdari, A., Lequeux, F., and Bocquet, L. (2004). Elastic consequences of a single plastic event. *Eur. Phys. J. E*, 15(4):371–381.

Porto, M., Havlin, S., Schwarzer, S., and Bunde, A. (1997). Optimal path in strong disorder and shortest path in invasion percolation with trapping. *Phys. Rev. Lett.*, 79(21):4060–4062.

Porto, M., Schwartz, N., Havlin, S., and Bunde, A. (1999). Optimal paths in disordered media: Scaling of the crossover from self-similar to self-affine behavior. *Phys. Rev. E*, 60(3):R2448–R2451.

Pradhan, S., Hansen, A., and Hemmer, P. C. (2005). Crossover behavior in burst avalanches: Signature of imminent failure. *Phys. Rev. Lett.*, 95(12):125501.

Pradhan, S., Hansen, A., and Hemmer, P. C. (2006). Crossover behavior in failure avalanches. *Phys. Rev. E*, 74(1):016122.

Reurings, F. and Alava, M. J. (2005). Damage in random fuse networks. *Eur. Phys. J. B*, 47:85–91.

Rice, J. R. (1999). Foundations of solids mechanics. In Meyers, M. A., Armstrong, R. W., and Kirchner, H. O. K., editors, *Mechanics and materials: fundamentals and linkages*, chapter 3, pages 33–70. John Wiley and Sons.

Richeton, T., Dobron, P., Chmelik, F., Weiss, J., and Louchet, F. (2006). On the critical character of plasticity in metallic single crystals. *Mater. Sci. Eng. A*, 424(1-2):190 – 195.

Rosti, J., Illa, X., Koivisto, J., and Alava, M. J. (2009). Crackling noise and its dynamics in fracture of disordered media. *Journal of Physics D: Applied Physics*, 42(21):214013.

Rosti, J., Koivisto, J., and Alava, M. J. (2010). Statistics of acoustic emission in paper fracture: precursors and criticality. *J. Stat. Mech.: Theory Exp.*, 2010(02):P02016.

Roux, S. and Guyon, E. (1985). Mechanical percolation : a small beam lattice study. *J. Physique Lett.*, 46(21):999–1004.

Roux, S. and Hansen, A. (1992). Perfect plasticity in a random medium. *J. Phys. II*, 2:1007–1021.

Rundle, J. B. and Klein, W. (1989). Nonclassical nucleation and growth of cohesive tensile cracks. *Phys. Rev. Lett.*, 63(2):171–174.

Sahimi, M. and Arbabi, S. (1993a). Mechanics of disordered solids. II. Percolation on elastic networks with bond-bending forces. *Phys. Rev. B*, 47(2):703–712.

Sahimi, M. and Arbabi, S. (1993b). Mechanics of disordered solids. III. Fracture properties. *Phys. Rev. B*, 47(2):713–722.

Salminen, L. I., Pulakka, J. M., Rosti, J., Alava, M. J., and Niskanen, K. J. (2006). Crackling noise in paper peeling. *Europhys. Lett.*, 73(1):55–61.

Salminen, L. I., Tolvanen, A. I., and Alava, M. J. (2002). Acoustic emission from paper fracture. *Phys. Rev. Lett.*, 89(18):185503.

Santucci, S., Vanel, L., and Ciliberto, S. (2004). Subcritical statistics in rupture of fibrous materials: Experiments and model. *Phys. Rev. Lett.*, 93(9):095505.

Schall, P., Weitz, D. A., and Spaepen, F. (2007). Structural rearrangements that govern flow in colloidal glasses. 318(5858):1895–1899.

Scholz, C. H. (1968). The frequency-magnitude relation of microfracturing in rock and its relation to earthquakes. *Bulletin of the Seismological Society of America*, 58(1):399–415.

Schroers, J. and Johnson, W. L. (2004). Ductile bulk metallic glass. *Phys. Rev. Lett.*, 93(25):255506.

Schuh, C. A., Hufnagel, T. C., and Ramamurty, U. (2007). Mechanical behavior of amorphous alloys. *Acta Materialia*, 55(12):4067 – 4109.

Schuh, C. A. and Nieh, T. G. (2003). A nanoindentation study of serrated flow in bulk metallic glasses. *Acta Materialia*, 51(1):87 – 99.

Schuster, B., Wei, Q., Hufnagel, T., and Ramesh, K. (2008). Size-independent strength and deformation mode in compression of a Pd-based metallic glass. *Acta. Mater.*, 56(18):5091 – 5100.

Schwartz, N., Nazaryev, A. L., and Havlin, S. (1998). Optimal path in two and three dimensions. *Phys. Rev. E*, 58(6):7642–7644.

Schwerdtfeger, J., Nadgorny, E., Madani-Grasset, F., Koutsos, V., Blackford, J. R., and Zaiser, M. (2007). Scale-free statistics of plasticity-induced surface steps on KCl single crystals. *J. Stat. Mech.: Theory Exp.*, 2007(04):L04001.

Selinger, R. L. B., Wang, Z.-G., Gelbart, W. M., and Ben-Shaul, A. (1991). Statistical-thermodynamic approach to fracture. *Phys. Rev. A*, 43(8):4396–4400.

Sethna, J. P., Dahmen, K. A., and Myers, C. R. (2001). Crackling noise. *Nature*, 410(6825):242–250.

Shan, Z. W., Li, J., Cheng, Y. Q., Minor, A. M., Syed Asif, S. A., Warren, O. L., and Ma, E. (2008). Plastic flow and failure resistance of metallic glass: Insight from in situ compression of nanopillars. *Phys. Rev. B*, 77(15):155419.

Sornette, D. and Vanneste, C. (1992). Dynamics and memory effects in rupture of thermal fuse networks. *Phys. Rev. Lett.*, 68(5):612–615.

Sun, B. A., Yu, H. B., Jiao, W., Bai, H. Y., Zhao, D. Q., and Wang, W. H. (2010). Plasticity of ductile metallic glasses: A self-organized critical state. *Phys. Rev. Lett.*, 105(3):035501.

Uchic, M. D., Dimiduk, D. M., Florando, J. N., and Nix, W. D. (2004). Sample dimensions influence strength and crystal plasticity. *Science*, 305(5686):986–989.

Utsu, T. (1999). Representation and analysis of the earthquake size distribution: A historical review and some new approaches. *Pure and Applied Geophysics*, 155:509–535.

Wang, G., Chan, K., Xia, L., Yu, P., Shen, J., and Wang, W. (2009). Self-organized intermittent plastic flow in bulk metallic glasses. *Acta. Mater.*, 57(20):6146 – 6155.

Wang, Y., Li, J., Hamza, A. V., and Barbee, T. W. (2007). Ductile crystalline–amorphous nanolaminates. *PNAS*, 104(27):11155–11160.

Wang, Z.-G., Landman, U., Selinger, R. L. B., and Gelbart, W. M. (1991). Molecular-dynamics study of elasticity and failure of ideal solids. *Phys. Rev. B*, 44(1):378–381.

Weibull, W. (1951). A statistical distribution function of wide applicability. *J. Appl. Mech.*, 18:293–297.

Weiss, J. and Grasso, J.-R. (1997). Acoustic emission in single crystals of ice. *The Journal of Physical Chemistry B*, 101(32):6113–6117.

Weiss, J., Richeton, T., Louchet, F. m. c., Chmelik, F., Dobron, P., Entemeyer, D., Lebyodkin, M., Lebedkina, T., Fressengeas, C., and McDonald, R. J. (2007). Evidence for universal intermittent crystal plasticity from acoustic emission and high-resolution extensometry experiments. *Phys. Rev. B*, 76(22):224110.

Yao, J. H., Wang, J. Q., Lu, L., and Li, Y. (2008). High tensile strength reliability in a bulk metallic glass. *Appl. Phys. Lett.*, 92(4):041905.

Zaiser, M. (2006). Scale invariance in plastic flow of crystalline solids. *Adv. Phys.*, 55(1-2):185–245.

Zaiser, M. and Moretti, P. (2005). Fluctuation phenomena in crystal plasticity—a continuum model. *J. Stat. Mech.: Theory Exp.*, 2005(08):P08004.

Zaiser, M., Schwerdtfeger, J., Schneider, A. S., Frick, C. P., Clark, B. G., Gruber, P. A., and Arzt, E. (2008). Strain bursts in plastically deforming Molybdenum micro- and nanopillars. *Phil. Mag.*, 88:3861–3874.

Zapperi, S. and Nukala, P. K. V. V. (2006). Fracture statistics in the three-dimensional random fuse model. *Int. J. Fracture.*, 140:99–111.

Zapperi, S., Nukala, P. K. V. V., and Simunovic, S. (2005a). Crack avalanches in the three-dimensional random fuse model. *Physica A*, 357:129–133.

Zapperi, S., Nukala, P. K. V. V., and Simunovic, S. (2005b). Crack roughness and avalanche precursors in the random fuse model. *Phys. Rev. E*, 71(2):026106.

Zapperi, S., Ray, P., Stanley, H. E., and Vespignani, A. (1997). First-order transition in the breakdown of disordered media. *Phys. Rev. Lett.*, 78(8):1408–1411.

Zapperi, S., Ray, P., Stanley, H. E., and Vespignani, A. (1999). Avalanches in breakdown and fracture processes. *Phys. Rev. E*, 59(5):5049–5057.